INTERFACIAL INTERACTION OF GRAPHITIC MATERIALS WITH WATER AND DNA ORIGAMI NANOSTRUCTURES

by

Karen B. Ricardo Figueroa

B.S. in Chemistry, University of Puerto Rico, 2010

Submitted to the Graduate Faculty of

the Kenneth P. Dietrich School of Arts and Sciences in partial fulfillment

of the requirements for the degree of

Doctor of Philosophy

University of Pittsburgh

2017

UNIVERSITY OF PITTSBURGH

KENNETH P. DIETRICH SCHOOL OF ARTS AND SCIENCES

This dissertation was presented

by

Karen B. Ricardo Figueroa

It was defended on

July 20th, 2017

and approved by

Alexander Star, Ph.D., Professor, Department of Chemistry

Jennifer Laaser, Ph.D., Assistant Professor, Department of Chemistry

Lei Li, Ph.D., Associate Professor, Department of Chemical and Petroleum Engineering

Committee Chair: Haitao Liu, Ph.D., Associate Professor, Department of Chemistry

INTERFACIAL INTERACTION OF GRAPHITIC MATERIALS WITH WATER AND DNA ORIGAMI NANOSTRUCTURES

Karen B. Ricardo Figueroa, Ph.D.

University of Pittsburgh, 2017

Over the last decade, graphene has gained a lot of interest because of its electrical, mechanical and overall intrinsic properties. The wettability of graphene is paramount in determining its other surface properties and consequently, its applications. On the other hand, DNA origami nanostructures can be synthesized in a wide-variety of shapes, sizes and dimensions. It has been used to pattern different surfaces and act as a template for the CVD growth of inorganic oxides. Research in this area may establish DNA origami as an attractive, low cost template for nanofabrication.

This thesis focuses on the interfacial interaction of HOPG, exfoliated and CVD graphene with hydrophilic materials such as aqueous solutions and DNA origami nanostructures. Specifically, chapter 1 presents a comprehensive review of research involving our materials of interest. Chapter 2 reports the surfactant-free exfoliation of graphite in a weakly basic solution to obtain few layer graphene sheets. This work reversed the notion that organic solvents or ionic surfactants were needed for the exfoliation process. Chapter 3 depicts the deposition of DNA origami nanostructures onto HOPG. This work analyzed the interaction of ds-DNA with a clean and contaminated graphitic substrate and the CVD growth of SiO_2 specifically on the DNA origami. Finally, chapter 4 reports the encapsulation and thermal stability of DNA origami under CVD graphene, demonstrating that it is possible to use graphene as a protection barrier for materials that may be prone to degradation or decomposition under harsh conditions.

Understanding the interaction of carbon materials with hydrophilic components will be important for future applications, such as the fabrication of new sensors and electronic devices.

TABLE OF CONTENTS

LIST OF TABLES

LIST OF FIGURES

LIST OF EQUATIONS

PREFACE

First and foremost, I would like to express my deepest and sincere gratitude to my research advisor, Dr. Haitao Liu. His support and guidance during my time at the University of Pittsburgh have given me all the tools I need to become a successful scientist. Since day one, Haitao always believed in me, even in times when I did not believe in myself. His consideration of allowing me to work remotely from Atlanta will always be appreciated. Thanks again for everything you have done for me.

I would like to also thank Prof. Jill Millstone for all her time and advice during my research projects, comprehensive examination and proposal defense. I would like to thank Prof. David Waldeck and Dr. Nathaniel Rosi for their time and support during my proposal defense. The guidance that Dr. Rosi provided made me a better writer and scientist. I would like to thank Prof. Lei Li and Prof. Jennifer Laaser for their time and being part of my Ph.D. defense committee. I would like to thank Prof. Alexander Star for his time during the comprehensive examination and dissertation defense. Thank you, Dr. Michelle Ward for our friendship, your guidance and support. I am now confident that as a woman in STEM I can accomplish anything, and this is thanks to you.

I also thank all of my former and current group members: Prof. Shichao Zhao, Dr. Sumedh P. Surwade, Dr. Raúl García Rodríguez, Dr. Zhiting Li, Dr. Feng Zhou, Rickdeb Sen, Hyojeong Kim, Anqin Xu, Muhammad Salim, Christopher Kurpiel, Dong Wang, Mina Kim,

Justin Hurst and Nathan Tolman for their help and suggestions during my graduate studies. You are all wonderful friends and scientists and I am confident you will be successful. Best of luck in your future endeavors. I would also like to thank the undergraduate researchers Anne Sendecki and Autumn Blackburn for their dedication and effort in our projects.

Finally, this dissertation would not be possible without the support from friends and family. My grad school friends outside the lab and everyone that always encouraged me will be forever in my heart. My parents, José and Nixa Ricardo and siblings, Kevin and Kaitlin Ricardo provided me their support, advice and love. Finally, I would like to thank my wonderful husband, Genariel Hernández. His incredible support during the easy and not so easy times during my graduate studies demonstrated his infinite love for me. I am so lucky I get to share my life adventures with you. Mi amor, our time is finally here... Te amo.

1.0 INTRODUCTION

1.1 CARBON MATERIALS

1.1.1 Highly Ordered Pyrolytic Graphite (HOPG)

HOPG crystal structure is characterized by an arrangement of a hexagonal pattern of carbon atoms stacked in parallel layers; each layer is the single-atom thick sp^2 material called graphene.[1] The carbon layers are stacked in the ABAB lattice conformation, shown in Figure 1A. Strong bonding forces are present between the carbon atoms in lateral planes, whereas weaker Van der Waals forces govern in between the planes.[2] In each layer, the atoms form a grid of hexagons with distances between atoms equal to 1.415 Å while the distance between layers is equal to 3.354 Å,[3] giving a theoretical density value of 2.265 g/cm^3.[3, 4] Experimental results demonstrated that the density of HOPG ranges from 2.04 to 2.24 g/cm^3.[4]

Unlike graphite found in nature, HOPG is of much higher purity. First reports of the oriented pyrolysis of graphene by Blackman *et al.* surfaced over 50 years ago. HOPG discs were created by annealing pyrolyzed graphite at a temperature of 3000 - 3700 ˚C under a compressive pressure of 10 kg cm^{-2}.[4, 5] HOPG is a highly-ordered form of high-purity pyrolytic graphite, with impurity levels in the order of 10 ppm ash.[4] Nowadays, HOPG is commercially available in a variety of size, shape and quality, shown in Figure 1B.[6, 7] The weak forces between sheets allow

thin layers of the graphite to be removed. This can be achieved by using Scotch tape, pressing flat on the surface and pulling to remove the top few layers, producing a freshly cleaved surface.[8] Mechanical cleaving using a razor blade is another method to obtain a fresh HOPG surface. The razor blade is inserted parallel to the basal plane and is slowly worked through the sample.[8]

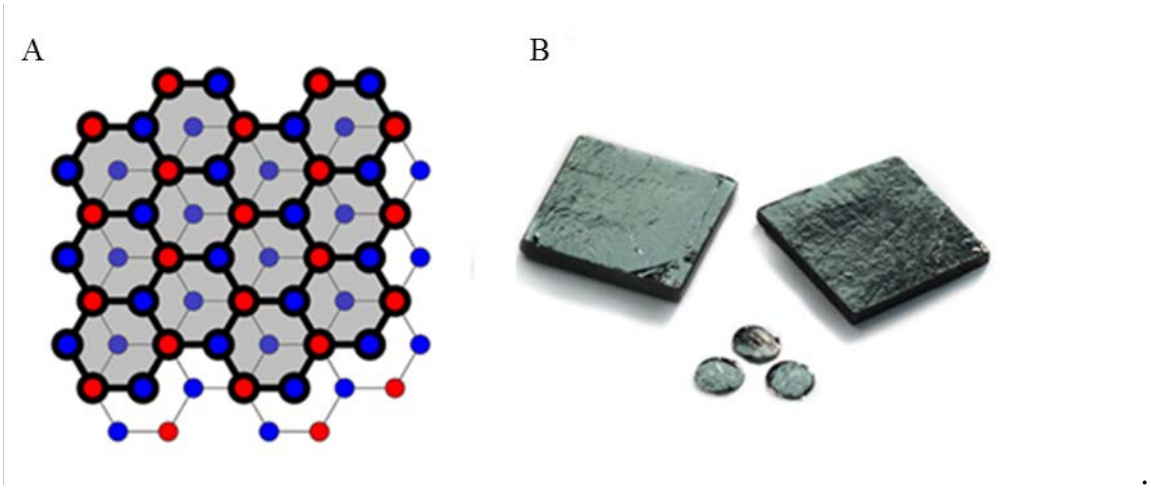

Figure 1. (A) AB lattice conformation of HOPG. (B) Photographical image of commercially available HOPG.

An important feature of pristine HOPG is that the basal plane is relatively inert to chemical reactions at room and high temperatures.[3, 9] Recent reports have shown that the basal plane can support fast electron transfer and electrochemical activity is observed in the absence of the more reactive internal step edges.[10-13] HOPG crystals are of interest for X-ray diagnostics of hot dense plasmas. Their unique crystal plane structure enables them to be highly efficient in X-ray diffraction instruments.[14, 15] Another feature of HOPG is its mosaicity accompanied by a high integral reflectivity, which is an order of magnitude higher than that of all other known crystals in an energy range between 2 keV up to 10 keV.[15] These characteristics make it possible to

efficiently collect optical measurements, which could be relevant for X-ray diagnostic tools and spectrometers.[15]

HOPG provides a versatile supporting surface, making HOPG an ideal substrate for SPM and AFM imaging. HOPG also offers a well-defined geometry with smooth surfaces that can remain relatively clean in ambient laboratory conditions.[16] Therefore, HOPG can be used to immobilize, study and image a wide-variety of materials such as metal clusters,[17] nanoparticles,[18-21] nanobubbles,[22, 23] organic heterostructures[24] and biomolecules including DNA,[25, 26] proteins[27, 28] and biological membranes.[29]

In the past, there was a conventional notion that HOPG was hydrophobic, with a water contact angle within the 75 - 98˚ range.[30-32] Morcos reported WCA of 84.2° on exfoliated graphite and 83.9° on highly oriented graphite.[30, 31] Figure 2A depicts the WCA of a HOPG sample, demonstrating its hydrophobicity.[33] Despite the dominant view that HOPG is hydrophobic, great effort has been made to demonstrate its hydrophilic properties. Several reports have demonstrated that the contact angle of freshly-cleaved HOPG ranges from 35 to 65˚.[34-37] Figure 2B depicts the WCA measurement of mildly hydrophilic HOPG. Kozbial and Li attributed the increase of the water contact angle over time and the reported hydrophobicity of HOPG to adventurous airborne hydrocarbon contamination on the surface.[35, 36, 38] This surprising finding points to a previously unknown factor that opens new opportunities to control the interaction of hydrophilic materials with graphitic surfaces. Taking recent findings into account, my interest is focused on the fundamental study of the interaction between exfoliated HOPG with hydrophilic materials, specifically DNA origami nanostructures.

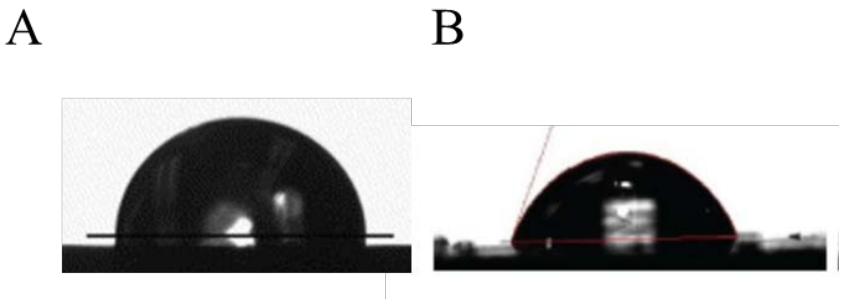

Figure 2. WCA measurements on freshly-cleaved HOPG. WCA measurements demonstrates the hydrophobic (A) and hydrophilic (B) properties of the surface. The difference in wettability is attributed to airborne hydrocarbon contamination on the surface. Figures reprinted with permission from: Reference 33, Copyright © 2006 Elsevier, reference 38, Copyright © 2016 American Chemical Society.

1.1.2 Graphene

Graphene is a two-dimensional single-atom-thick monolayer of sp^2 carbon atoms arranged in hexagons. The extended honeycomb network has a carbon-carbon bond length of 1.42 Å and a lattice constant of 2.46 Å.[39] Graphene is also the simplest allotrope of carbon, making it the base of fullerenes, carbon nanotubes and graphite, displayed in Figure 3.[40] Graphene was first defined in the 1980's and 1990's by Boehm and coworkers.[41, 42] The scientific community was skeptical that graphene could be physically isolated. It all changed in 2004 when Novoselov and Geim isolated and characterized single layer graphene from exfoliated graphite.[43] Their discovery revolutionized the scientific community and the research to uncover the properties of graphene grew exponentially.[44] With many of its potential applications being discovered, graphene could be useful in many areas of nanotechnology and materials science.

One of the most important properties of graphene is its high electron mobility.[45] The electrons on graphene behave as massless particles with little scattering. When a gate voltage is applied, this results in a high carrier mobility at room temperature of ~200,000 $cm^2\ V^{-1}\ s^{-1}$.[46] Another property of graphene is its high thermal conductivity at room temperature, measured to

be 5300 W m^{-1} K^{-1}.[47] The light absorbance of single-layer suspended graphene is 2.3 % and the absorbance increases in a linear relation when layers are added.[48] Finally, graphene also demonstrates a strong mechanical property with a tensile modulus of 1.0 TPa, making it the strongest material ever measured.[49, 50] These intrinsic properties make graphene a valuable material for electronic applications.

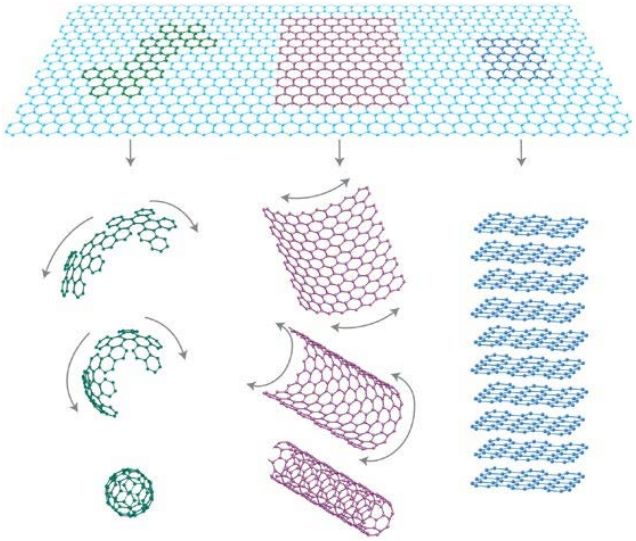

Figure 3. Graphene is the building material for carbon materials of other dimensionalities. Figure reprinted with permission from reference 40, Copyright © 2009 Nature Publishing Group.

1.1.2.1 Synthesis methods

The micromechanical exfoliation of graphene from HOPG was first introduced in 2004 by Novoselov and Geim.[43] The process consisted of peeling repeatedly graphite from the HOPG surface with Scotch tape, until several layers were obtained and transferred to a Si substrate for characterization. A disadvantage the exfoliation process presents is the fact that is not scalable and the size of the graphene cannot be controlled. Regardless, this method was a breakthrough in the synthesis of graphene and a race ensued to synthesize and study pristine single-layer

graphene. Other synthesis methods have been reported in literature such as the epitaxial growth of graphene from SiC,[50, 51] the unzipping and subsequent reduction of CNTs,[52] among other methods,[53] each of them with potential applications in different areas of materials science. My interest is focused on the liquid phase exfoliation of graphite and CVD graphene synthesis methods.

Graphite oxide can be prepared using the Hummers method and is then exfoliated in aqueous solutions by ultrasonic exfoliation to obtain graphene oxide.[54] Stankovich *et al.* proposed the reduction of graphene oxide using hydrazine at 100 ºC for 24 h.[55, 56] Furthermore, Li *et al.* studied the stabilization mechanism of reduced graphene oxide in hydrazine.[57] The chemically converted graphene oxide is stable in ionic solutions due to the electrostatic interaction between graphene and the ionic reagents present from the reduction step. A major setback on this process is the fact that graphene oxide is not always fully reduced and the electronic properties of reduced graphene oxide are affected. Additionally, the morphology of graphene is very rough and does not present intrinsic properties as promising as pristine graphene.

Almost a decade ago, Hernandez *et al.* developed a method to produce graphene through the exfoliation of graphite in organic solvents such as NMP, DMF and GBL.[58] Figure 4 shows the result of the exfoliation process, a gray solution with colloidally-stable graphene. They claimed that this was possible because the energy required to exfoliate graphene is balanced by the solvent–graphene interaction for solvents whose surface energies match that of graphene. Although this process is very similar to the reduction of graphene oxide, the oxidation and reduction steps are eliminated, limiting the potential damage to the graphene surface. While Hernandez reported low concentrations of graphene (< 0.01 mg mL^{-1}), Khan *et al.* demonstrated

that longer sonication times and the usage of probe sonication improved the concentration of graphene in solution up to 35 mg mL^{-1}.[59, 60] Other types of organic solvents have been tested for the exfoliation of graphite to obtain single and few layer graphene.[61, 62] A disadvantage of this process is that the boiling point and toxicity of the solvents hinders applications where solvent residues may greatly deteriorate the performance of devices.[63] To address this issue, the exfoliation of graphene was reported in volatile solvents.[64, 65] Additionally, a method was proposed to transfer graphene dispersions from high boiling point solvents into low boiling point solvents via solvent exchange.[66]

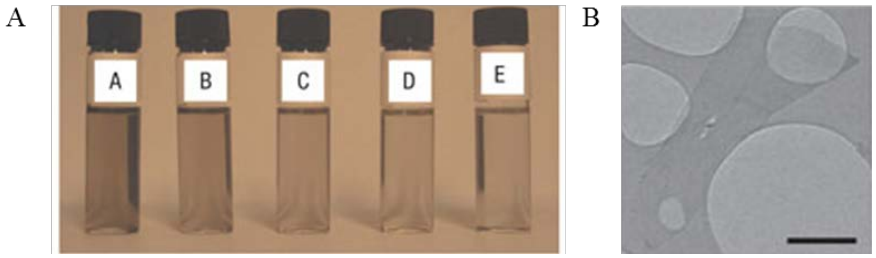

Figure 4. (A) Exfoliated single and few-layer graphene in NMP with concentrations ranging from 6 µg mL^{-1} to 4 µg mL^{-1}. (B) TEM image of an exfoliated single layer graphene. Figures reprinted with permission from reference 58, Copyright © 2008 Nature Publishing Group.

The exfoliation of graphene using surfactants as stabilizers was first reported by Loyta *et al.*, where they used the ionic surfactant SDBS to exfoliate graphite.[67] After ultrasonic sonication and centrifugation, low concentration (0.01 - 0.3 mg mL^{-1}) of single and multilayer graphene sheets were obtained with little to no defect. Other reports in literature explored the usage of anionic,[68-70] cationic[71] and nonionic[72] surfactants as stabilizers. One significant setback of this exfoliation method is that the surfactant cannot be completely removed from the graphene surface, affecting the conductivity and performance of films, composites and electronic devices.[63]

The exfoliation of graphite in solution without organic solvents and surfactants has gained interest in the scientific community over the last seven years. We reported the exfoliation of few layer graphene in a weakly basic aqueous solution using NaOH as the stabilizing agent.[73] Our mechanism proposed that graphene suspension is stabilized by electrostatic repulsion with hydroxide ions being adsorbed onto the graphitic surface. Before our research project was published, there were no reports regarding the liquid-phase exfoliation to produce graphene without the aid of surfactants or organic solvents. Additionally, fundamental studies such as the recycling of the unexfoliated graphite, the effect of different ions and various sources of graphite and the effect of their structural features had not been explored. This research provides the low-cost production of graphene that has the potential to be scaled up for industrial applications.

Other reports have surfaced where other stabilizers such as urea and even liquid detergent and soap have been used.[74-76] Srivastava *et al.* claimed the exfoliation of HOPG and graphite in water, attributing the suspension stability to n-type doping.[77] Additional graphene stabilizers in solution include the usage of polymers,[78] pyrene derivatives[79] and ionic liquids.[80, 81] Finally, other exfoliation methods such as shear exfoliation and electrochemical exfoliation of graphite have also been developed and reported in literature.[75, 82-84]

An alternative synthesis method to obtain high-quality monolayer and multilayer graphene is via CVD. The concept of creating multilayer graphene on a transition metal substrate for catalysis and industrial applications has been studied for over half a decade.[85] Li and Rouff developed a simple, straightforward method for the CVD synthesis of single layer graphene using copper foil as a substrate that has expanded the ability to synthesize and analyze single layer graphene.[86] Since then, great effort has been made to create graphene at a large scale with reports of roll-to-roll production of 30-inch graphene films.[86-88]

The growth of graphene using copper as the substrate is the most popular method for preparing large-area, high quality monolayer graphene. Figure 5A depicts the experimental setup of CVD graphene synthesis.[89] In the CVD method reported by Li *et al.*, copper foil was used as a metal substrate, put into a furnace and heated under low vacuum to around 1000 °C.[90] The heat under the presence of H_2 anneals the copper increasing its domain size and eliminating the oxide from the uppermost layer. Methane gas is then flowed through the furnace; its stability at high temperatures makes it the best carbon source.[91] The hydrogen catalyzes the reaction between methane and the surface of copper, causing the carbon atoms from methane to be deposited onto the surface of the metal through chemical adsorption (Figure 5B). The growth mechanism on copper surface is a surface adsorption process owing to the low solubility of carbon atoms on copper, offering a path to grow monolayer graphene based on a self-limiting process.[92]

The most common method to transfer graphene to a solid substrate was developed by Li *et al.* A protective polymeric coating such as PMMA is deposited on top of the graphene thin film. The underlying copper that also contains monolayer graphene is etched in an iron chloride solution.[90, 93] The graphene film is transferred to a cleaning solution to remove the acid from the graphene. The sample is then collected with the desired substrate and the PMMA is removed using acetone or other organic solvents such as dichloromethane.[90]

Although the optimization and mechanism of the CVD synthesis have been greatly developed and improved, some drawbacks still exist. For example, the size of single crystals is still limited to the centimeter range because of the low rate growth and copper domains.[93] Additionally, there are still various defects such as wrinkles and vacancies present, even on single crystal graphene.[94] The transfer process also introduces more impurities to the graphene

surface. Finally, the synthesis and transfer method is not cost-effective for industrial applications.[89]

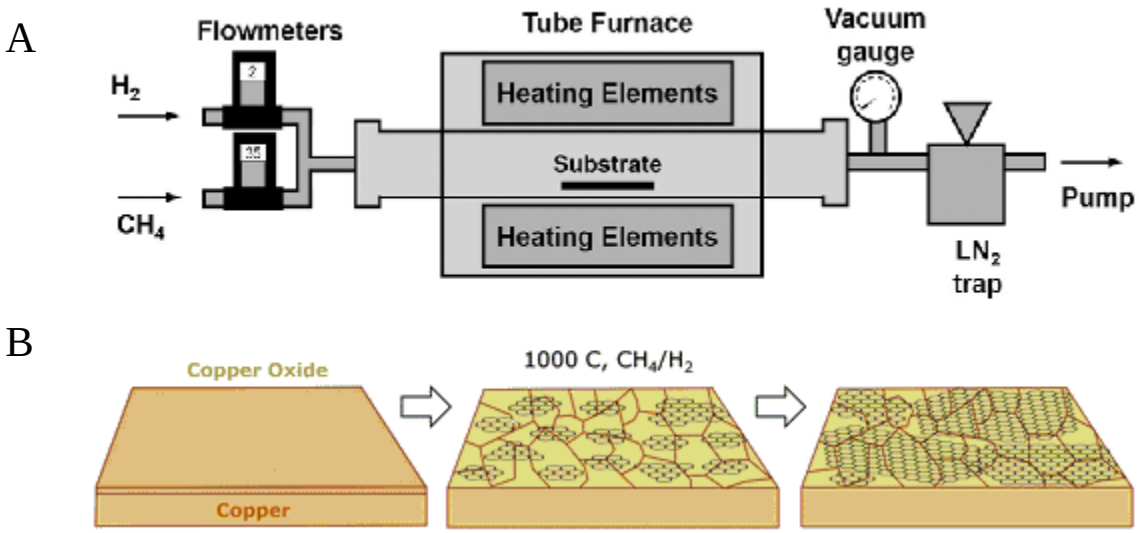

Figure 5. (A) Experimental setup for the CVD growth of graphene on a metal substrate. (B) Schematic illustrating the CVD growth mechanism of single layer graphene on a copper substrate. Figures reprinted with permission from: reference 89, Copyright © 2016 WILEY-VCH Verlag GmbH & Co. (A), reference 94, Copyright © 2010 Royal Society of Chemistry (B).

1.2 DNA NANOTECHNOLOGY

DNA, the molecule in charge of coding and carrying genetic information on most living organisms, has gained interest as a building block for the fabrication of nanomaterials. DNA is a polymer of nucleotides, which are themselves composed of a sugar, a base and a phosphate group. The bases of DNA are adenine (A), cytosine (C), guanine (G), and thymine (T), which are subject to complementary pairing; each pyrimidine base (C and T) combines with one purine base (A and G).[95] That is, adenine pairs with thymine (A-T) and guanine pairs with cytosine (C-

G) by hydrogen bonding.[96] Nowadays, DNA goes beyond the replication of genetic information; it is the center point of a new and exciting branch of materials science.

DNA nanotechnology utilizes the precise and predictable nature of DNA base pairing to create 1D, 2D and 3D nano- and micro- structures.[97] One important aspect for designing and engineering DNA nanostructures is its molecular recognition ability through the Watson-Crick base pairing rules. This makes DNA hybridization and self-assembly process programmable, enabling the precise design of well-ordered molecular structures with controllable size and configuration. The DNA nanotechnology field was introduced in the 1980's where the construction of a 4-way arm junction of DNA and connecting networks through sticky ends was proposed.[98] After a few decades of development, this field has been exponentially explored and a wide-variety of DNA nanostructures have been reported.[99-106] The following sections provide an overview of the progress in the fabrication of DNA nanostructures, its properties and interaction with carbon materials.

1.2.1 DNA tiles

In 1982, Nadrian Seeman pioneered the field of DNA nanotechnology by creating a four-way branched junction structure composed of four complementary ss-DNA strands tailed with sticky ends.[98] The four-arm junctions were structural analogues of the Holliday junctions found in genetic recombination complexes.[107] Nonetheless, the instability of the Holliday junctions only allowed for the fabrication of small lattices.[108] A more rigid double-crossover DNA tile was later developed to overcome the instability of the four arm junctions by joining two DNA double helices with a single strand that begins on one helix and switches onto an adjacent helix, generating well-defined lattices with predesigned periodicity.[109] Since then, more complex

crossover DNA tiles have been created with more junctions that enabled assembly of nanotubes,[110, 111] 2D structures such DNA crystals,[112, 113] arrays[114] and complex shapes[115] and 3D arrangements including cubes,[116] tetrahedrons,[117] octahedrons,[118, 119] buckyballs,[120] and crystals.[121] Figure 6 depicts several types of tile DNA nanostructures reported in literature.

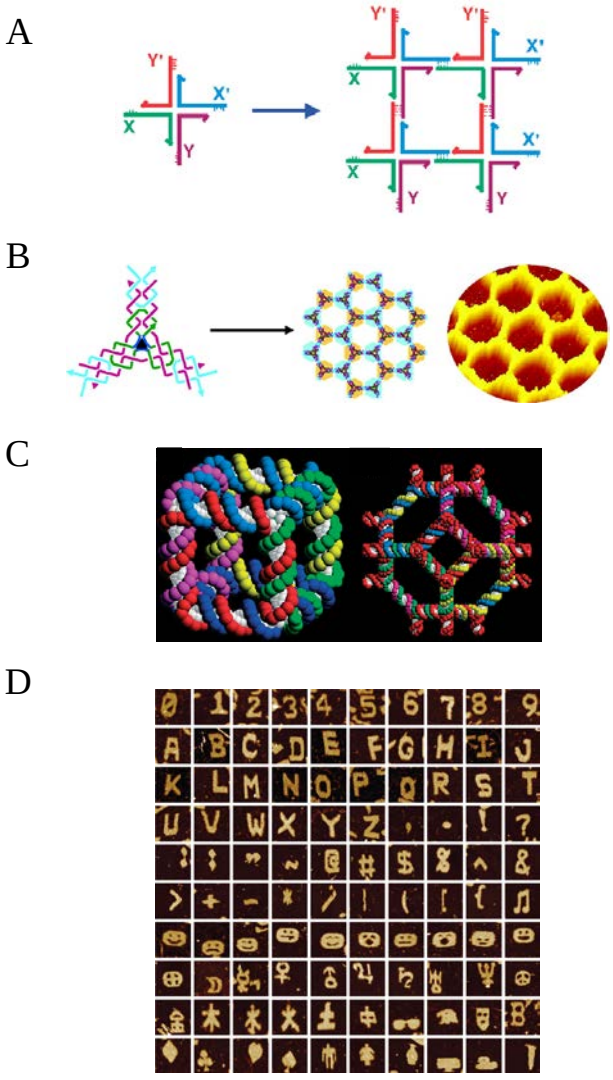

Figure 6. Examples of tile-based DNA self-assembly. (A) 4x4 sticky-end assembly of branched molecules. (B) Three-point star DNA crossover motif that can self-assemble into a hexagonal 2D lattice. (C) Tile-based 3D nanostructures. A cube (left). A DNA crystal (right). (D) AFM images of complex 2D ss-DNA tiles. Reprinted with permission from: reference 97 Copyright © 2005 IOP Publishing Ltd (A, C), reference 114 Copyright © 2005 American Chemical Society (B), reference 115 Copyright © 2012 Nature Publishing Group (D).

1.2.2 DNA origami

A decade ago, Rothemund demonstrated the idea of assembling DNA nanostructures via the DNA origami method.[122] A long ss-DNA scaffold, generally the M13mp18 bacteriophage genome is folded into shapes by short synthetic oligonucleotides, called staple strands. Aided by a computer program, one can design a particular shape and modify the staples to bind into specific regions of the scaffold. The resulting structure has a size of approximately 100 nm and a resolution of about 6 nm. One major advantage of the DNA origami synthesis is its straightforwardness. This method is a one-pot process that simply involves the thermal annealing and cooling of the scaffold and the strands. Additionally, precise stoichiometry is not necessary and the purification step can be eliminated.[122]

The process of fabricating DNA origami nanostructures involves five steps. The first step is to build a geometric model of a DNA structure that will approximate the desired shape. The shape is filled from top to bottom by an even number of parallel double helices, idealized as cylinders (Figure 7A). Each cylinder unit is made of 10.67 base pairs, the equivalent of 1 turn on the double-helix. Crossovers are added to designate positions at which strands running along one helix will switch to an adjacent helix. The second step involves the folding of a single long scaffold strand into a pattern so that it comprises one of the two strands in every helix (Figure 7B). The third step is the design of the staple strands, that are complementary to the scaffold and periodic crossovers (Figure 7C) using computer programs such as SARSE and caDNAno are created.[123, 124] To hold the helices together, a periodic array of crossovers is incorporated every 1.5 turns (16 base pairs). In the fourth step, the twist of scaffold crossovers is calculated and their position is changed to minimize strain (Figure 7D). Wherever two staples meet there is a nick in the backbone. Nicks occur on the top and bottom faces of the helices. In the last step, pairs of

adjacent staples are merged across nicks to yield fewer, longer staples (Figure 7E). Larger staples have superior binding specificity and higher melting temperatures. To prepare the nanostructures, the DNA scaffold and staples are mixed, annealed and slowly cooled to room temperature at a rate of 1 ˚C min^{-1}. As the DNA cools, the staples will bind to the scaffold into the desired shape, yielding the anticipated DNA origami shape (Figure 8A).

Moreover, several groups have focused on scaling-up DNA origami by using longer scaffolds,[125] and the fabrication of a "super origami", a method where an origami structure serves as a large staple.[126] The 3D DNA origami fabrication, including the assembly of twisted and curved 3D structures, a box with a controllable lid and a tetrahedron has also been reported (Figure 8B).[127-132] Additionally, DNA origami can be modified with molecules and structures such as gold and silver nanoparticles,[133, 134] carbon nanotubes[135] and proteins.[136, 137] The capability to modify DNA origami nanostructures brings the opportunity to expand the usage of DNA origami on multiple applications such as nanofabrication,[100, 138-140] patterning,[103, 141, 142] lithography,[143, 144] sensing[145-147] and drug delivery.[148-150]

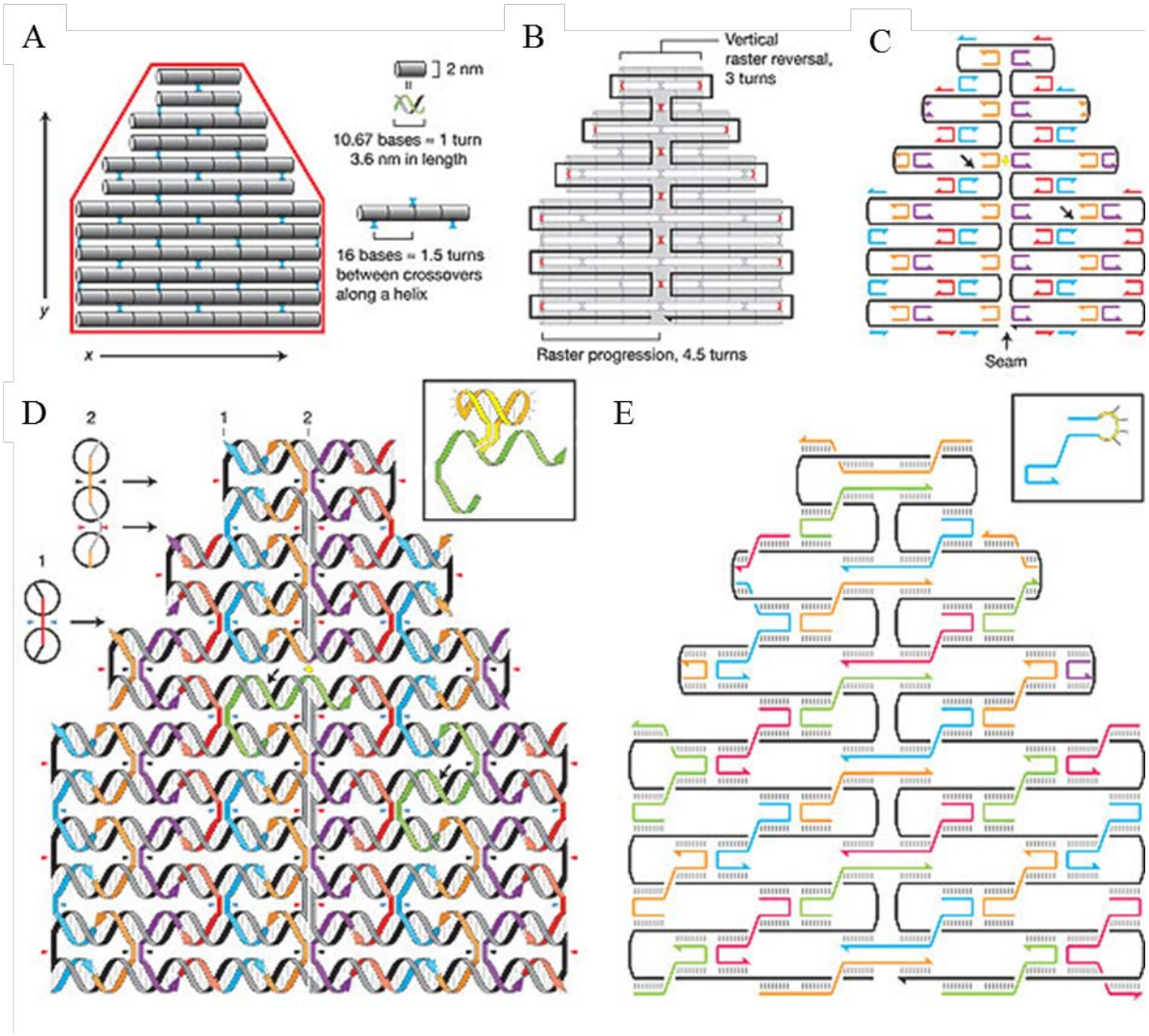

Figure 7. Design of a DNA origami structure. (A) The schematic design of a shape (red) approximated by parallel double helices joined by periodic crossovers (blue). (B) A scaffold strand (black) runs through every helix and forms more crossovers (red). (C) As first designed, most staples bind two helices and are 16-mers. Arrows point to nicks that can be sealed to create longer strands. (D) Helical drawing of (C). (E) A finished design after merges and rearrangements of the staples along the seam. Most staples are 32-mers spanning three helices. Figure reprinted with permission from reference 122, Copyright © 2006 Nature Publishing Group.

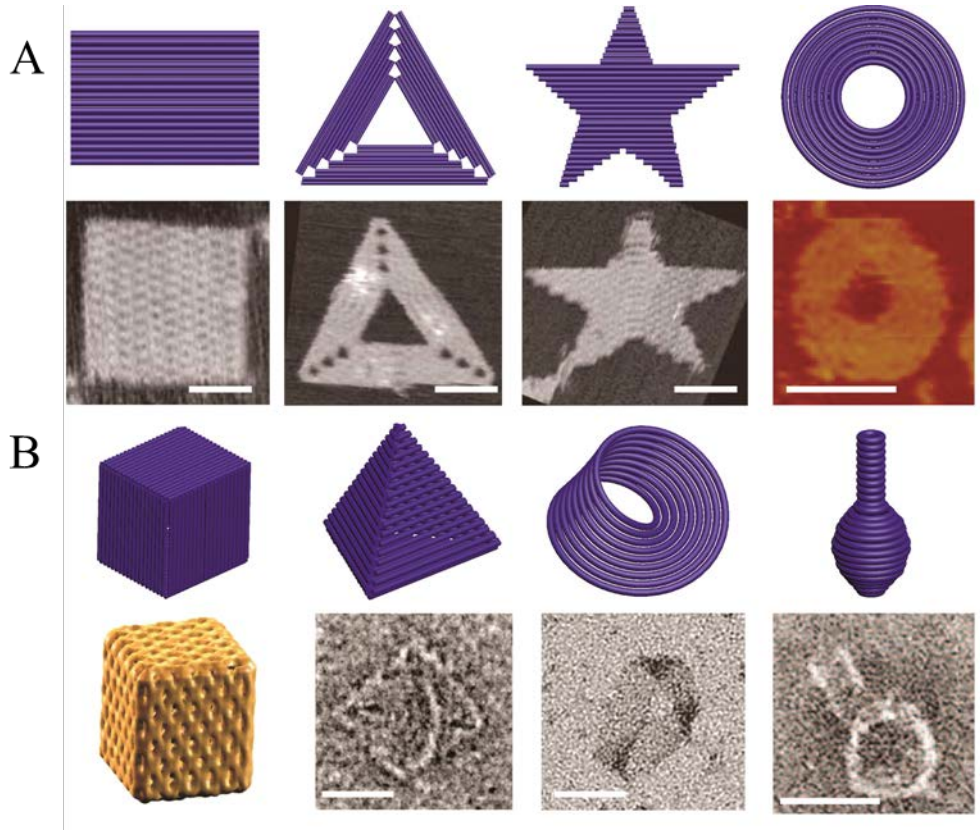

Figure 8. Schematic drawing and corresponding microscopy images of 2D (A) and 3D (B) DNA nanostructures prepared using the origami synthesis method. Figures reprinted with permission from: reference 140, Copyright © 2017, American Chemical Society (A, B), reference 122, Copyright © 2006 Nature Publishing Group (A), reference 128, Copyright © 2011 The American Association for the Advancement of Science (A,B), reference 131, Copyright © 2009, Nature Publishing group, (B) reference 117, Copyright © 2009, American Chemical Society (B), reference 132, Copyright © 2010, Nature Publishing Group (B).

1.2.2.1 Chemical and thermal stability of DNA origami nanostructures

One major setback of DNA origami from its potential applications is its low chemical stability. Being an organic structure with hydrogen bonding instead of non-covalent bonding, the degradation and denaturation of the DNA nanostructures is inevitable under certain conditions. For example, DNA origami is synthesized in an aqueous solution with a buffer of neutral pH. When the pH of the buffer is too low (~ 4) or too high (~ 12), DNA origami is deformed after its deposition on a solid substrate.[151]

It has been reported that DNA origami triangles are stable under certain conditions in the presence of chaotropic agents such as urea and guanidinium chloride.[152] Deformation is only observed at high molar concentrations of the chaotropic agent (up to 6 M) and mild temperatures (37 - 42 ˚C). The deformation of the structure was analyzed and it was concluded that the staples that connect the trapezoidal domains used to form the DNA triangle are a weak point on the nanostructure. This finding brings the opportunity to enhance the DNA origami stability by photo-cross-linking or redesigning the bridging staples toward higher melting temperatures to employ in applications such as the study of biomolecular processes.[152, 153]

The Mg^{2+} ions in the buffer play an important role in the origami stability. The ions prevent the repulsion among helices during and after folding of the origami by neutralizing the negative charge of the phosphate groups present on the DNA backbone.[154] Our research group reported that when a solid substrate containing DNA origami triangles is immersed in a NaCl solution, the DNA nanostructure degrades into its trapezoidal domains. That is, Mg^{2+} is replaced by Na^{+} ions that accumulate on the nanostructure surface, leading to the shape deformation and structural defects.[151] Nonetheless, Na^{+} ions have been used at high concentrations (1 - 2.4 M compared to 12.5 mM for Mg^{2+} in a buffer solution) to synthesize multi-layer DNA origami nanostructures.[155]

Temperature is another factor that affects the stability of DNA origami. The melting temperature of ds-DNA varies from 50 ˚C to 75 ˚C, depending on the base sequence and buffer composition.[156] When the DNA origami is deposited on a substrate such as mica and Si/SiO_2, the melting temperature increases due to the interaction between the backbone of the DNA and the substrate, with Mg^{2+} being a stabilizing agent.[157] Our research group showed that triangular DNA origami deposited on a Si/SiO_2 substrate wafer decomposed upon heating to 200 ˚C.[151]

One peculiar feature observed was that the triangular feature was preserved, even at 500 ˚C. The triangular shape observed is likely composed of an inorganic residue (*e.g.,* magnesium phosphate) from the decomposition of the DNA triangle.[151] To further optimize the potential applications of DNA origami, it is important to preserve the shape, height and overall structure integrity of the DNA structure of interest at elevated temperatures.

1.3 INTERFACIAL INTERACTION OF DNA WITH GRAPHITIC MATERIALS

Regarding DNA-HOPG interactions, early studies by Oliveira-Brett *et al.* demonstrated the electrochemical immobilization of calf-thymus ds-DNA on a HOPG electrode surface.[158] They also analyzed the effect of pH and applied potential on the adsorption process and different adsorption and self-assembly behaviors were observed.[159] Kawano *et al.* produced monolayers of self-assembled ds-DNA by surface modification of the HOPG substrate through contact with a $MgCl_2$ solution under an externally applied electric potential.[160]

It has been shown that DNA molecules can be freely adsorbed on HOPG surfaces.[25, 158, 159, 161-163] However, these investigations are focused on the structures of polydispersed DNA at high concentrations, in which dense DNA networks have been observed. In these studies, single DNA molecules are difficult to be identified. In an effort to create a monolayer of DNA on HOPG, the effect of different divalent ions (Mg^{2+}, Ni^{2+} and Cu^{2+}) on the free adsorption of circular ds-DNA was investigated via AFM.[164] The results revealed that the topography and height of the DNA significantly varied, depending on the ion used for the deposition. Recently, Zhang and Hu deposited and rearranged individual long ds-DNA coils into a spiral-like pattern by rotating a water drop on top of the deposited DNA.[165, 166]

Directed assembly of DNA molecules was for the first time reported on a dodecylamine-modified layer on HOPG.[167] DNA molecules were oriented along the directions of three-fold symmetry of the underlying pattern at room temperature. A similar effect of DNA assembled on a stearylamine-modified HOPG surface was also investigated.[168] In another work, different scenarios of DNA adsorption on modified HOPG were reported for three types of nanotemplates: stearic acid, octadecyl amine and stearlyl alcohol.[169, 170]

A strong binding interaction between ss-DNA and exfoliated graphene was reported by Husale *et al.*[171] They also demonstrated preferential orientation of the ss-DNA towards the graphene lattice. It was concluded that graphene can bind ss-DNA via hydrophobic and π-π stacking interactions between the ring structures in the nucleobases and the hexagonal lattice of graphene. DNA can also electrostatically interact with graphene basal planes; ss-DNA showed a much stronger affinity towards graphene than ds-DNA, probably due to electrostatic repulsion between the negative-charged DNA backbone and graphene.[172]

Ferapontova *et al.* created a DNA origami rectangle that was self-assembled on a cysteamine-modified HOPG surface and was later used for nanomechanical applications.[173] The origami was stable under pH and electric field changes.

We recently reported the deposition of DNA origami triangles onto HOPG without any surface or DNA nanostructure modification.[174] Comparable results have been observed with cross-shaped DNA origami modified with streptavidin protein.[175, 176] In both cases, the nanostructures show structural rearrangement when deposited on HOPG due to the exposure of the DNA base to interact with the graphite surface. We were interested in the deposition of DNA origami on HOPG because HOPG is the model to understanding the behavior of other graphitic materials such as graphene and carbon nanotubes. Being more hydrophilic than previously

believed, this study could bring new insight on the intrinsic properties of HOPG and DNA origami. In literature, the mechanism of the deposition process, the type of interaction and the effect of the wettability of HOPG had not been reported. Finally, we wanted to find a suitable application for the deposition such as CVD growth of semiconductors solely on the DNA triangle.

DNA nanostructures have been deposited on graphene; however, most of these efforts involve a chemical modification of the substrate to enhance the DNA-graphene interaction such as doping[177, 178] and assisted immobilization.[179] Husale, *et al*. attempted to deposit DNA origami on graphene but the origami structures were not stable because they did not add Mg^{2+} in the buffer.[171] It was recently reported that cross-shaped DNA origami structure is deformed when deposited onto graphene.[176] In contrast, on 1-pyrenemethylamine modified graphene, DNA nanostructures were deposited without such deformation and were successfully used for subsequent metallization.[179] Finally, Yun *et al.* reported the nanopatterning of DNA origami on various forms of chemically modified graphene.[178] The DNA nanostructures were successfully deposited on graphene oxide and nitrogen-doped reduced graphene oxide but it was not possible on CVD graphene or reduced graphene oxide. They attributed the deposition to the attraction of Mg^{2+} ions to the negatively charged graphene oxide and the lone electron pair of nitrogen-doped reduced graphene oxide.

Recently, graphene has been employed to encapsulate objects such as water,[180-182] DNA[183, 184] and DNA nanostructures,[185] biosensors,[186] biological species[187, 188] and nanoparticles.[189] It has been demonstrated that graphene replicates the topography of the DNA molecules.[183, 185] A recent publication claimed that the encapsulation of DNA origami helps with the protection of the structures from water and AFM force manipulation.[185] A thermal stability

study of DNA origami under graphene has not been reported in literature. Additionally, the usage of DNA origami as a material to create site-specific atmospheric oxidation and its possible mechanism is unheard of. Analyzing the thermal stability of graphene and DNA origami could offer a better perspective in understanding the interaction and atmospheric oxidation of graphene using DNA origami.

1.4 STABILIZATION MECHANISM OF EXFOLIATED GRAPHENE IN SOLUTIONS: DLVO THEORY

Colloidal stabilizations often depend on the presence of a surface charge. The surface charge attracts counter-ions from the liquid, forming an electric double layer.[190] In a liquid dispersion media, ionic groups can adsorb to the surface of a colloidal particle through different mechanisms to form a charged layer. To maintain electroneutrality, an equal number of counterions with the opposite charge will surround the colloidal particles and give rise to overall charge-neutral double layers. The presence of this electrical double layer implies the presence of an attractive VDW attraction potential (V_A). Equation 1 shows the VDW potential for a colloidal suspension where *A* is the Hamaker constant (attraction parameter) and *D* is the particle separation.

$$V_A = \frac{-A}{12\pi D^2}$$

Equation 1. The Van der Waals attraction potential.

Since there are always strong attractive forces between similar colloidal particles, it is necessary to provide repulsion between the particles to promote stability. This repulsion should be at least as strong as the attractive force and comparable in range of the attractive interaction. An effective way to counterbalance the VDW attraction between colloidal particles is to provide the particles with Coulombic repulsion. In charge stabilization, it is the mutual repulsion of these double layers surrounding particles that provides stability. Equation 2 shows the Coulomb repulsion potential where ε is the permittivity of free space, a is the diameter of the particle, ζ is the zeta potential of a particle and κ is the Debye-Hückel screening length.

$$V_R = 2\,\pi\,\varepsilon\,a\,\xi^2\,e^{-\kappa D}$$

Equation 2. The Coulomb repulsion potential.

The DLVO theory suggests that the stability of a colloid in solution is the sum of the Coulomb repulsion and the van der Waals attractive forces.[190] Figure 9 shows the attractive Van der Waals potential, the Coulomb repulsive potential and the sum of both of these potentials.[191] The energy barrier from repulsive forces prevents the aggregation of two particles. If the particles collide with enough energy to surpass the barrier, the particles will adhere together, causing flocculation. We propose that the surfactant-free exfoliated graphene sheets are stabilized by electrostatic repulsion with the adsorption of hydroxide ions present in the solution. As explained on the DLVO theory, nearby graphene sheets feel a potential barrier, which opposes aggregation.

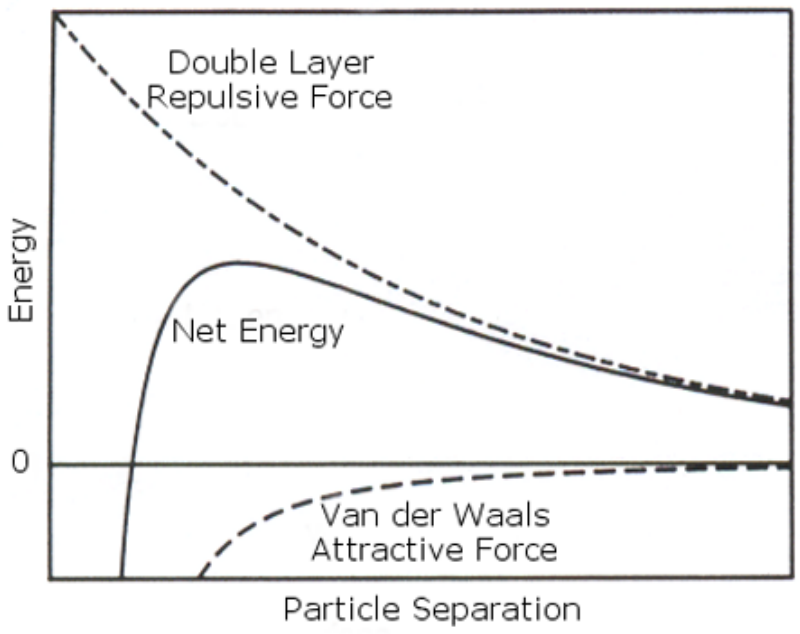

Figure 9. Schematic diagram of the variation of free energy with particle separation according to the DLVO theory. Reprinted from reference 191, Copyright © 2011, Malvern Instruments.

1.5 CHARACTERIZATION METHODS

1.5.1 Atomic force microscopy

AFM is a high-resolution form of scanning probe microscopy. It was invented by Binning, Quate and Gerbrtand and was first reported in 1986.[192] In recent decades, it has become a versatile technique in several fields for mapping and measuring nano- and micro-scale samples. AFM can resolve molecules on a surface[193] and even achieve atomic resolution.[194] AFM possesses many unique advantages. For example, while STM requires the sample to be conductive, AFM can work well with most types of materials. Compared with TEM and SEM, AFM can be employed

in more flexible environments. Finally, AFM has a higher resolution than SEM and is comparable to that of TEM and STM.

To obtain an AFM image, a cantilever (generally called tip) is oscillated near or on the surface of the sample. A laser beam is focused at the end of the cantilever and reflected to a photo diode detector. As the cantilever moves through the sample, the oscillation change of the cantilever is recognized. The feedback electronics produce a nullifying bias that keeps constant the force exerted on the cantilever. This signal is then recorded and converted into a map of the surface. The AFM instrument can be used in different types of setups such as contact, non-contact and tapping mode. AFM imaging is a common technique used to study the morphology and thickness of graphene and DNA nanostructures. Figure 10A depicts an AFM image of DNA origami triangles on a Si/SiO_2 substrate. In my study, tapping mode AFM was employed to study the morphology of the exfoliated graphene, DNA origami on HOPG and DNA underneath CVD graphene.

1.5.2 Transmission electron microscopy

TEM is another high-resolution characterization technique to obtain images, diffraction patterns among other properties with the potential of extremely high subatomic resolution. Developed in the 1930's, TEM is a microscopic system whereby an electron beam is transmitted through thin samples. An image is produced due to diffraction or mass-thickness contrast. This image is subsequently magnified by a set of electromagnetic lenses and commonly recorded with a CCD camera. The signals generated from the interaction between electrons and the sample can be collected to obtain information, such as the morphology, crystalline phase structure, chemical bonding and composition of the material studied. Since graphene is one atom thick layer, TEM is

a useful instrument to analyze its morphology and atomic properties. Figure 10B shows a TEM image of surfactant-free exfoliated graphene deposited on a holey-carbon mesh.[73] A low resolution TEM was used in our study to analyze the morphology and size of exfoliated graphene in an aqueous solution containing NaOH.

1.5.3 Raman spectrocopy

Raman spectroscopy is a molecular analysis technique used to observe low frequency vibrational modes in a target sample. Generally speaking, when a vibrational mode is excited, it presents an elastic behavior; the emitted photon has the same energy as the incident photon, a process called Rayleigh scattering. Raman scattering occurs when a small proportion of the incident laser photons are scattered at a frequency that is shifted from the original energy level.[195] Because of its strong vibrational modes, Raman spectroscopy is an effective method to study some properties of graphene.[196]

There are three major peaks on the graphene spectrum that provide information about its quality: the D, G and 2D bands.[196, 197] The G band (1580 cm^{-1}) is due to the in-plane symmetric stretching of the sp^2 carbon atoms. The intensity of the G band is proportional to the number of layers of graphene; as the number of layers increases, the peak intensity also increases.[198] The D (1350 cm^{-1}) and 2D (2700 cm^{-1}) bands originate from a second order process. The D band is not activated on pristine graphene. A disordered atomic arrangement on the graphene lattice must be present and is usually found on the edges. Thus, the D band can be used as an indicator to identify the quality of graphene.[199] Finally, the 2D band is an overtone from the D band and it does not require any defect for its activation. When the number of layers increases, the FWHM of the 2D band increases but the overall intensity decreases. Therefore, the ratio between the G

and 2D bands can be used to determine the number of graphene layers present. Figure 10C shows the Raman spectrum of the edge of graphene, showing the G, D and 2D bands.[200] This technique was used to study the morphology and quality of the exfoliated graphene with NaOH and CVD graphene used as an encapsulating agent to protect DNA origami nanostructures.

1.5.4 UV-Vis spectroscopy

UV-Vis spectroscopy is used to analyze the absorption of a sample at different wavelengths. Absorbance is a measurement of the light that does not pass through the sample and corresponds to the base ten logarithm of incident light, I_0, divided by light registered by the detector, I.[195] The absorbance, A, of the sample is a factor of the extinction coefficient at the specific wavelength, ε, the concentration of the species in the sample, c, and the path length of the light, b. The combination of these variables is known as the Beer-Lambert law, shown in Equation 3. Since graphene is a hexagonal lattice of conjugated carbon atoms, UV-Vis spectroscopy can be used to determine the concentration of graphene in a solution. The UV-Vis absorption spectra of graphene has a peak around 230 nm and it is related to π-π* transition of the aromatic C=C bond, shown in figure 10D.[73] In our study of the exfoliation of graphene in NaOH, we used the absorbance of each sample and an extinction coefficient value from literature to determine the concentration of graphene in an aqueous solution.

$$A = log_{10} \frac{I_0}{I} = \varepsilon \cdot c \cdot b$$

Equation 3. The Beer-Lambert Law.

1.5.5 Zeta potential

The immersion of a solid into an aqueous solution produces a region of electrical inhomogeneity at the solid–solution interface, forming an electric double layer within the solid. The inner layer of the electric double layer consists of ions or molecules that oppose the charge of the particle, called the Stern layer. A diffuse layer consisting of both the same and opposing charge of the particle grows beyond the Stern layer, which along the Stern layer forms the electric double layer. This electrostatic effect is only present a few nanometers from the particle, depending on the composition of the counter ion. The composition of the diffuse layer is dynamic and varies on factors such as pH and ionic strength.[201]

When an electric field is applied to the dispersion, the charged particles move towards the electrode of opposing charge. Within the diffuse layer there is a plane that separates mobile fluid from fluid that remains attached to the surface. This plane is called the slipping plane and the zeta potential is found at this interface. Zeta potential cannot be measured directly because it depends on the electrophoretic mobility (μ_e) of the particle of the charged particles. The electrophoretic mobility can be calculated using Equation 4 where v is the velocity of the particle and E is the applied electric field.

$$\mu_e = \frac{v}{E}$$

Equation 4. Electrophoretic mobility.

The zeta potential is then calculated using the Henry's equation (Equation 5) where ε_r is the dielectric constant, ε_0 is the permittivity in vacuum, ζ is the zeta potential, f(Ka) is the Henry's function and η is the viscosity of the medium at experimental temperature.

$$\mu_e = \frac{2\varepsilon_r \varepsilon_0 \xi f K_a}{3\eta}$$

Equation 5. Henry's equation.

In the case of exfoliated graphene, the electric double layer is much smaller than the size of the particle, the value of f(Ka) is taken as 1.5 and the Henry's equation is modified to the Helmholtz-Smoluchowski equation (Equation 6).

$$\mu_e = \frac{\varepsilon_r \varepsilon_0 \xi}{\eta}$$

Equation 6. The Helmholtz-Smoluchowski equation.

The zeta potential is determined by the surface chemistry. Even a small percent of a component, preferentially adsorbed at the surface of the particle, will largely determine the surface charge density, the resulting zeta potential, and the stability, or lack thereof, of the dispersion. There are several factors that affect the zeta potential of a particle. pH is the most influential parameter in aqueous solutions. The zeta potential greatly varies as the pH of the solution changes and becomes more positive or negative under acidic and basic environments, respectively. Using a titration curve of the zeta potential as a function of pH one can determine the point where the colloid loses stability and flocculate, called the point of zero charge or the

isoelectric point. The ionic strength of the solution also affects the electric double layer and consequently, the zeta potential value. As the ionic strength increases, the electric double layer is compressed and the zeta potential decreases.

The stability of a colloid is determined by the magnitude of the zeta potential value. Guidelines classifying dispersions with zeta potential values of ± 0–10 mV, ± 10–20 mV and ± 20–30 mV and > ± 30 mV as highly unstable, relatively stable, moderately stable and highly stable, respectively are common in literature.[191]

1.5.6 X-ray photoelectron spectroscopy

XPS is a quantitative surface-sensitive analysis technique that identifies the elemental composition of the surface of a material. XPS spectra are obtained by irradiating a sample with a beam of X-rays, while simultaneously measuring the kinetic energy and number of electrons ejected from a core level, usually within the first nanometers of the surface. The energy of the emitted photoelectrons is then analyzed by the electron spectrometer and the data is presented as a graph of intensity as a function of the binding energy of the electrons, shown in Figure 10F for oxygen. Each element (except hydrogen and beryllium) owes a characteristic set of XPS peaks corresponding to related characteristic binding energy values, which can be used to directly identify each element that exists on the surface of the material analyzed. Because of the surface sensitivity of the technique, XPS requires ultra-high vacuum conditions for proper operation and analysis. Additionally, XPS can be implemented with other techniques for further analysis, such as ion beam etching to perform depth profiling on the substrate. XPS analysis was used to analyze and quantify the CVD growth of SiO_2 on the DNA origami nanostructures deposited on HOPG.

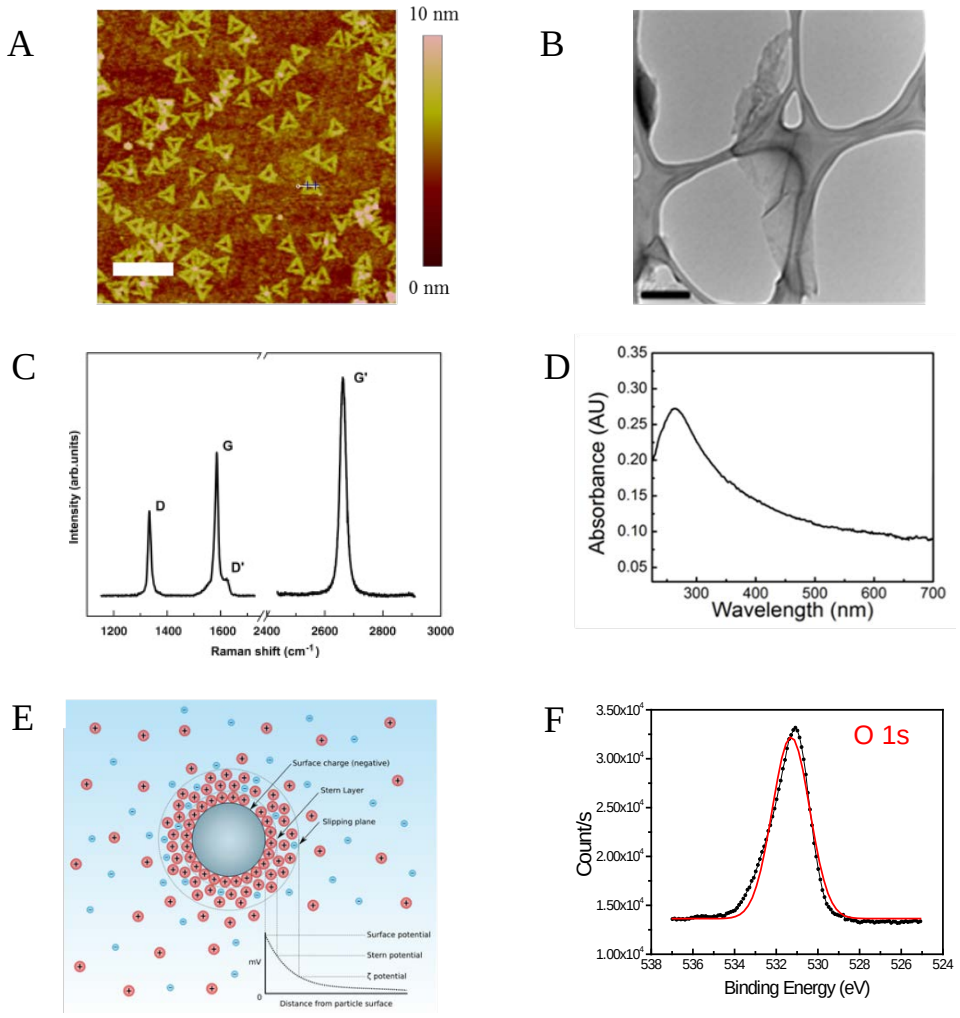

Figure 10. Characterization methods used to characterize graphitic materials and DNA origami triangles. (A) AFM image of DNA origami triangles on a Si/SiO_2 substrate. The scalebar represents 250 nm. (B) TEM image of exfoliated graphene in a weakly basic solution of NaOH. (C) Raman spectrum of a graphene edge where all the relevant peaks are shown: D, G and 2D (labeled here as G'). (D) UV-Vis spectrum of exfoliated graphene in a weakly basic solution of NaOH. (E) Diagram showing the ionic concentration and potential difference as a function of distance from the charged surface of a particle suspended in a dispersed medium. (F) O1s XPS spectra of a sample made of DNA origami nanostructures deposited on HOPG. Figures reprinted with permission from: reference 174, Copyright © 2017, American Chemical Society (A, F), 73, Copyright © 2014, Royal Society of Chemistry (B, D), reference 200, Copyright © 2009, Elsevier (C), reference 191, Copyright © 2011, Malvern Instruments (E).

2.0 SURFACTANT FREE EXFOLIATION OF GRAPHITE IN AQUEOUS SOLUTIONS

2.1 CHAPTER PREFACE

Materials contained in this chapter were published as a communication in *Chemical Communications*; figures used in this chapter have been reprinted with permission from: *Chemical Communications* **2014**, *50 (21)*, 2751 – 2754. Copyright 2014, Royal Society of Chemistry.

List of Authors: Karen B. Ricardo, Anne Sendecki and Haitao Liu.

Author Contributions: K.B.R and H.L. designed and directed the experiments. K.B.R. and A.S. conducted the experiments. All authors discussed the results. K.B.R. and H.L. wrote the manuscript with input from all authors.

2.2 INTRODUCTION

Graphene has found promising applications in energy storage, catalysis, surface coating, and electronics.[202-204] Since its discovery in 2004, a large number of methods have been developed to prepare graphene, such as micromechanical exfoliation,[43] chemical vapor deposition,[86] unzipping carbon nanotubes,[52] chemical reduction of graphene oxide,[57] solution phase exfoliation of graphite and graphite intercalation compound in organic solvents, water, or their mixtures.[58, 59, 62, 69, 205-207] Among these techniques, the aqueous-based exfoliation of graphite is one of the most promising ways to mass produce graphene at extremely low cost and with minimal environmental impact.[59, 67, 77]

Until very recently, all reported pure-aqueous-based exfoliations of graphite required a surfactant to stabilize exfoliated graphene in water. In a typical exfoliation process, graphite particles are suspended in an aqueous solution of a surfactant and subjected to a mild sonication. The sonication breaks up graphite into single- and multi-layer graphene flakes that are coated by the surfactant molecules. The surfactant coating provides the necessary steric and electrostatic repulsion to prevent the graphene flakes from aggregation.[58, 59, 67, 69, 75]

These surfactant molecules, while providing the necessary colloidal stability for the graphene dispersion, are electrically insulating and if not removed, could negatively impact the electrical performance of graphene-based devices. Unfortunately, removing these surfactant molecules is often not a trivial task because these molecules are chosen for their strong binding to graphene. In one study, it was found that surfactant accounts for 36 wt % of the film made from SDBS-stabilized graphene suspension.[67] In addition to their impact on the electrical

performance, the use of surfactants and the associated waste disposal also significantly increases the manufacturing cost and the environmental impact. Reducing or even eliminating the use of surfactants in the aqueous exfoliation of graphite could bring tremendous economic and environmental benefits.

Surfactants were considered to be essential in preparing aqueous dispersions of graphene because both graphene and graphite were believed to be hydrophobic and therefore could not be dispersed in pure water on their own. For example, graphite have long been believed to be hydrophobic with a water contact angle of about 90°.[30] However, recent studies showed that the hydrophobicity of graphene and graphite is actually due to airborne hydrocarbon contamination. A clean graphite surface is in fact mildly hydrophilic with a water contact angle of 64°.[36] This recent discovery suggests that the interaction between water and graphitic surface has been underestimated. More importantly, the fact that graphite is mildly hydrophilic raises the question as to whether a surfactant is absolutely required to stabilize graphene in water.

Herein we report that natural graphite can be exfoliated into graphene in a weakly basic aqueous solution without adding any organic surfactant. The exfoliation produced a suspension of multi-layer graphene flakes that are stable for up to several months. The concentration of the graphene dispersion is comparable to those produced by organic or surfactant-assisted exfoliation methods under the same experimental conditions. In addition to advancing the fundamental understanding of water-graphene/graphite interaction, this approach is also ideal for large-scale production of graphene dispersions using environment-friendly and inexpensive materials.

2.3 EXPERIMENTAL SECTION

2.3.1 Materials

Lithium chloride, potassium carbonate, potassium chloride, potassium hydroxide, sodium carbonate and sodium chloride were purchased from Sigma-Aldrich. Sodium hydroxide was purchased from Fisher Scientific. Water was purified by an Easypure water purification system from Thermo Scientific.

The following graphite samples were used in the study: graphite powder from Sigma Aldrich (SKU # 332461, batch # MKBB2274), graphenium flakes from NGS Naturgraphit, graphite fine powder from Riedel-de Haën (lot # 62910) and graphite powder of different grades (4827, TC307, 4052) from Asbury Graphite Mill Inc. (lot # 20669, 20966 and 23184, respectively).

The HOPG substrate used for the AFM imaging and exfoliation control experiments was purchased from SPI supplies (SPI-2 grade). The holey carbon mesh grid for the TEM analysis was purchased from Ted Pella Inc. The graphene film prepared for Raman measurements and the determination of the concentration of graphene was made by filtering a graphene dispersion through an alumina membrane (Cat. No. 6809-7013) with a pore size of 0.1 μm, purchased from Whatman. The ultrasonic bath used for all of the experiments was purchased from VWR International LLC. (model # 97043-468). The centrifuge was purchased from Eppendorf (model # 5804) The CVD furnace used for the annealing experiments was purchased from Thermo Scientific (Linderg Blue M, model number TF55030A-1) The Cu foil used for the annealing experiments was purchased from Alfa Aesar (99.8 %, 25 μm thick)

2.3.2 Characterization methods

UV-Vis spectra were taken using a GENESYS 10S UV-Vis with a Xenon Flash Lamp as the light source. Quartz cuvettes were used as sample holders. Each spectrum was collected using a wavelength range of 190 - 1100 nm. For plotting and histogram purposes, the wavelength reported was 500 nm.

AFM images were taken with a Digital Instruments Nanoscope IIIA from Veeco Systems in tapping mode in air using silicon tips with a resonance frequency of approximately 320 kHz. The images were collected at a scan rate of 1 Hz and 512 data points per line with a scan size identified by the scale bar in the image. Each sample was prepared by drop casting several microliters of the graphene suspension onto exfoliated HOPG. The sample was then spin-coated at a velocity of 3,000 rpm for 30 s and slowly dried using N_2 gas.

TEM samples were prepared by diluting a few milliliters of the graphene dispersion onto holey carbon mesh grids. The images were taken using the FEI Morgagni 268 D.

Zeta potential measurements were carried out on a Malvern Zetasizer Naano system with irradiation from a He-Ne laser at a wavelength of 633 nm. All measurements per sample were collected 3 times and the average was reported.

Room temperature micro-Raman spectra were conducted on a custom-built setup using 532 nm single-longitudinal mode solid-state laser with a spot size less than 1 μm. A 40x objective (NA: 0.60) was used in all the micro-Raman experiments. Each Raman spectrum was taken with 60 seconds of integration time with a low incident laser power of less than 1 mW at the entrance aperture to avoid laser induced thermal effect on graphene.

2.3.3 Sample preparation

In a typical sample preparation, 20.00 mL of an aqueous solution (typically NaOH) was added to a glass vial. Approximately 100 mg of graphite flakes were added to the solution. The solution was then placed on a bath sonicator for 30 min. The sample was immediately centrifugated at a speed of 2,000 rpm for 60 min. After the centrifugation, 10.00 mL of the upper solution was removed using a micropipette and transferred into a clean vial. Great care was taken while removing the supernatant to avoid the large unexfoliated graphite flakes at the bottom of the vial. The resulting suspension was stored and used for characterization purposes.

2.3.4 Effect of the centrifugation velocity on the sample preparation

To study the effect of the centrifugation velocity, a sample was prepared as described in section 2.3.3. In this study, 100 mg of graphite flakes were added to 20.00 mL of a NaOH solution of pH = 11.0. After 30 min of ultrasonic exfoliation, the sample was immediately centrifuged with speeds ranging from 1,000 to 6,000 rpm for 60 min. After centrifugation, the resulting suspension was removed and stored for characterization.

2.3.5 Effect of exfoliation time on the sample preparation

To study the effect of the exfoliation time, a sample was prepared as described in section 2.3.3. In this experiment, 100 mg of graphite flakes were added to 20.00 mL of a NaOH solution of pH = 11.0. The exfoliation time ranged from 5 to 60 min. The sample was then centrifuged at a speed of 2,000 rpm and the resulting suspension was removed and stored for characterization.

2.3.6 Recycling of the unexfoliated graphite

To recycle the unexfoliated graphite, a sample was first prepared as described in section 2.3.3 with a NaOH solution of pH = 11.0. After the centrifugation step, 17.00 mL of the solution was transferred into a clean vial and stored for characterization. The vial containing the unexfoliated graphite was refilled with 17.00 mL of a fresh NaOH solution (pH = 11.0) to obtain the original volume of 20.00 mL. This procedure was repeated 24 times, each time using the graphite from the first cycle.

2.3.7 pH dependence in the exfoliation process and zeta potential measurements

To study the effect of the concentration of NaOH in the solution, the samples were prepared following the procedure described in section 2.3.3. In this experiment, 100 mg of graphite flakes were added to 20.00 mL of a solution with the following pH values: 7.0, 8.0, 8.5, 9.0, 9.5, 10.0, 10.5, 11.0, 11.5, and 12.0. The resulting suspension was extracted and used for UV-Vis and zeta potential measurements.

2.3.8 Effect of neutral salts or nature of the base present on the exfoliation process

To study the effect of the cation in solution during the exfoliation process, a sample was prepared following the procedure on section 2.3.3. On these samples, 100 mg of graphite flakes were added to 20.00 mL of a 1.0 mM solution of the desired base or neutral salt. The salts used to prepare the solutions were NaCl, LiCl, KCl, and the bases were KOH, K_2CO_3 and Na_2CO_3. The resulting suspension was extracted and characterized.

2.3.9 Effect of the graphite source on the exfoliation process

To assess the effect of the structure of graphite in the exfoliation process, seven sources of graphite were compared following the procedure on section 2.3.3. On this set of samples, the following types and amount of graphite were added to 20.00 mL of a solution of NaOH pH = 11: HOPG (500 mg), graphenium flakes (100 mg), graphite fine powder (100 mg), and 100 mg of graphite with three different grades (4827, TC307, 4052). After sonication and centrifugation, the resulting suspension was extracted and characterized.

2.3.10 Effect of annealed graphite on the exfoliation process

To analyze the presence of structural features on natural graphite, 100 mg of graphite powder was precisely weighted and placed on a copper foil rinsed with HCl and DI H_2O. The sample was annealed on a CVD furnace under an Ar flow of 250 SCCM at various temperatures, ranging from 50 °C to 600 °C for 1 h. After the sample was cooled to room temperature, the annealed graphite was exfoliated following the procedure on section 2.3.3. The resulting suspension was extracted and stored for characterization.

2.4 RESULTS AND DISCUSSION

2.4.1 Procedure optimization

In a typical experiment, natural graphite flakes were added to a solution of NaOH (pH = 11) and subjected to a bath sonication. The sonication produced a black suspension that was then centrifuged to remove the large graphite particles. In order to obtain the best exfoliation yield, the procedure to obtain exfoliated graphene was optimized.

2.4.1.1 Effect of centrifugation velocity on the sample preparation

Loyta *et al.* showed that centrifugation speed affects the yield of solution exfoliation of graphene.[67,60] To verify if the same effect was observed in our surfactant-free exfoliation method, a similar experiment was performed where the centrifugation speed was varied from 1,000 to 6,000 rpm. The general trend demonstrated that at speeds above 2,000 rpm the absorbance value at 500 nm stayed almost constant, shown in Figure 11. The centrifugation speed used on the rest of the experiments was 2,000 rpm, which resulted in a gray, transparent solution.

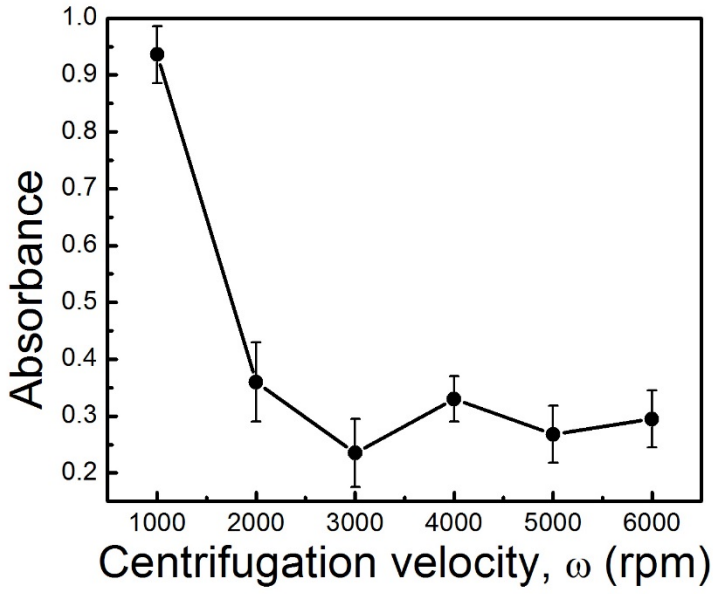

Figure 11. Absorbance value at 500 nm of the exfoliated graphene in a NaOH solution (pH = 11) as a function of the centrifugation velocity**.**

2.4.1.2 Effect of the exfoliation time on the sample preparation

Another procedure step that needed optimization was the sonication time. Among the many experiments realized by Li *et al.* in the exfoliation of graphite in organic solvents, one of them focused on how the exfoliation time affected the absorbance value of the solution with graphene.[57] Figure 12 shows the absorbance value at 500 nm of the dispersion as the sonication time ranged from 5 min to 60 min. After 30 min, the absorbance value reached to a maximum value and did not significantly change when the sample was exfoliated for 60 min, meaning that 30 mins of sonication is enough to obtain exfoliated graphene.

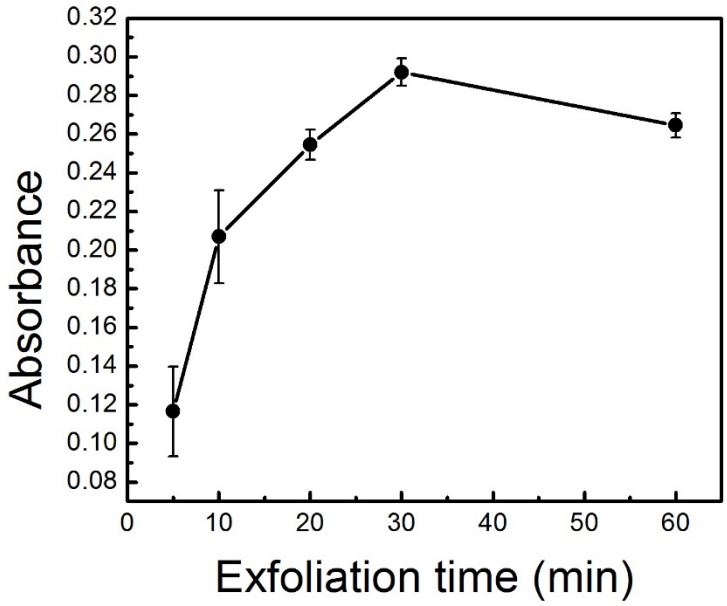

Figure 12. Absorbance value at 500 nm of the exfoliated graphene in a NaOH solution (pH = 11) as a function of the exfoliation time.

2.4.2 Characterization of exfoliated graphene

2.4.2.1 UV-Vis spectroscopy

After ultrasonic exfoliation and sonication, the resulting supernatant was transparent and greyish in color; a photograph of this solution is shown in Figure 13 inset. The UV-Vis absorption spectrum of the exfoliated graphene in solution is shown in Figure 13. The spectrum is featureless in the visible region, as expected for graphene. A prominent peak was found at around 268 nm corresponding to the π-π* transition of graphene and graphite.[208] For characterization and plotting purposes, the absorbance value at 500 nm was used because at this wavelength the spectrum is featureless.

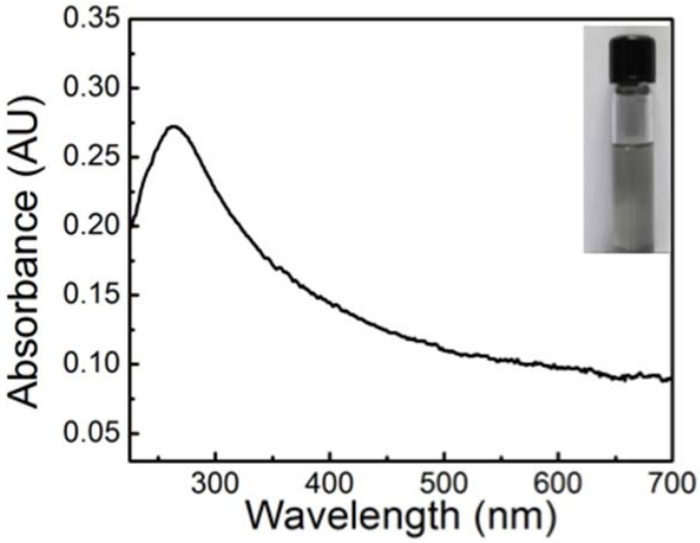

Figure 13. UV-Vis spectrum of the exfoliated graphene in a NaOH solution of pH = 11. Inset: Photographic image of the exfoliated graphene.

2.4.2.2 Raman spectroscopy

A micro-Raman spectrum was collected on a graphene dispersion deposited on a film. The Raman spectrum (Figure 14) shows three major peaks: the G peak at *ca.* 1580 cm^{-1}, the D peak at *ca.* 1350 cm^{-1} and the 2D peak at *ca.* 2750 cm^{-1}. The peak area ratio between the intensity of 2D and G peaks (I_{2D}/I_G ratio) is 0.50 and the 2D peak is broad, both of which suggest multi-layer graphene, likely more than 3 layers, in the sample. There is a noticeable D peak in the Raman spectrum with an I_D/I_G ratio of 0.52.

Because the size of the graphene flakes is on the order of 1 μm (*vide infra*), we believe that the edge and random stacking of the graphene flakes on the film contributed significantly to the observed D peak, although we cannot completely rule out the presence of in-plane defects. We note that because of the small size of the flake, D peak was generally observed in exfoliated graphene samples even if there was minimal in-plane defect in the sample.[58, 59, 67, 69] It is also

important to note that the D and G peaks of our graphene sample are well separated from each other and are distinctly different from those of graphene oxide, in which case the D and G peaks are broad and overlap.[209] This fact suggests that our graphene sample did not undergo severe in-plane disruption as in the case of graphene oxide.

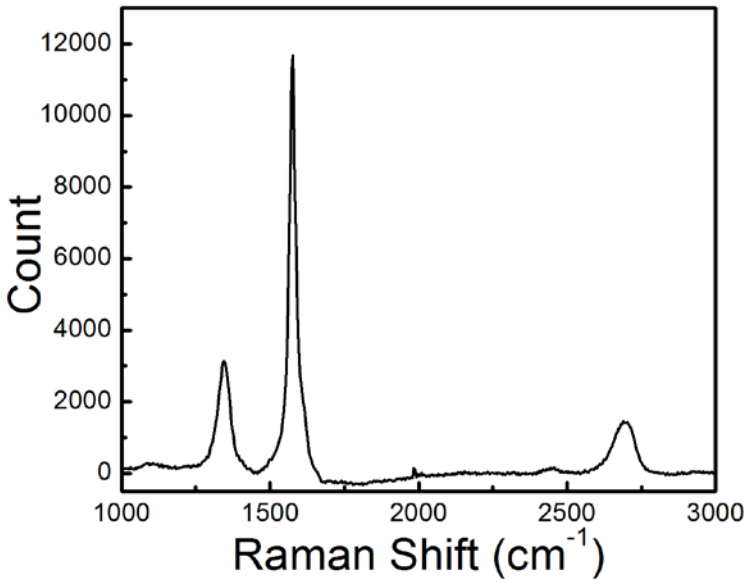

Figure 14. Micro-Raman spectrum of a film prepared with surfactant-free exfoliated graphene.

2.4.2.3 TEM imaging

To assess the morphology of the exfoliated graphene, a sample for TEM analysis was prepared by spotting the graphene suspension onto a holey carbon mesh grid. Depicted in Figure 15, the TEM images showed micrometer sized sheet-like structures, similar to other exfoliated graphene flakes reported in the literature.[58, 59, 67, 69] The size of the graphene flakes ranged from 200 nm to 2 μm. It is also observed that some flakes fold over or stack together to give a disordered multilayer structure. The number of the layers could not be determined using TEM, but we can assume the flakes have several layers because of the aggregation.

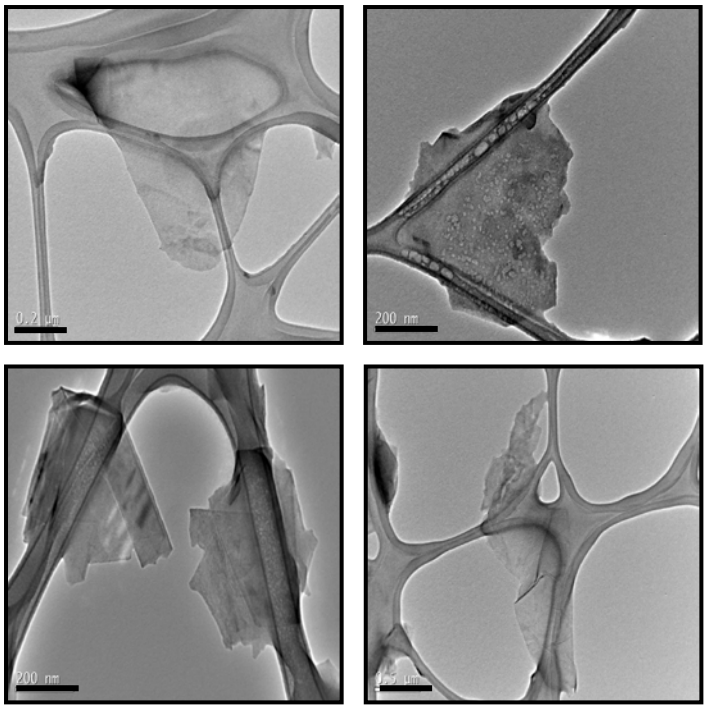

Figure 15. Selected TEM images of the exfoliated graphene flakes**.**

2.4.2.4 AFM imaging

For characterization using AFM, a graphene suspension was spin coated onto a highly ordered pyrolytic graphite (HOPG) substrate. The AFM image (Figure 16) show plate-like structures with a thickness in the range of several to several tens of nanometers, consistent with the presence of multi-layer graphene. The flakes varied from 50 to 300 nm long and ranged from 5 to 10 nm in height. We noticed that the density of graphene flakes is low on HOPG when compared to the TEM sample. The detailed reason is not known although it could suggest a weak interaction between HOPG and exfoliated graphene.

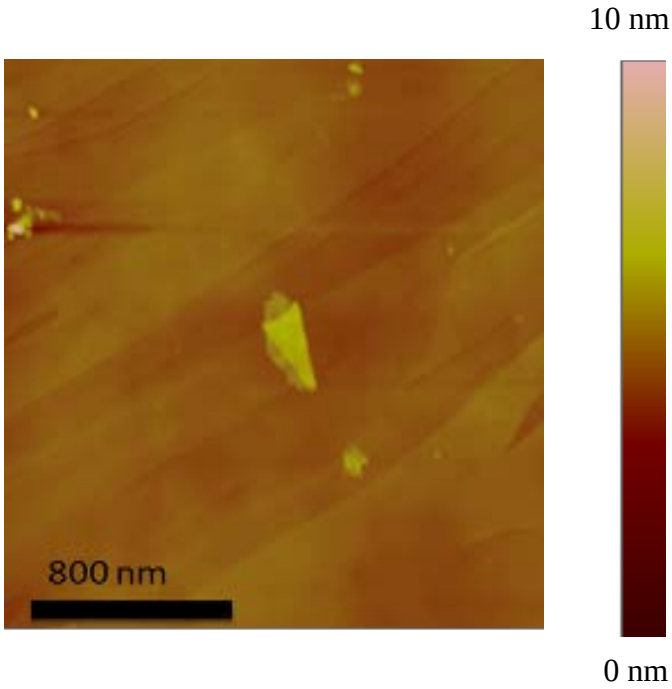

Figure 16. AFM image of exfoliated graphene flakes on a HOPG substrate. Scalebar denotes 800 nm.

2.4.3 Determination of graphene concentration in solution

We estimated the concentration of the graphene dispersion by creating a film that isolated the graphene flakes. This was done by carefully filtrating a small volume of the graphene in NaOH onto an alumina membrane. The film was then dried for 24 h and the concentration was determined by mass difference.

Another approach was via the Beer-Lambert equation using the published absorption coefficient of graphene by Coleman and coworkers.[58, 67] Depending on the reaction conditions (*e.g.*, pH, sonication time) used, the concentration of graphene ranges from 0.002 mg/mL to 0.20 mg mL^{-1}. These concentrations are comparable to those obtained by early studies of graphite exfoliation in organic solvents or using surfactant in water.[58, 67, 70] Recent studies showed that the

exfoliation yield can be significantly increased by edge functionalization,[210] adding intercalant,[211] or increasing sonication time.[59, 69]

2.4.4 Recycling of unexfoliated graphite

The yield of exfoliated graphene is low; however, the unexfoliated graphite powders can be recovered and recycled to improve the overall usage of the starting material. In a typical experiment, about 100 mg of graphite was exfoliated in 20.00 mL of a NaOH solution. The yield of graphene in the supernatant was up to 0.4 mg, or 0.4% of the starting material. Most of the graphite remained as unexfoliated large flakes. After removing the supernatant containing the exfoliated graphene, we added additional NaOH solution to the unsuspended graphite flakes and subjected the mixture to another round of ultrasound treatment to produce a new batch of suspended graphene. As shown in Figure 17, in one experiment, the same graphite starting materials was recycled and used in 24 successive exfoliation experiments. Although some fluctuations of the absorbance values are present, it is clear that the sediment can be recycled. Based on the optical density of the suspensions, we estimate that the overall yield from graphite to suspended graphene can be as high as 2.5%. Therefore, this approach has the potential for large scale, low cost production of graphene dispersions that could be useful in industrial applications.

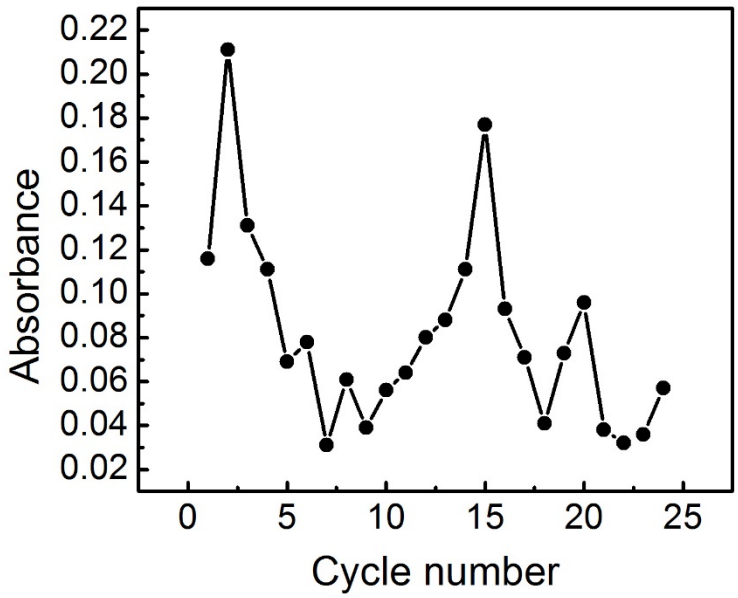

Figure 17. Absorbance value at 500 nm of the exfoliated graphene in NaOH as a function of the cycle number.

2.4.5 pH dependence on the exfoliation process

A thorough analysis of the dependence of the pH in the concentration of the exfoliated graphene was performed. Figure 18 shows a plot of the average absorbance values at 500 nm as a function of the pH of the solution where the graphene was exfoliated. At pH = 10 and 11 the highest absorbance values were observed, implying that a higher concentration of graphene is produced. This showed that the concentration of NaOH played a crucial role in the exfoliation process.

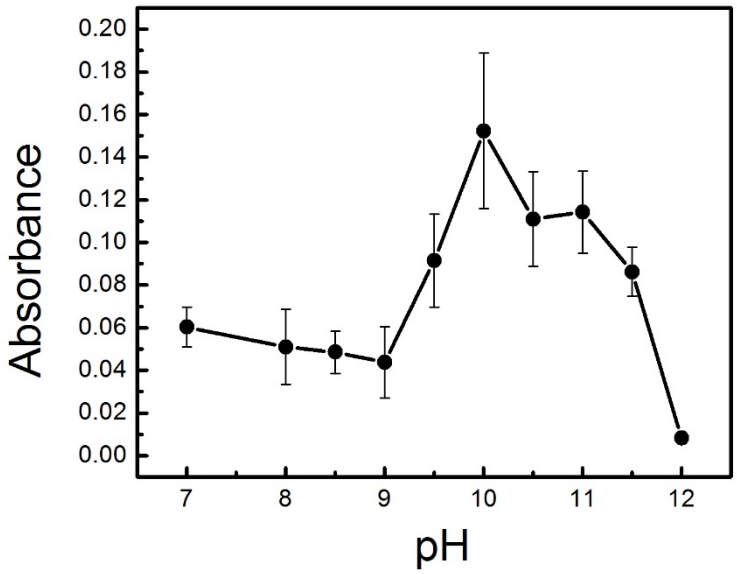

Figure 18. Absorbance values at 500 nm of the exfoliated graphene in NaOH as a function of the pH of the solution where the graphene was exfoliated.

2.4.6 Zeta potential analysis

The samples from the pH dependence study were also used to determine the zeta potential of the samples. For a graphene suspension prepared using a NaOH solution of pH = 11, its zeta potential was found to be -47 mV (Figure 19). Such a large value is usually associated with a stable colloidal suspension. When a solution of lower pH was used in the exfoliation, the zeta potential of graphene suspension decreased along with a decrease in the yield of the exfoliation. This was also observed with samples prepared in the acidic pH range. This result could be due to a change in the surface charge of graphene as the pH of the solution varies. As the pH increases, so does the concentration of hydroxide ions, causing a greater stability of the electric double layer. At pH = 11.5 and 12 the concentration of hydroxide ions is high, causing colloidal instability that results in the collapse of the electric double layer and subsequently, a decrease in

the zeta potential value. At lower pH values, there are not enough hydroxide ions to create a stable electric double layer. Therefore, the exfoliation is not possible and the zeta potential is high or near the isoelectric point.

Our preliminary hypothesis proposes that the graphene suspension is stabilized by electrostatic repulsion. Both of these observations suggest that the charge buildup on the exfoliated graphene flakes and their stability are linked to the OH^- ions.

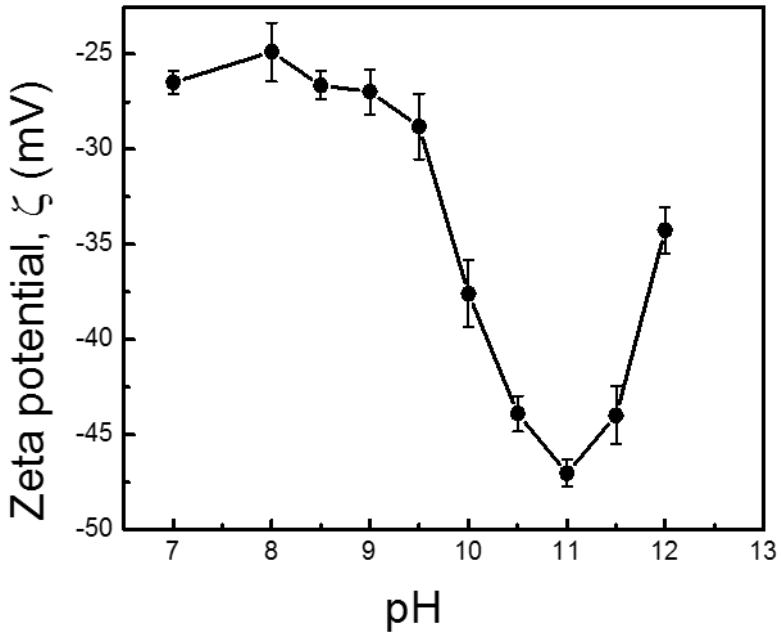

Figure 19. Zeta potential (mV) as a function of pH of the solution where the graphene was exfoliated.

2.4.7 Effect of neutral salts and nature of the base on the exfoliation process

To confirm that basic solutions are essential to obtain a high concentration of graphene sheets in a stable colloidal suspension, different bases (KOH, K_2CO_3, Na_2CO_3) and neutral salts (NaCl, LiCl, KCl) were used to exfoliate graphite. The chemical nature of the base does not affect the

outcome of the exfoliation. In addition to NaOH, we also obtained stable graphene dispersion with other bases. On the other hand, we found that using neutral salts of the same concentration did not produce stable graphene suspensions (Figure 20). This confirms that OH^- is essential to the successful exfoliation and stabilization of graphene in the absence of a surfactant. Overall, these observations are consistent with the previous reports that OH^- ions can spontaneously adsorb onto hydrophobic surfaces,[212-215] although we note that such claim is hotly debated in recent literatures.[216-219]

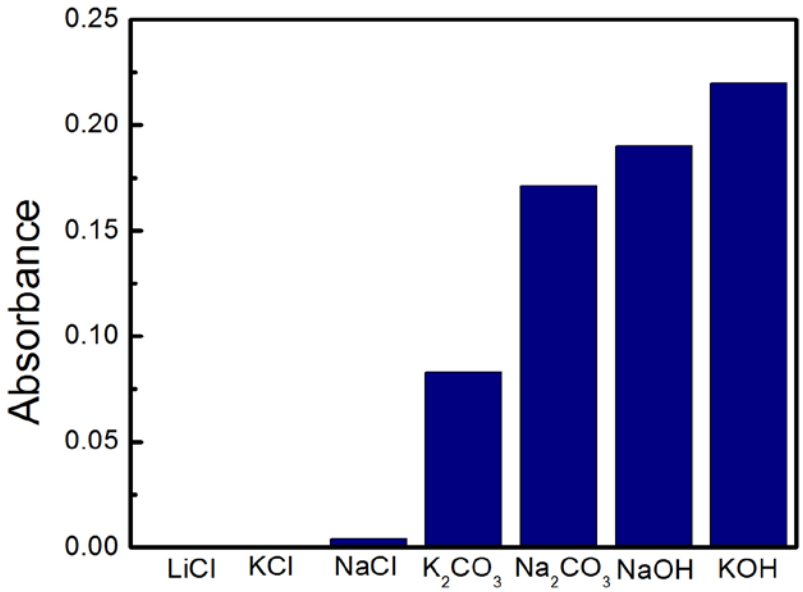

Figure 20. Histogram of the absorbance value at 500 nm of graphite exfoliated in different types of bases and neutral salts.

2.4.8 Effect of different sources of graphite on the exfoliation process

We tested 7 types of graphite with different grades, including natural graphite from various sources as well as HOPG. The result (Figure 21) shows that most natural graphite can be successfully exfoliated in NaOH solution without adding any surfactant. However, highly crystalline graphite (graphenium flakes and HOPG) showed almost zero exfoliation yield. This

result suggests that the colloidal stabilization of graphene could be connected to certain structure features of graphite that contribute to the outcome of the exfoliation.

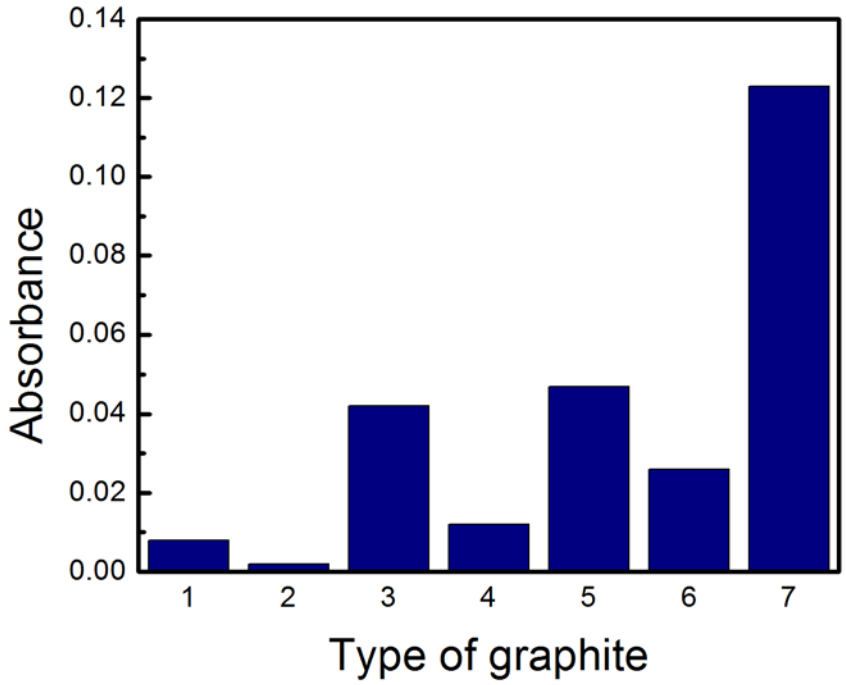

Figure 21. Histogram of the absorbance values at 500 nm of different sources of graphite. 1. HOPG, 2. Graphenium flakes (NGS Naturgraphit), 3. Graphite fine powder from Riedel-de Haën, 4. Asburg Graphite Mills (AGM) light powder [TC307], 5. AGM dense powder [4052], 6. AGM light powder [4827], 7. Sigma-Aldrich graphite flakes.

2.4.9 Effect of the annealed graphite on the exfoliation process

To confirm the hypothesis that certain structural features are present on the graphite flakes, we annealed a sample of natural graphite under an Ar atmosphere for 1 hr at temperatures ranging from 50 ˚C to 600 ˚C. We found no effect on the exfoliation yield when the graphite powder was annealed at 300 °C or lower. However, annealing the graphite sample at 400 °C or higher significantly reduced the exfoliation yield to almost zero (Figure 22). This result suggests that

certain thermally labile functional groups may exist in natural graphite (*e.g.*, -OH and –COOH) and contribute to the stabilization of graphene in water.[220] Significantly, the annealed graphite showed a mass loss of only 0.06 % after annealing in Ar at 600 ˚C for 1h, indicating that the density of such functional group must be very low.

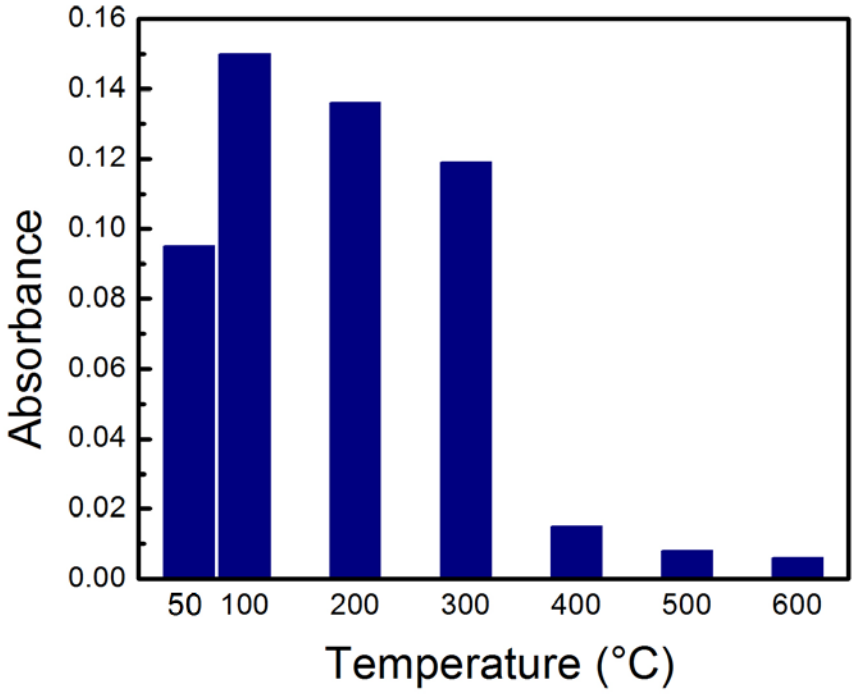

Figure 22. Histogram of the absorbance value at 500 nm of the exfoliated graphene after the graphite was annealed at different temperatures.

2.5 CONCLUSION

In summary, we have developed a surfactant-free exfoliation of natural graphite into multilayer graphene in a weakly basic aqueous solution. The graphene flakes are stabilized by electrostatic repulsion and are stable at room temperature for up to several months. The exfoliation yield and

zeta potential of the graphene dispersion depends on the solution pH, with pH = 11 giving the optimal results. Control experiments suggest that interfacial accumulation of OH^- ions and naturally-occurring functional groups in graphite may contribute to the observed colloidal stability of graphene. This unexpected result opens up new possibilities in preparing graphene dispersions with low cost and minimal environmental impact.

3.0 DEPOSITION OF DNA ORIGAMI NANOSTRUCTURES ON HIGHLY ORIENTED PYLOLYTIC GRAPHITE

3.1 CHAPTER PREFACE

Materials contained in this chapter were published as a research article in *Langmuir*; figures used in this chapter have been reprinted with permission from: *Langmuir* **2017,** *33 (16)*, 3991 – 3997.

List of Authors: Karen B. Ricardo, Anqin Xu, Muhammad Salim, Fen Zhou and Haitao Liu.

Author Contributions: K.B.R, A.X. and H.L. designed and directed the experiments. K.B.R., A.X., M.S. and F.Z. conducted the experiments. All authors discussed the results. K.B.R., A.X. and H.L. wrote the manuscript with input from all authors.

3.2 INTRODUCTION

DNA nanostructures have been a useful template for patterning at the nanometer length scale.[138] Programmable structures can be created using synthetic, short strand DNA with or without a single strand viral scaffold DNA to form 2D and 3D shapes,[99, 114, 115, 128, 129] making them useful for a wide variety of applications that include, but are not limited to, metallization,[179] growth of oxides,[141] and nanomaterial positioning.[221,222]

The sp^2 carbon materials have been widely studied because of their excellent mechanical, thermal and electrical properties.[223,12] Among the many different types of carbon materials (*e.g.*, graphite, semiconducting and metallic carbon nanotubes, and single and multilayer graphene), HOPG is often used as the model to understand the basic properties of extended sp^2 carbons in wetting,[224] adsorption,[225] tribology,[226] biosensing,[227] and surface chemistry.[228] Therefore, a fundamental understanding of the interaction between DNA nanostructure and HOPG will pave the way to integrating DNA nanostructure with a broad range of sp^2 carbon materials.

The interaction between graphitic surfaces with DNA has been studied for many years.[229-230] Husale, *et al*. reported a strong binding interaction between ss-DNA and exfoliated graphene and demonstrated preferential orientation of the ss-DNA towards the graphene lattice.[171] They also attempted to deposit DNA origami on graphene but the origami structures were not stable because they did not add Mg^{2+} in the buffer. Regarding DNA-HOPG interactions, all deposition procedures in literature involved surface modification,[21] applying a voltage,[158, 159] or the modification of the DNA origami.[231] Recently, DNA nanostructures have been deposited on graphene; however, most of these efforts involve a modification of the

substrate to enhance DNA-carbon interaction, such as doping[24,25] and assisted immobilization.[179] It was recently reported that cross-shaped DNA origami structure is deformed when deposited onto graphene.[176] In contrast, on 1-pyrenemethylamine modified graphene, DNA nanostructures were deposited without such deformation and were successfully used for subsequent metallization.[179] A related study also investigated the deposition of a cross shaped DNA nanostructure on pristine and 1-pyrenemethylamine-modified MoS_2 surfaces.[232] Similar to the case of graphene, the origami was found to deform upon contact with the pristine MoS_2 surface but the shape can be preserved by adding a layer of 1-pyrenemethylamine to the MoS_2 substrate. These preliminary reports point to the need to better understand and control the interaction between graphitic surface and DNA nanostructures.

Recently, we and others showed that exfoliated HOPG presented a water contact angle of 64.4°,[35] much smaller than the previously accepted value of 86°.[30] It was further shown that the commonly observed hydrophobicity of graphite is due to adventurous airborne hydrocarbon contamination.[36] This finding points to a previously unknown factor that could impact graphitic carbon-DNA interaction and opens new opportunities to control the deposition of DNA nanostructures onto graphitic substrates.

Herein we report a detailed study of the deposition of triangular DNA origami nanostructures on exfoliated HOPG without any surface or DNA nanostructure modification. AFM was used to analyze the DNA origami. The results showed that the deposition is accompanied by a structural reconfiguration of the DNA origami to maximize Van der Waals interactions between the DNA bases and the substrate. Surface contamination of HOPG by airborne hydrocarbons does not significantly impact the outcome of the deposition. Despite the structural change, the morphology of the DNA nanostructure remained unchanged on the HOPG

surface for at least a week, comparable to the stability of DNA nanostructures deposited on other substrates, such as Si/SiO_2.[151] This result provides new insight into the interaction between graphitic carbon and DNA nanostructures and could aid the development of biosensors and electrochemistry applications.

3.3 EXPERIMENTAL SECTION

3.3.1 Materials

DNA strands were synthesized by Integrated DNA Technology, Inc. or purchased from Bayou Biolabs, LCC. The irrelevant DNA single strand was purchased from Integrated DNA Technology, Inc. (http://www.idtdna.com). Acetic acid, EDTA, magnesium acetate and tris(hydroxymethyl)aminomethane were purchased from Sigma Aldrich. The HOPG with a dimension of 20 x 20 x 1 mm (SPI-2 grade, lot #1170412) was purchased from SPI Supplies. Si wafers containing 300 nm of SiO_2 (Si/SiO_2) were purchased from University Wafers. The bench top microcentrifuge was purchased from Fisher Scientific, USA. The 30 kDa MW centrifuge filters (Nanosep Centrifugal Devices with Omega Membrane) were purchased from Pall Corporation, Port Washington, NY. The spectrophotometer used to determine the concentration of DNA triangles (NanoDrop 2000c) was purchased from Thermo Scientific. The Scotch tape used to exfoliate HOPG was obtained from 3M. The plastic Petri Dish used for the deposition of DNA origami were purchased from VWR International LLC. The Kimwipes used to maintain a humid environment during the deposition process were obtained from Kimberly Clark.

3.3.2 Characterization methods

AFM images were taken with a Digital Instruments Nanoscope IIIA from Veeco Systems in tapping mode in air using silicon tips with a resonance frequency of approximately 320 kHz. Figures 34 and 35, were collected using an Asylum MFP-3D Atomic Force Microscope by tapping mode in air with HQ:NSC15/Al BS AFM probes (325 kHz, 40 N/m) purchased from μmasch (Nano and More, USA). All images collected had a scan rate of 1.0 Hz and 512 data points per line with scan size identified by scale bars. XPS measurements for the samples were conducted with a Thermo Scientific™ Escalab 250Xi. The X-Ray source was monochromatic and used an Al anode with a spot size of 0.2 mm for the samples in Figure 27 and 0.4 mm for the CVD experiments (Figure 37), with a takeoff angle of 45˚. A minimal of 3 survey scans (10 scans for CVD experiments) were employed for good signal to noise ratio. Higher resolution scans were performed with a minimum of 64 scans. Measurements were acquired, peaks deconvoluted, and analyzed using the Thermo Scientific™ Avantage Data System or the XPSPEAK 4.1 software. Peak fitting allowed for Lorentzian-Gaussian ratio control as well as difference spectra optimization, with the Smart method being implemented to calculate the background spectrum.

3.3.3 Synthesis of DNA origami nanostructures

Triangular-shaped DNA nanostructures were synthesized using a previously published method[122] by mixing 15.0 μL of DNA staples (300 nM for each staple), 8.60 μL of M13mp18 DNA (454 nM), 77 μL of DI water and 181.0 μL of a TAE/Mg buffer. The stock TAE/Mg buffer solution contains the following reagents with its respective concentrations: 150.0 mM of $Mg(OAc)_2$, 2.0

mM of acetic acid, 2 mM of EDTA, and 40 mM of tris(hydroxymethyl)aminomethane. The stock solution was then diluted for all the experiments and the concentrations were 12.5 mM of $Mg(OAc)_2$, 0.17 mM of acetic acid, 0.17 mM of EDTA and 3.33 mM of tris after dilution. The diluted TAE/Mg solution with the DNA was then heated to 95 ˚C and slowly cooled down to 25 ˚C at a rate of 1 ˚C min^{-1}. After the cooling process was completed, the sample (*ca.* 280 μL) was divided equally and transferred into two separate 30 kDa MW centrifugal devices (Nanosep Centrifugal Devices with Omega™ Membrane, Pall Corporation, Port Washington, NY). Additional *ca.* 400 μL of diluted buffer solution was added into each centrifugal device and the mixtures were centrifuged at a speed of 6000 rpm using a single speed benchtop microcentrifuge to remove the excess DNA staple strands. The DNA origami solution was centrifuged until 1/3 to 1/4 of the original volume was left to ensure that the solution was not completely centrifuged to dryness. The process of adding buffer and centrifuging was repeated five times. The final DNA triangle solution was stored inside plastic vials at 4 ˚C.

The triangular DNA origami used in this study is formed by three trapezoidal domains and each of the domains is formed by nine cross-linked double helixes with a length of approximately 122.4 nm (Figure 23A).[122] The width at the origami edge was estimated to range from 26 nm to 30 nm, depending on the size of the inter-helix gap. The structure also contains a loop composed of 97 base pairs. Using the NUPACK software, it was determined that the loop is mostly linear (Figure 23B).[233]

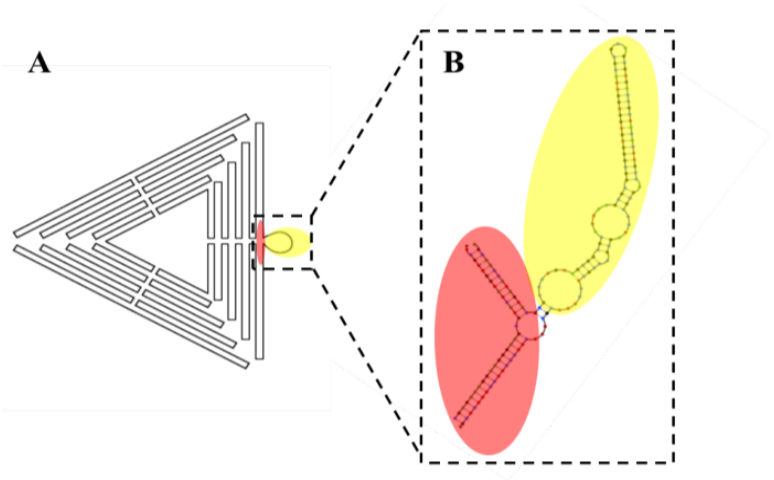

Figure 23. (A) A sketch of triangular DNA origami with a loop on one side. (B) Secondary structure analysis of this 97-base loop of the DNA nanostructure. The loop was marked in yellow; the two adjacent 16 bases and the complementary staple DNA were marked in red. Reprinted with permission from reference 234, Copyright © 2015, American Chemical Society.

3.3.4 Cleaning of Si/SiO_2 wafer

A clean Si wafer with 300 nm of oxide was used as a support for the HOPG samples. In order to preserve a clean sample, the wafer was immersed in a piranha solution composed of H_2SO_4:H_2O_2 (70:30 v/v) and left undisturbed for 30 minutes. *Warning: piranha solution presents an explosion danger and should be handled with extreme care; it is a strong oxidant and reacts violently with organic materials. All work should be performed in a fume hood. Wear proper protective equipment*. The sample was then removed and copiously rinsed with DI water (> 10 mL) and blow-dried with N_2 gas.

3.3.5 Exfoliation of HOPG

HOPG was cleaved following the Scotch tape method[43] using double-sided tape. Once the tape was attached to the HOPG, it was gently massaged to remove any air bubbles present. The tape was then slowly removed and a continuous layer of HOPG was obtained. This tape was then attached to a clean Si/SiO_2 substrate for support. The HOPG layer on the tape was exposed to air and used as a substrate for the following experiments.

3.3.6 Deposition of DNA origami triangles on HOPG and Si/SiO_2

The synthesized DNA origami solution was diluted with the TAE/Mg buffer and 20 μL was deposited using a micropipette to a HOPG substrate prepared using the procedure described in section 3.3.5. The purpose of the dilution was to ensure that no more than a monolayer of DNA origamis were deposited on the HOPG surface. The HOPG was then left undisturbed for 40 min in a plastic Petri dish. To keep a humid environment and avoid evaporation, a wet Kimwipe was placed between the cover and the bottom of the Petri dish. The HOPG substrate was then slowly dried using a rubber tube to flow N_2 gas and them completely immersed in a 90 % -10 % (v/v) ethanol-water solution for 10 s to remove any residues present from the buffer solution. The rinsing solution was used once for every sample prepared. Finally, the sample was air dried using N_2 gas. To ensure complete removal of the salt residue, the immersion and drying steps were repeated 3 times.

The same process was used for depositing DNA nanostructures onto the Si/SiO_2 substrate.

3.3.7 Effect of non-hybridizing ss-DNA on the deposition of DNA origami

DNA triangles were prepared using 1.2:1 staple-scaffold ratio using the method previously described in section 3.3.3. The concentration of the DNA and the non-hybridizing DNA strand were determined by a UV-Vis spectrophotometer. DNA triangles were thoroughly mixed with an irrelevant ss-DNA DNA single strand in 1 × TAE-Mg buffer. The sequence of the strand was determined to be

5'-

ACATTCCTAAGTCTGAAACATTACAGCTTGCTACACGAGAAGAGCCGCCATAGTA -

3'

and was used without further purification. This DNA is considered irrelevant because it does not have a complimentary sequence longer than 8 nucleotides with M13mp18 single stranded phage DNA or any of the staple strands. The final concentrations of DNA triangle and irrelevant DNA single strand in each sample are listed in Table 3.

3.4 RESULTS AND DISCUSSION

3.4.1 General procedure for the deposition of DNA origami on HOPG

A schematic illustration of the deposition process of the DNA triangle origami onto HOPG is shown in Figure 24. A previous report attempted to deposit DNA origami triangles on HOPG for imaging purposes but observed no deposition.[234] Contrary to that report, we found that the deposition of DNA nanostructures was achieved after depositing approximately 20 µL of the

DNA origami solution onto HOPG. In this experiment, HOPG was exfoliated and immediately used (within < 30 s of exfoliation) for the DNA origami deposition.

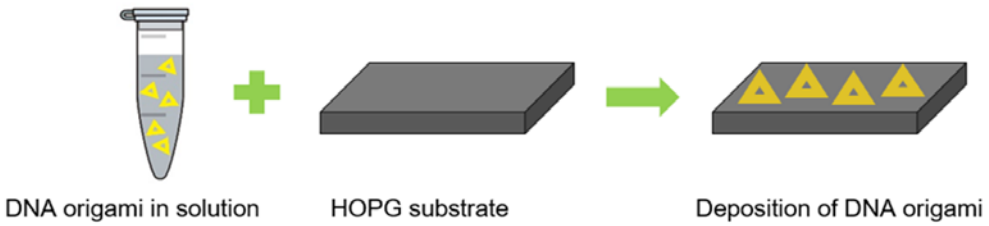

Figure 24. Schematic of the deposition process.

3.4.2 Procedure optimization

Great care was taken whenever rinsing the HOPG substrate since the interaction of the DNA origami with the HOPG substrate is different from other substrates (*e.g.*, Si/SiO_2). It was important to determine the best rinsing process because AFM is a very sensitive characterization method and a clean surface is essential to obtain high quality images. The solvents tested ranged from polar to non-polar (Figure 25). It was discovered that having a 90% ethanol solution in water was optimal. This solution removes the salt residues from the deposition without losing the origami structures.

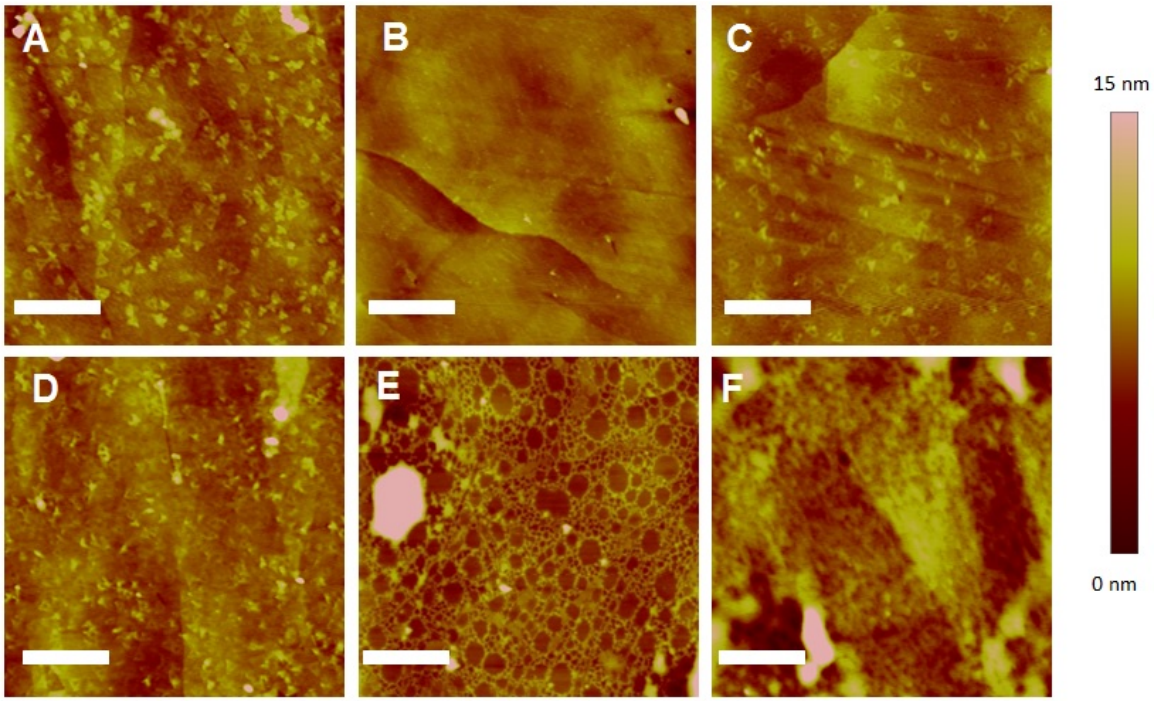

Figure 25. Representative AFM images of the DNA nanostructures deposited onto HOPG after being rinsed with different solvents: (A) No rinse. (B) Water. (C) 90 % ethanol solution in water. (D) Ethanol. (E) Acetone. (F) Hexane. The scale bars denote 1 μm.

3.4.3 AFM imaging

AFM imaging was performed to examine the morphology of the DNA triangle. We found that the overall shape of the origami was preserved, but the lateral segments of the triangle were significantly deformed (Figure 26A) when compared to the ones deposited on a Si/SiO_2 wafer (Figure 26B). We analyzed the cross section of 10 DNA triangles (Figure 26C) to extract the FWHM of the width of the lateral triangle sides. The DNA nanostructures deposited on HOPG are *ca.* 1.7 times wider in size than the ones deposited on Si/SiO_2. Note, in this analysis, the effects of AFM tip convolution and tip-sample interaction are neglected.[235] It was also found that

ca. (74.7 ± 5.0) % of the DNA triangles conserved their shape (*i.e.*, structures having a hole surrounded by three deformed edges).

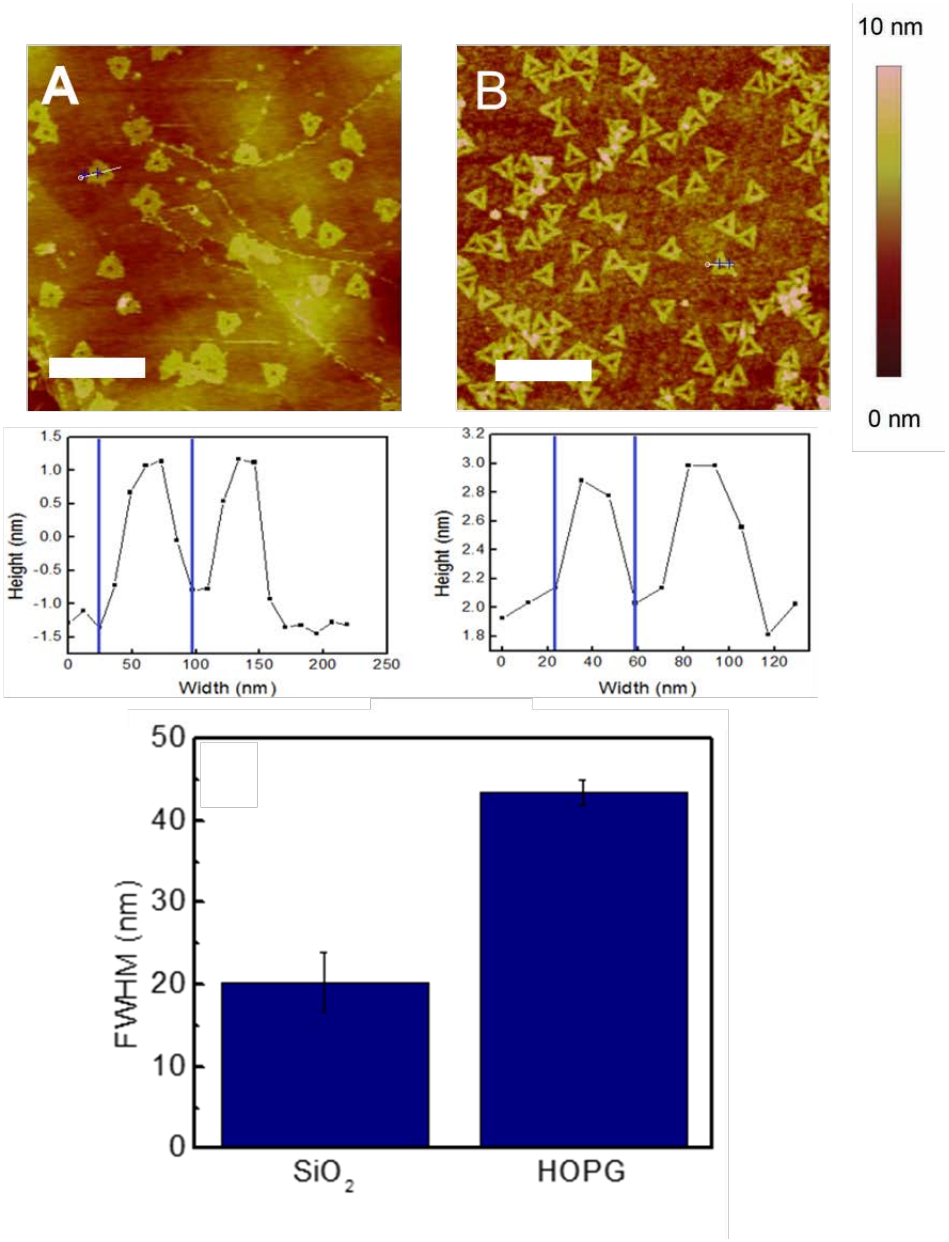

Figure 26. Representative AFM images of the DNA triangles deposited on (A) HOPG and (B) Si/SiO_2. The scale bars denote 500 nm. The cross sections below show the height profile of selected DNA triangles in the image. (C) Histogram of the FWHM of DNA triangle edge of the two samples.

3.4.4 XPS analysis

XPS elemental analysis showed the presence of Mg in the sample, which was present in the buffer solution (Figure 27A), and P from the DNA backbone (Figure 27B). Other elements such as nitrogen and oxygen were also found, but they were not quantified due to likely contribution from airborne contamination (Figures 27C and 27D).

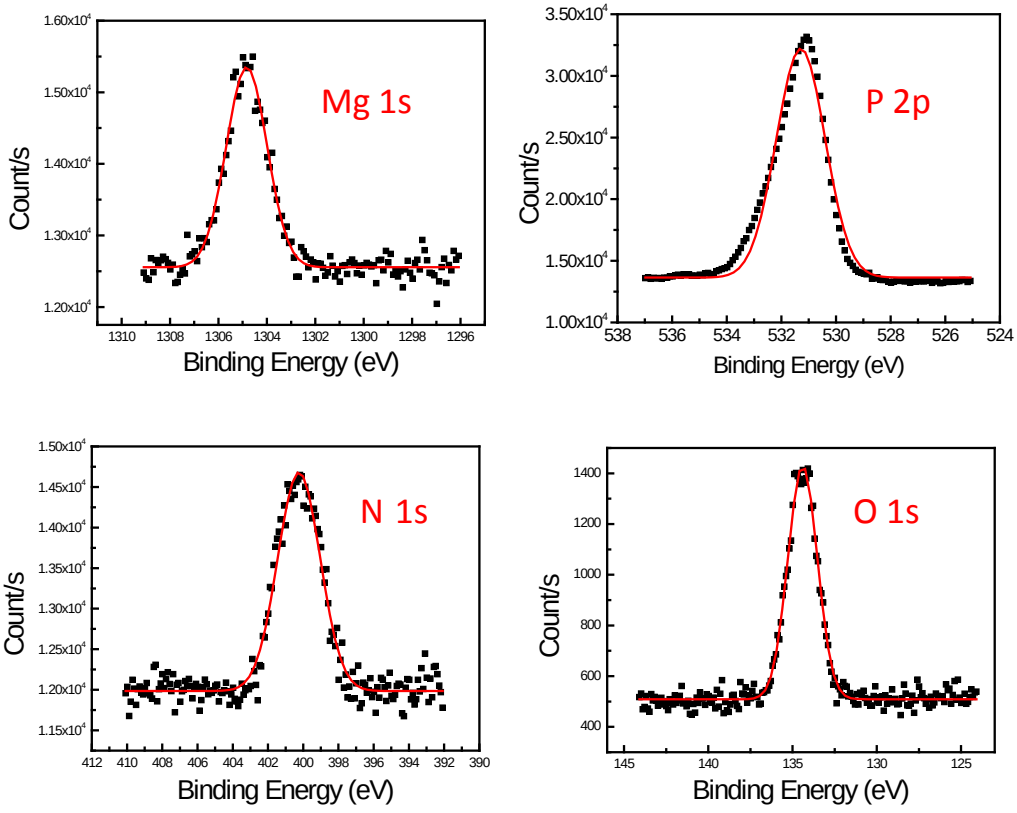

Figure 27. XPS spectra of peaks of the DNA origami samples deposited on HOPG. (A) Mg 1s. (B) P 2p. (C) N 1s. (D) O 1s (D).

3.4.5 Effect of temperature on the deposition process

To understand the observed shape deformation of DNA nanostructures, we note that that ss-DNA interacts strongly with graphitic materials such as graphene[171] and carbon nanotubes.[236] Computational simulations of DNA nanostructures have also demonstrated that under aqueous conditions, the DNA origami goes through spontaneous dehybridization with a length of 3 - 6 base pairs.[237] One explanation for this observation is that the interaction between the DNA origami and the HOPG surface involves partial structural rearrangement and partial dehybridization of the DNA duplex, exposing the DNA bases to create π-π stacking interaction with HOPG.[158, 161] This conformation change causes the expansion of the lateral size of the DNA nanostructure.

To test if our hypothesis is correct, we studied the effect of temperature on the deposition process. We reasoned that the DNA dehybridization will be suppressed at lower temperature and thus the morphology of DNA nanostructure will be better preserved. Indeed, when the deposition was conducted in an ice bath, the FWHM of the lateral size of the DNA nanostructure deposited on HOPG was smaller (33.5 ± 5.6 nm) than the value for samples deposited on HOPG samples at room temperature (Figure 28). Surprisingly, the density of the DNA nanostructure also increased, suggesting that entropy may also play a significant role in the deposition process.

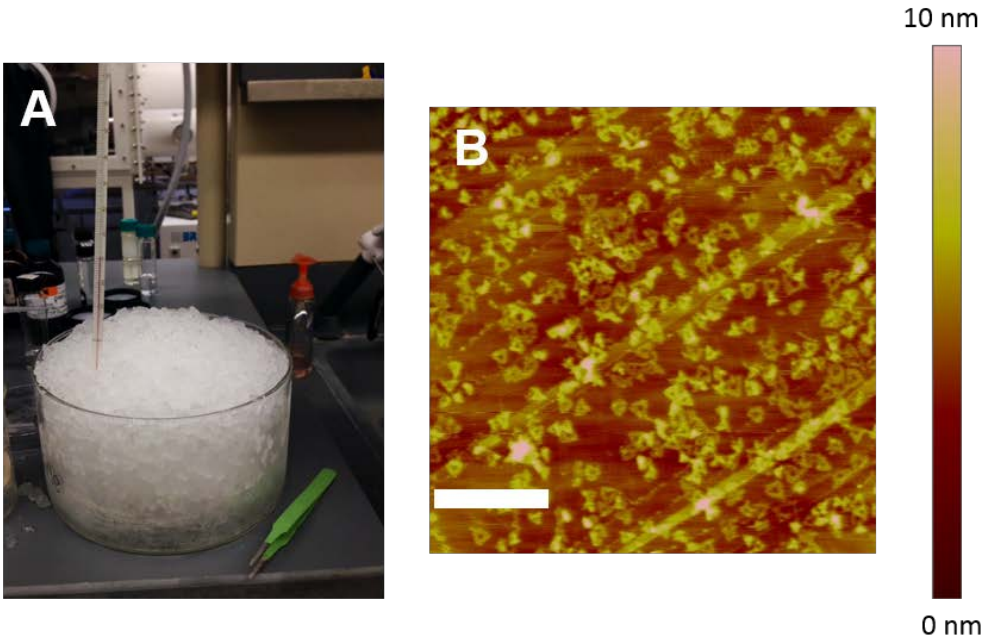

Figure 28. Effect of low temperature on the deposition process. (A) Photographic image of the experimental setup. (B) Representative AFM image of the deposited origami. The scale bar denotes 750 nm.

3.4.6 Effect of the wettability of HOPG

In the above experiments, the HOPG substrate was used immediately (< 30 s) after exfoliation. As discussed in the introduction, the wettability of graphitic surfaces can be significantly impacted by airborne hydrocarbons contamination. Given this recent development, it was of interest to analyze if the deposition of DNA nanostructure can be achieved when the HOPG surface was exposed to air for longer periods of time. The longer the HOPG is exposed to air, the more hydrocarbon contamination present in the atmosphere can adsorb onto HOPG, making it more hydrophobic.[35]

Different HOPG samples were left exposed to air ranging from 5 seconds up to 4 hours (Figure 29A-F). We previously showed that exposing a freshly cleaved HOPG to air for > 1 hour

will render its surface hydrophobic (water contact angle > 80°).[35, 36, 38] The result showed that the exposure time of the HOPG does not significantly affect the deposition outcome. After 4 hours of exposure the deposition of DNA nanostructure was still observed (Figure 29F). FWHM analysis of the cross-section of 10 representative triangles on each sample shows that the lateral side dimension is slightly smaller in the case of air-aged HOPG but the difference is close to the standard deviation (Figure 29G). Since the airborne contamination does not significantly affect the deposition process, we conclude that the interaction between the DNA origami nanostructure and the HOPG is not dictated by the wettability of the substrate.

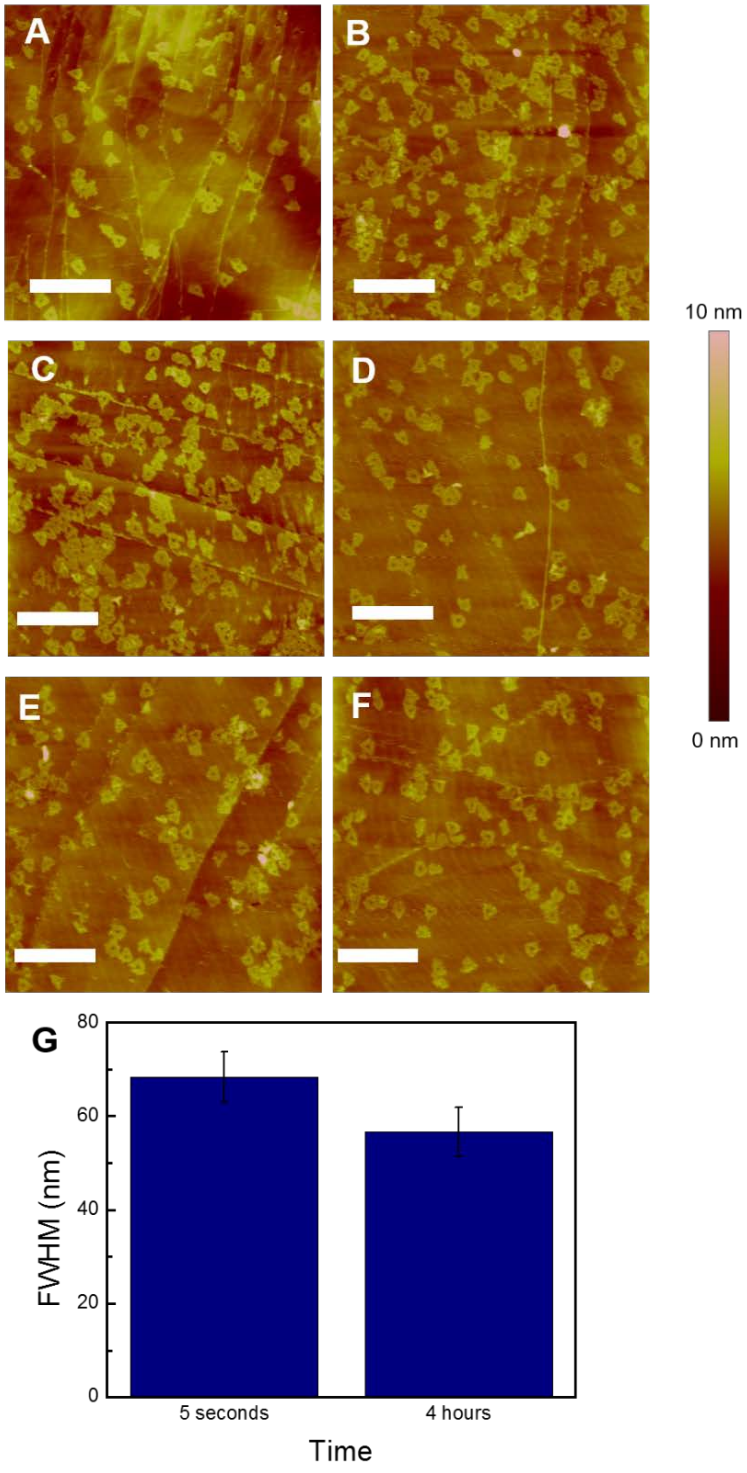

Figure 29. Representative AFM images of the DNA nanostructures deposited onto HOPG that has been exposed to air for different times after cleavage: (A) 5 sec (fresh). (B) 30 min. (C) 1 hour. (D) 2 hours. (E) 3 hours. (F) 4 hours. The scale bars denote 750 nm. (F) Histogram of the FWHM of the cross-section analysis of 10 DNA triangles from figure A and F.

3.4.7 Stability of deposited DNA origami nanostructures in air over time

Having established the successful deposition of DNA triangle nanostructures on HOPG, we moved our attention to the stability of deposited DNA origami in air. Same-location AFM images were taken after the sample was exposed to air for up to a week (Figure 30). It was observed that the width of the side of the triangles remained unchanged, indicating the absence of diffusion of the DNA backbone on HOPG in the dry state. This result also concurs with the stability of the DNA triangles deposited in a Si/SiO_2 wafer (Figure 31). It was observed that the dimensions of the triangles also remained unchanged.

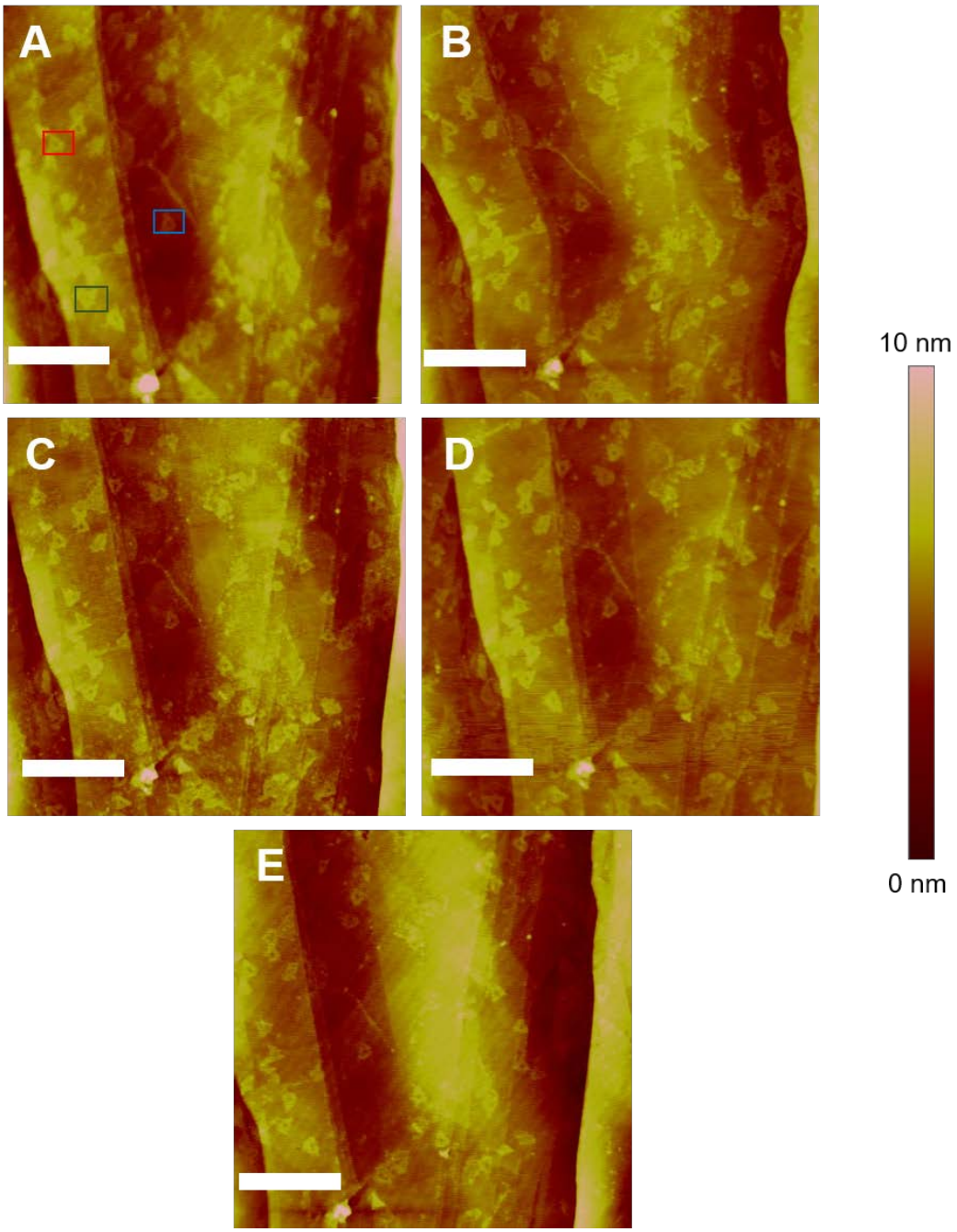

Figure 30. Same location AFM images of the DNA nanostructures at different times after the deposition: (A) Fresh (~2 hours). (B) 2 days. (C) 4 days. (D) 5 days. (E) 7 days. The scale bars denote 750 nm.

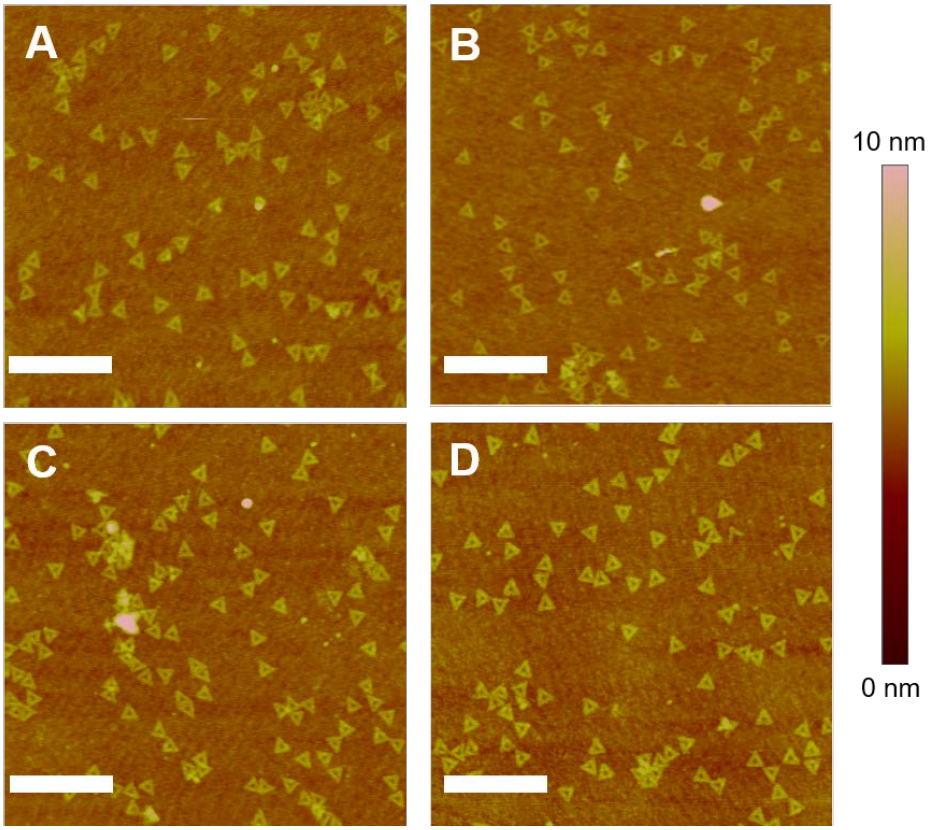

Figure 31. Same area AFM images of the DNA nanostructures deposited on Si/SiO_2 substrate at different times after the deposition: (A) Fresh (~2 hours). (B) 2 days. (C) 5 days. (D) 7 days. The scale bars denote 750 nm.

3.4.8 Effect of the Mg^{2+} concentration in the aqueous buffer on the deposition of DNA origami

Si/SiO_2 is one of the most often used substrates for studying DNA nanostructures. The interaction between the DNA origami and the HOPG is promoted by strong Van der Waals forces while its interaction with a Si/SiO_2 substrate has an electrostatic nature, using Mg^{2+} as an intermediate.[176] It was of interest to analyze the qualitative magnitude of the interaction between DNA and the two substrates. To this end, we exfoliated the HOPG substrate and exposed it to air for different periods of time (5 seconds to 1 hour) before used for the deposition of DNA

nanostructure. AFM images of the deposited DNA nanostructure were taken at 4 locations, 20 μm apart from each other. The results show that the density of the DNA triangle did not change among these samples (Figure 32 and Table 1). However, the ratio between the density of triangles found on HOPG and Si/SiO_2 is *ca.* 1:2, demonstrating that the interactions between DNA and the two substrates are significantly different (Figure 32E). A similar experiment was performed by adjusting the ionic strength of the buffer by increasing the Mg^{2+} solution concentration from 12.5 mM to 125.0 mM. In this case, although the amount of deposited DNA nanostructures decreased, the ratio of density of triangles between the HOPG and the Si/SiO_2 substrate remained *ca.* 1:2, indicating that the ionic interaction between DNA and SiO_2 is again stronger under this condition (Figure 33).

Table 1. Number of DNA origami nanostructures present at each 3 μm × 3 μm AFM image scanned for 4 samples.

	Location 1	Location 2	Location 3	Location 4	Average
Fresh HOPG	47	36	59	38	45 ± 5
30 min HOPG	51	66	54	63	59 ± 4
60 min HOPG	49	46	41	--	45 ± 2
Si/SiO_2	102	115	98	103	105 ± 4

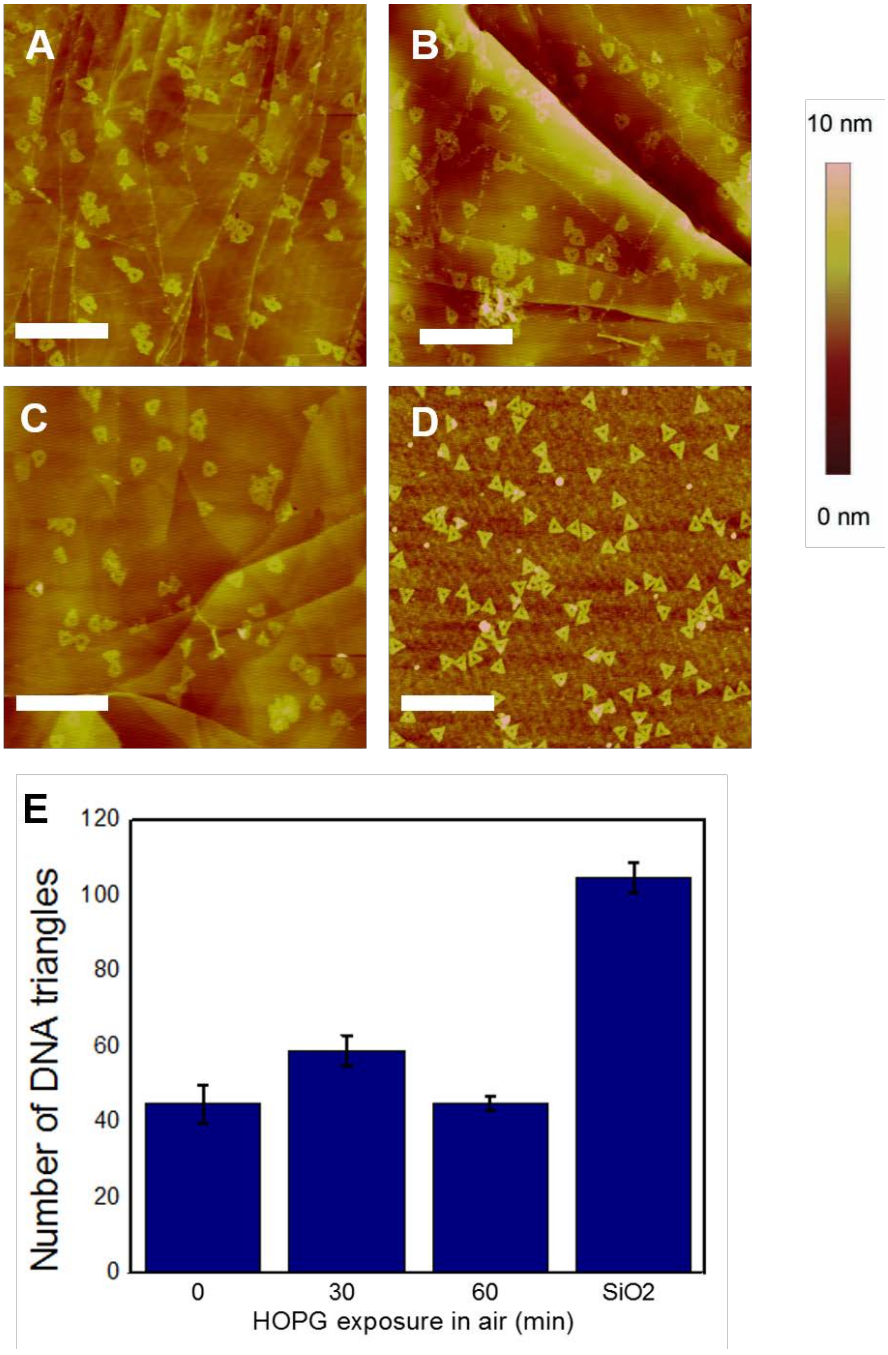

Figure 32. Representative AFM images of the DNA nanostructures as a function of time of HOPG exposure to air with a Mg^{2+} concentration of 12.5 mM. Each images represent one of the four images taken per sample: (A) Fresh (< 5 s). (B) 30 min. (C) 60 min. (D) Si/SiO_2. (E) Histogram representing the number of DNA triangles per AFM image. The scale bars denote 750 nm.

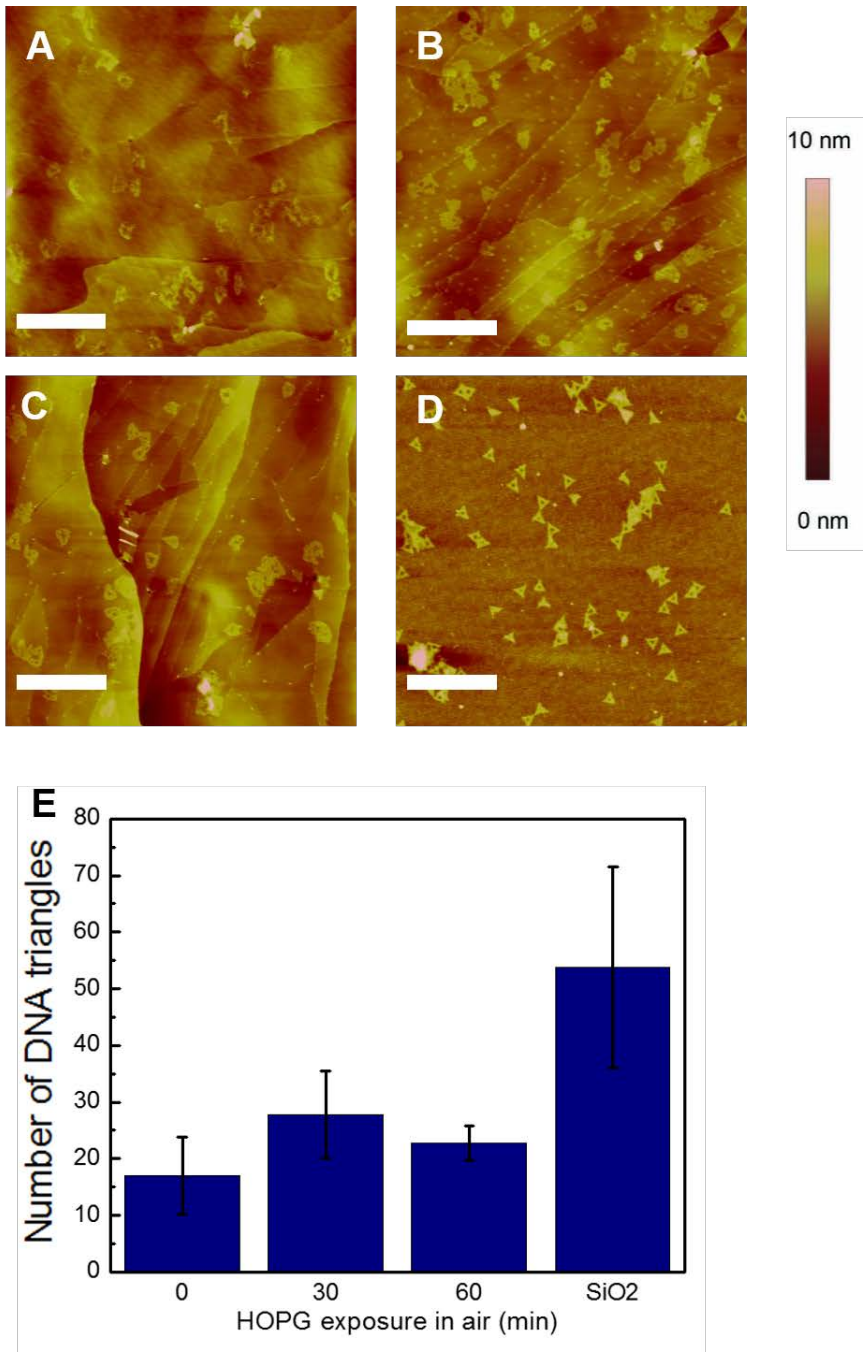

Figure 33. Representative AFM images of the of the DNA nanostructures as a function of time of HOPG exposure to air with a Mg^{2+} concentration of 125.0 mM. The images represent one of the four images taken per sample: (A) Fresh (< 5 s). (B) 30 min. (C) 60 min. (D) Si/SiO_2. (E) Histogram representing the number of DNA triangles per AFM image. The scale bars denote 750 nm.

3.4.9 Role of ss-DNA

Single stranded DNA is known to strongly adsorb onto HOPG.[25] A large excess of ss-DNA was used in preparing DNA origami. Although most of these ss-DNA will be removed by the purification process, it is important to understand the effect of ss-DNA on the deposition process. For this purpose, DNA origami with different scaffold/staple ratios (1:1 to 1:10) were successfully synthesized *via* thermal annealing process and purified by the same methods (Table 2). The corresponding AFM images on mica (Figure 34A) show the well-defined DNA origami structures. DNA origami nanostructures were also deposited on freshly-cleaved HOPG surface. Immediately after the deposition process, AFM imaging was performed to examine the shape of the DNA triangles (Figure 34B) showing that the shape of DNA origamis were similar in all cases. The deposition of the DNA nanostructures was achieved on HOPG no matter what staple/scaffold ratio was used in the synthesis. However, all the AFM images show the deformation of lateral segments of the DNA triangles, which is consistent with our earlier observations. No significant difference is observed between samples with different scaffold/staples ratios. As discussed above, ss-DNA has a strong interaction with HOPG surface, which presumably causes the structural deformation of DNA triangles when deposited on the HOPG surface. At the largest staple to scaffold ratio, more single-stranded staples were left over in the sample after the purification step, meaning that more single strands could be deposited on HOPG surface. However, even at a 10:1 staple/scaffold ratio, the remaining single strands did not affect the spontaneous DNA nanostructure deposition process on HOPG.

Table 2. Different reagent concentrations for the DNA origami triangle synthesis.

Experiment #/ Reagent Volume (µL)	1	2	3	4	5
M13mp18 single stranded phage DNA solution (454 nM)	8.57	0	0	3.00	9.00
M13mp18 single stranded phage DNA solution (52. 8 nM)	0	8.57	14.3	0	0
DNA staple strand mixture solution (300 nM each)	15.0	15.0	15.0	15.0	15.0
Deionized water (µL)	77	77	71	82	76
1 × TAE-Mg buffer (µL)	181	181	181	181	181
Staple/Scaffold Ratio	1.2:1	10:1	6:1	3:1	1:1

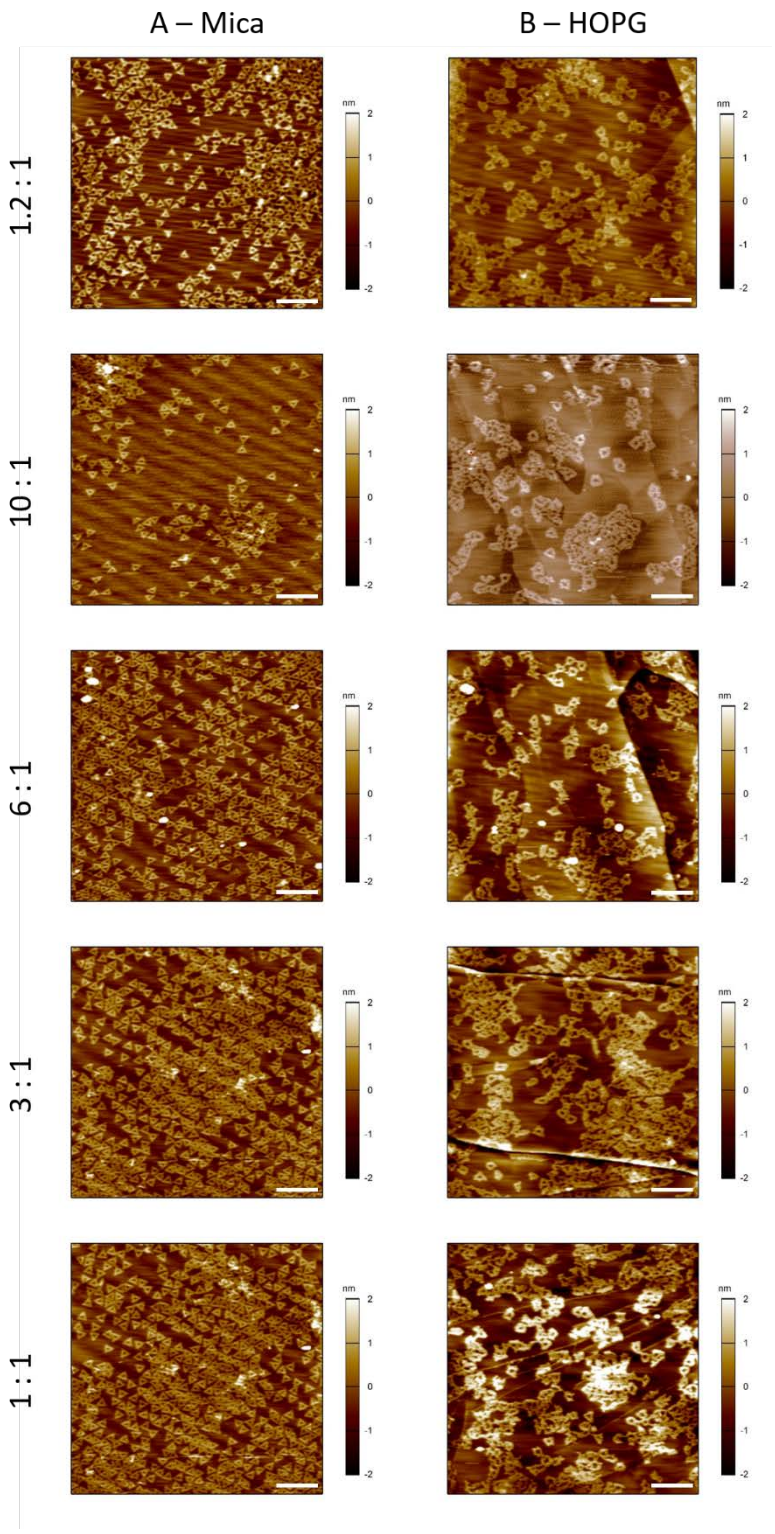

Figure 34. AFM images of DNA triangles synthesized with different staple/scaffold ratios and deposited onto mica (A) and HOPG (B). Scale bars denote 500 nm.

Another approach we used was the addition of a non-hybridizing DNA single strand to the DNA origami solution. This DNA single strand does not contain a complimentary sequence longer than 8 nucleotides with respect to the M13mp18 single stranded phage DNA and any of the staple strands. The mixture (ratio of ss-DNA/DNA origami = 0 - 5) was deposited on freshly-cleaved HOPG surface. The final concentrations of DNA triangle and irrelevant DNA single strand in each sample are listed in Table 3. The AFM images of these samples showed similar morphology previously observed, demonstrating that the added DNA single strands did not significantly affect the deposition of the DNA nanostructures on HOPG (Figure 35).

Table 3. Molar concentration of DNA triangles and irrelevant ss-DNA in different experiments.

Sample number/Conc. (nM)	1	2	3	4
DNA Triangle	1.2	1.2	1.2	1.2
Irrelevant DNA single strand	0	1.2	3.0	6.0

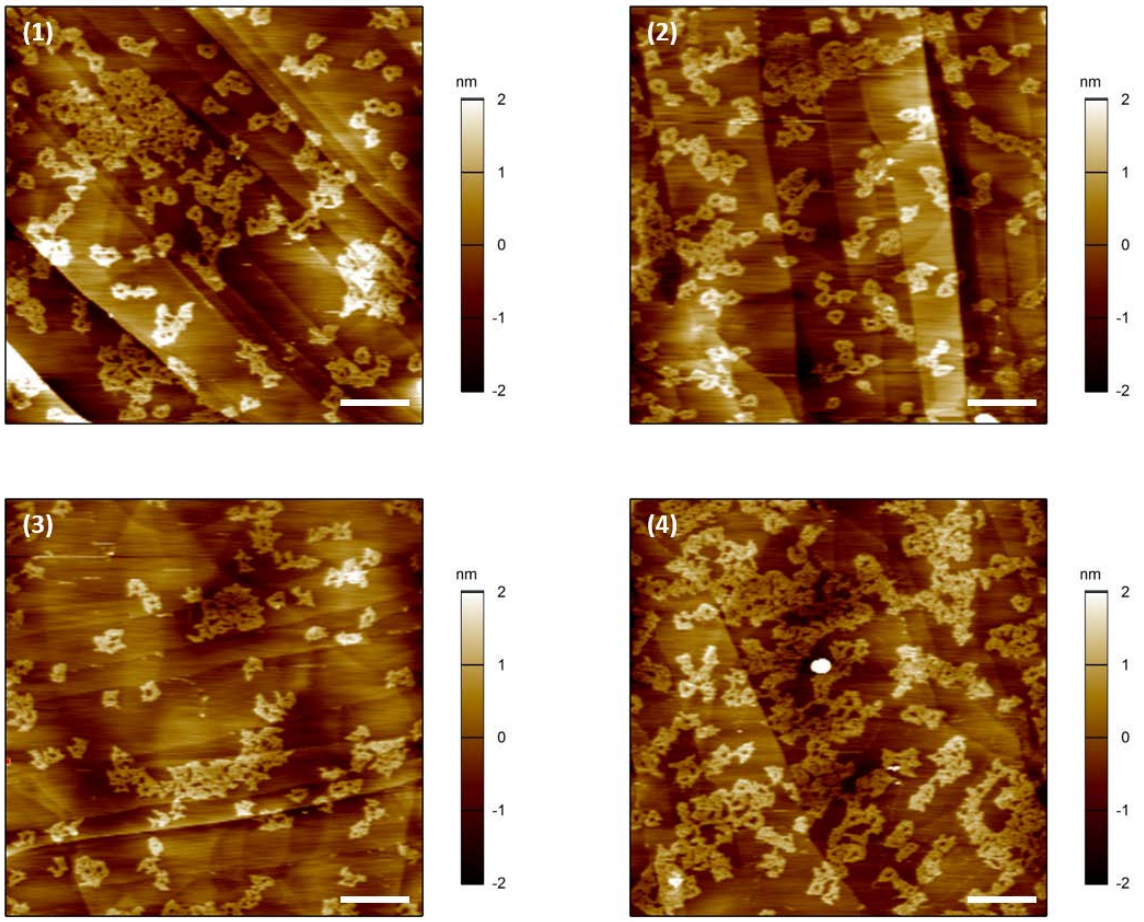

Figure 35. AFM images for mixture of DNA triangles with different amounts of irrelevant ss-DNA. The image numbers correspond to the sample numbers in Table 3. Scale bars denote 500 nm.

3.4.10 Effect of other types of DNA samples on the deposition process

We have also used other types of DNA and DNA nanostructures such as λ-DNA and DNA tile nanostructures for the deposition (Figure 36). Surprisingly, the deposition of these DNA nanostructures onto HOPG was not successful. A possible explanation could be due to limited surface area of these DNA structures, leading to much smaller Van der Waals interaction with the HOPG surface.

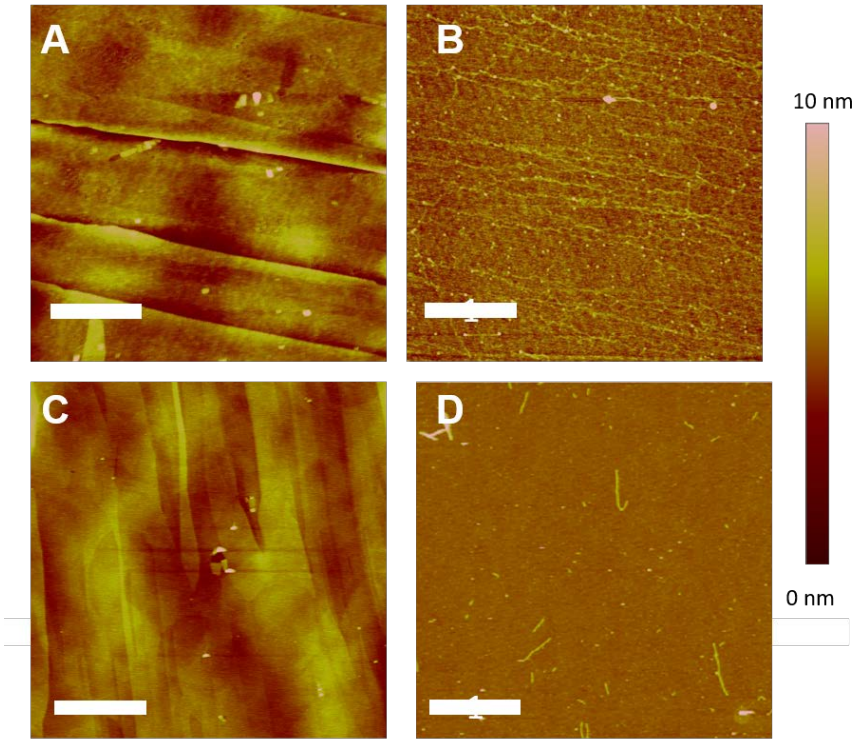

Figure 36. AFM images of the deposition of other DNA samples. (A) λ-DNA on HOPG. (B) λ-DNA on Si/SiO_2. (C) Tile DNA on HOPG. (D) Tile DNA on Si/SiO_2. Scale bars denote 750 nm.

3.4.11 CVD deposition of SiO_2

HOPG is one of the most common substrates used for imaging and deposition of nanomaterials.[238, 239] More importantly, with the exception of step edges, the basal plane of HOPG is chemically inert. This particular feature makes HOPG a desirable substrate if one wishes to initiate chemical transformation on and only on the deposited DNA nanostructure. As an example, we previously reported that DNA nanostructures can promote CVD of inorganic oxides.[141] In that work, the DNA nanostructures were supported on a Si/SiO_2 substrate, which is also active for CVD. As a result, it was difficult to confine the CVD of SiO_2 only on DNA nanostructure.

We carried out CVD growth of SiO_2 on the DNA origami deposited on HOPG using TEOS, NH_4OH, water, and isopropanol, following our previous work.[141] As shown on Figure 37A, the growth of SiO_2 was successful after leaving the sample undisturbed in a 300 mL chamber with 2 mL of each reagent. The average SiO_2 growth was *ca.* 8.5 nm, as shown in the cross-section analysis. XPS data confirm the presence of SiO_2 after the CVD growth, with a surface Si coverage of (4.35 ± 0.76) atom % (Figure 37B). The thickness of CVD-grown SiO_2 is much higher compared to our previous report of SiO_2 growth on DNA triangles deposited on a Si/SiO_2 substrate (*ca.* 2 nm).[141] We attribute the improvement to the inertness of the HOPG substrate, which improves the spatial selectivity and also allows more aggressive reaction conditions to be used. XPS analysis of the carbon peak before and after the CVD growth were similar, demonstrating that the CVD process is selective and that most of the HOPG surface was not covered by SiO_2 (Figure 38). The CVD growth of TiO_2 was also explored but was not as successful due to the high reactivity of the TiO_2 precursor, which leads to TiO_2 deposition at the reactive step edges of HOPG.[240]

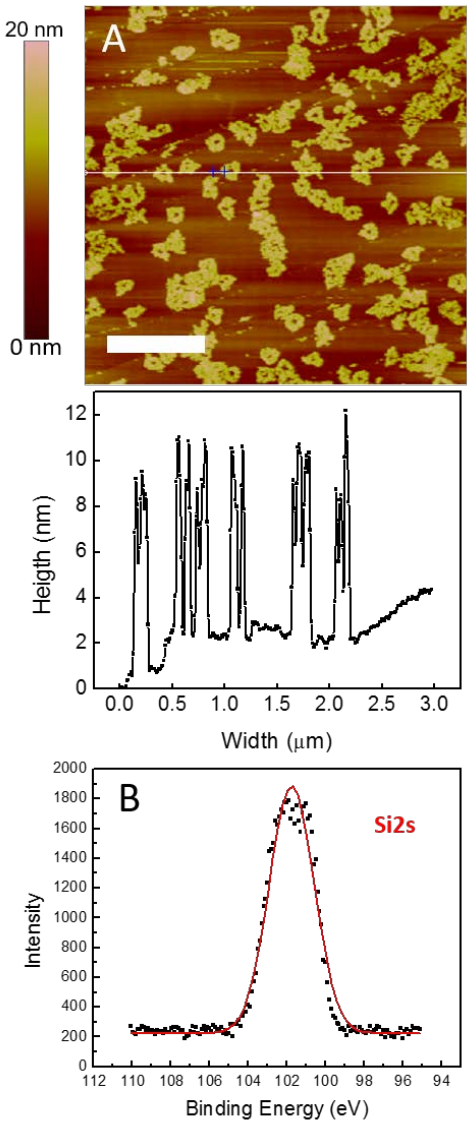

Figure 37. (A) Representative AFM images and cross-section analysis of the CVD growth of SiO_2 on the DNA triangles deposited on the HOPG surface. The scale bar denotes 750 nm. (B) Typical XPS spectrum (Si 2s) of the sample after CVD growth of SiO_2.

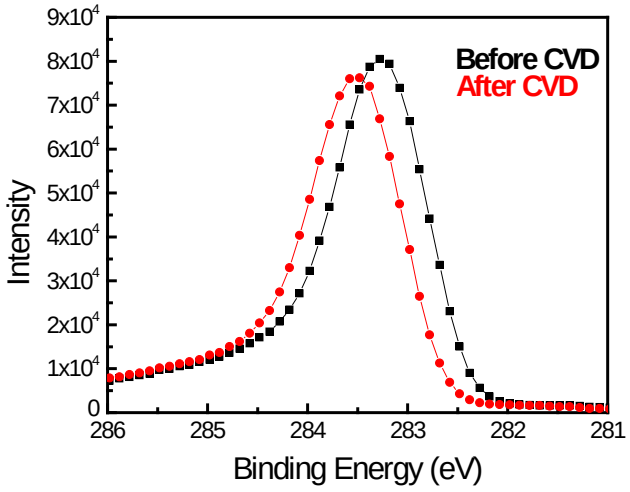

Figure 38. XPS analysis of the carbon peak before (black) and after (red) the CVD growth.

3.5 CONCLUSION

In summary, we have studied the deposition of DNA nanostructures on HOPG from an aqueous buffer solution. No surface modification on the HOPG was needed to achieve the deposition. We observed significant structural deformation of the DNA nanostructure, which we attribute to the π-π interaction between the DNA bases and the HOPG substrate. The deposition was not sensitive to the surface contamination of the HOPG surface by airborne hydrocarbon. The deposited DNA triangles were stable for at least a week and promote site-selective chemical vapor deposition of SiO_2. We hope this study will expand the use of DNA nanostructure in a broader range of surface-related studies and applications.

4.0 INTERFACIAL INTERACTION OF CVD GRAPHENE WITH DNA ORIGAMI NANOSTRUCTURES

4.1 INTRODUCTION

Synthetic DNA offers the possibility of creating an array of nanostructures, varying in size and shape. Since the report of Rothemund, where he created multiple nanostructures with high contrast at the nanoscale level,[122] many 2D and 3D structures have been synthesized with larger and more complex features.[115, 119] This type of DNA structures have the potential to be used in sensing,[241] patterning and lithography,[141, 242, 243] assembly of nanoparticles,[133, 134] among other applications. While the synthesis and application of DNA origami is quickly growing, the structures are very delicate and quickly degrade when exposed to acidic, alkaline and mild (300 ˚C) temperature conditions.[138, 151] It is essential to preserve the structure and optimize the stability conditions of the DNA origami to maximize its applications.

Graphene, a single atom thick of sp^2 carbon,[43] could improve the stability of DNA origami, if used as an encapsulating agent. Because of its thermal stability and high Young modulus, many reports have surfaced where graphene were used as a protective coating to reduce friction,[244, 245] improve lubrication properties[246] and protect the oxidation of metals, such as copper.[247, 248] Being atomically thin and flexible, graphene does not affect AFM imaging of the underlying DNA nanostructure, which facilities the characterization process and analysis of interest.

Oxidation has traditionally been the most common method to modify graphene and its derivatives to tune their properties, and explore their functionalization.[249] Specifically, the atmospheric oxidation and patterning of graphene has been well studied because of its potential in integrated electronics and technological applications.[250-252] Controllable oxidation can be a useful tool to functionalize the surface of graphene and manipulate its properties in a selective manner. For these reasons, an understanding of the stability of graphene under oxygenating conditions and in the presence of site-specific patterning materials is necessary.

The concept of encapsulation of materials using graphene is quickly growing. There have been multiple reports of using graphene to encapsulate water,[180-182] DNA[183, 184] and DNA nanostructures,[185] biosensors,[186] and nanoparticles.[189] A recent publication claimed that the encapsulation of DNA origami helps with the protection of the structures from water and AFM force manipulation.[185] While it is important to analyze the force resistance of DNA origami, studying the structure integrity of DNA nanostructures under high temperature could offer a better perspective in understanding the encapsulation effect of graphene on DNA origami.

The interest of combining DNA origami with graphitic materials is not limited to encapsulation. In recent years, DNA nanostructures have been self-assembled on modified graphene and HOPG with or without surface modification.[167, 174-176, 178] It is important to investigate if the origami after modification, encapsulation or deposition into a substrate conserves its original properties and shape. However, the stability mechanism of the experiments performed and the DNA nanostructures is not always explained, allotting to the uncertainty if these studies are suitable for the applications proposed.

Herein, we report the encapsulation and thermal stability study of DNA origami triangles using CVD graphene as the encapsulating agent. The samples were exposed to a series of

thermal annealing manipulations and AFM images were taken at the same location to observe the effect of temperature on DNA origami triangles. The DNA nanostructure was more stable under graphene when compared to that deposited on Si/SiO_2. It was also observed that the salt residue from the origami conserved the triangular shape after the DNA nanostructure destruction. Additionally, triangular holes were observed upon the atmospheric oxidation of graphene. We attributed this observation to the salt residue of the DNA triangle acting as a promotor for graphene oxidation. This encapsulation technique could potentially be used in the fabrication of DNA devices that would degrade under harsh environments. This research also presents the possibility of patterning graphene on the nanometer scale.

4.2 EXPERIMENTAL SECTION

4.2.1 Materials

DNA strands were synthesized by Integrated DNA Technology, Inc. or purchased from Bayou Biolabs, LCC. Acetic acid, EDTA, magnesium acetate, PMMA and tris(hydroxymethyl)aminomethane were purchased from Sigma Aldrich. The bench top microcentrifuge was purchased from Fisher Scientific, USA. The 30 kDa MW centrifuge filters (Nanosep Centrifugal Devices with Omega Membrane) were purchased from Pall Corporation, Port Washington, NY. Si wafers containing 300 nm of SiO_2 (Si/SiO_2) were purchased from University Wafers. The copper foil for the CVD synthesis was purchased from Alfa Aesar (99.8 %, 25 μm thick). The furnace for the CVD synthesis and annealing experiments was purchased from Thermo Scientific (Linderg Blue M, model number TF55030A-1). The plastic Petri Dish

used for the deposition of DNA origami were purchased from VWR International LLC. The Kimwipes used to maintain a humid environment during the deposition process were obtained from Kimberly Clark.

4.2.2 Characterization methods

AFM images were taken with a Digital Instruments Nanoscope IIIA from Veeco Systems in tapping mode using silicon tips with a resonance frequency of approximately 320 kHz. All images collected had a scan size of 3 μm by 3 μm, and a scanning rate of 0.50 Hz and 512 samples per line.

Room temperature micro-Raman spectra were conducted on a custom-built setup using 532 nm single-longitudinal mode solid-state laser with a spot size less than 1 μm. A 40x objective (NA: 0.60) was used in all the micro-Raman experiments. Each Raman spectrum was taken with 60 seconds of integration time with a low incident laser power of less than 1 mW at the entrance aperture to avoid laser induced thermal effect on graphene.

4.2.3 Synthesis of DNA origami nanostructures

Triangular-shaped DNA nanostructures were synthesized using a previously published method[122] by mixing 15.0 μL of DNA staples (300 nM for each staple), 8.60 μL of M13mp18 DNA (454 nM), 77 μL of DI water and 181.0 μL of a TAE/Mg buffer. The stock TAE/Mg buffer solution contains the following reagents with its respective concentrations: 150.0 mM of $Mg(OAc)_2$, 2.0 mM of acetic acid, 2 mM of EDTA, and 40 mM of tris(hydroxymethyl)aminomethane. The stock solution was then diluted for all the experiments and the concentrations were 12.5 mM of

$Mg(OAc)_2$, 0.17 mM of acetic acid, 0.17 mM of EDTA and 3.33 mM of tris after dilution. The diluted TAE/Mg solution with the DNA was then heated to 95 ˚C and slowly cooled down to 25 ˚C at a rate of 1 ˚C min^{-1}. After the cooling process was completed, the sample (*ca.* 280 μL) was divided equally and transferred into two separate 30 kDa MW centrifugal devices (Nanosep Centrifugal Devices with Omega™ Membrane, Pall Corporation, Port Washington, NY). Additional *ca.* 400 μL of diluted buffer solution was added into each centrifugal device and the mixtures were centrifuged at a speed of 6000 rpm using a single speed benchtop microcentrifuge to remove the excess DNA staple strands. The DNA origami solution was centrifuged until 1/3 to 1/4 of the original volume was left to ensure that the solution was not completely centrifuged to dryness. The process of adding buffer and centrifuging was repeated five times. The final DNA triangle solution was stored inside plastic vials at 4 ˚C.

4.2.4 Cleaning of Si/SiO_2 wafer

A clean Si wafer with 300 nm of oxide was used as a support for the DNA origami encapsulated with CVD graphene samples. In order to preserve a clean sample, the wafer was immersed in a piranha solution composed of H_2SO_4:H_2O_2 (70:30 v/v) and left undisturbed for 30 minutes. *Warning: piranha solution presents an explosion danger and should be handled with extreme care; it is a strong oxidant and reacts violently with organic materials. All work should be performed in a fume hood. Wear proper protective equipment.* The sample was then removed and copiously rinsed with DI water (> 10 mL) and blow-dried with N_2 gas.

4.2.5 Deposition of DNA origami triangles on a Si/SiO_2 wafer

The synthesized DNA origami solution was diluted with the TAE/Mg buffer and 10 μL was deposited using a micropipette to a Si/SiO_2 substrate prepared using the procedure described in section 4.2.4. The purpose of the dilution was to ensure that no more than a monolayer of DNA origami was deposited on the surface. The Si/SiO_2 wafer was then left undisturbed for 40 min in a plastic Petri dish. To keep a humid environment and avoid evaporation, a wet Kimwipe was put between the cover and the bottom of the Petri dish. The substrate was then slowly dried using a rubber tube to flow N_2 gas and then completely immersed in a 90%-10% (v/v) ethanol-water solution for 10 s to remove any residues present from the buffer solution. The rinsing solution was used once for every sample prepared. Finally, the sample was air dried using N_2 gas. To ensure complete removal of the salt residue, the immersion and drying steps were repeated three times.

4.2.6 CVD synthesis of graphene

The CVD synthesis process used in this work was first reported by Li *et al.*[86] In a typical experiment, a copper foil was cleaned by rinsing in concentrated HCl, DI water and blown dry with N_2 gas. The clean Cu foil was placed in the center of a quartz tube. The tube was then evacuated, back filled with H_2 (g) and heated to 1000 °C using a furnace under a H_2 flow maintained at 2.0 SCCM and a pressure of 70 mTorr. After annealing the Cu inside the furnace for 60 min under H_2 flow, CH_4 (g) with a flow rate of 20 SCCM was introduced into the furnace at a total pressure of 500 mTorr. After 30 min (graphene growth time), the furnace was turned off and allowed to cool to room temperature under H_2 and CH_4 gas flow.

4.2.7 Transfer of CVD graphene onto a Si/SiO_2 wafer containing DNA origami triangles

PMMA (50 mg mL^{-1} solution in anisole) was spin coated on the Cu foil containing graphene. Since graphene grows on both sides of the Cu, the graphene on the non PMMA coated Cu surface was removed by placing the Cu foil in an etching solution (1M $FeCl_3$ in 10 % HCl) for 2 min followed by a gentle wipe using a Kimwipe. The PMMA/graphene/Cu foil was then placed again in the etching solution for 20 minutes to etch away the Cu foil. The floating PMMA/graphene was then transferred to a D.I. water bath to wash away etching impurities and was fished onto a clean Si/SiO_2 wafer and dried in air for a minimum of 30 min. To avoid impurities, the sample was covered with a glass Petri dish. A drop of PMMA solution was then placed on top of the sample covering the entire surface and was left undisturbed for 30 min. The sample was then placed in an acetone bath overnight to dissolve PMMA. The sample was rinsed with copious amounts of fresh acetone and blown dried using N_2 gas.

4.2.8 Thermal annealing process

The annealing experiments were performed in a furnace with a quartz tube in air. The furnace was heated to the desired temperature before the sample was placed in a quartz boat and pushed towards the middle of the quartz tube. After the annealing was completed, the sample was pushed towards the end of the tube. It was important to ensure that the sample received heat only when it was under thermal annealing inside the furnace. This way, the time the sample was receiving heat was well controlled. To avoid heat transfer from the quartz boat, the sample was immediately removed from the quartz boat and transferred onto a clean glass Petri Dish. The

sample was then left undisturbed for 30 minutes allow the sample to cool until it reached room temperature. After the cooling process, the sample was characterized by AFM imaging.

4.3 RESULTS AND DISCUSSION

4.3.1 Morphology and characterization of DNA origami triangles upon deposition of CVD graphene

In a typical experiment, shown in Figure 39A, synthesized DNA origami with a triangular shape was deposited to a Si wafer with 300 nm of thermal oxide (Si/SiO_2). CVD graphene was then transferred to the wafer containing the DNA nanostructures. AFM imaging was performed to examine the DNA origami underneath the graphene. The shape of the DNA origami was not affected and the triangles are well-defined under the graphene. Figure 39B shows an AFM image of DNA triangles covered by CVD graphene. The prepared sample is relatively clean and uniform, with typical graphene wrinkles due to the transfer process from the copper foil to the Si/SiO_2 substrate. Small pink dots are observed at the bottom of Figure 39B which we attribute to PMMA residue from the transfer process.

The total height of the nanostructures is slightly higher under the CVD graphene with a height of (1.65 ± 0.05) nm when compared to DNA triangles on a Si/SiO_2 substrate with a height of (1.53 ± 0.08) nm, shown in Figure 39C. This height difference of the origami nanostructures could be due to the presence of monolayer graphene that may cause a change in the tip-sample interaction since the AFM tips are hydrophilic and the graphene is hydrophobic. Another possible explanation of the height difference is that during the sample preparation the silicon

wafer containing the DNA triangles is briefly submerged in water to capture the suspended graphene. It is possible that water was trapped between the graphene and the origami, making the height of the triangle higher. The shape of the DNA triangle is well-preserved under graphene. The measured FWHM of 10 DNA triangles underneath the graphene was (24.0 ± 5.0) nm while outside the graphene was measured to be (28.2 ± 5.9) nm, demonstrating no statistical difference in their morphology.

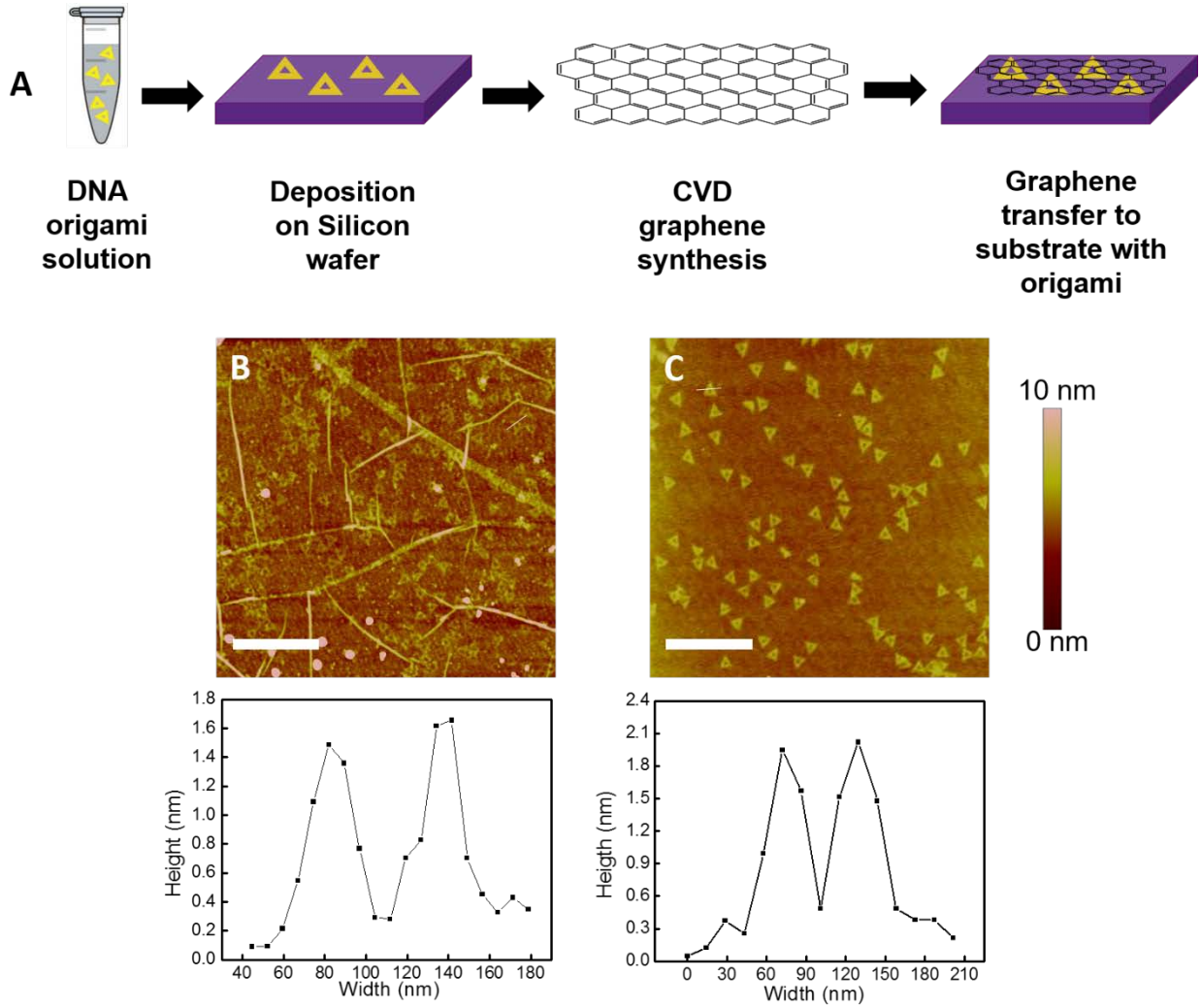

Figure 39. (A) Scheme of the deposition of CVD graphene on a Si water containing DNA origami triangles. AFM image and cross-section analysis of the DNA origami underneath CVD graphene (B) and bare Si/SiO_2 (C).

4.3.2 Raman spectroscopy

Micro-Raman spectra were collected in three different spots on the sample from Figure 39. A representative Raman spectrum, shown on Figure 40 shows two major peaks: the G peak at *ca.* 1589 cm^{-1} and the 2D peak at *ca.* 2685 cm^{-1}. No D peak was observed in the sample. The height ratio between the intensity of 2D and G peaks (I_{2D}/I_G ratio) is (1.21 ± 0.12) and the 2D peak is narrow, suggesting single-layer graphene.[196] Overall, the DNA origami does not affect the vibrational modes of graphene.

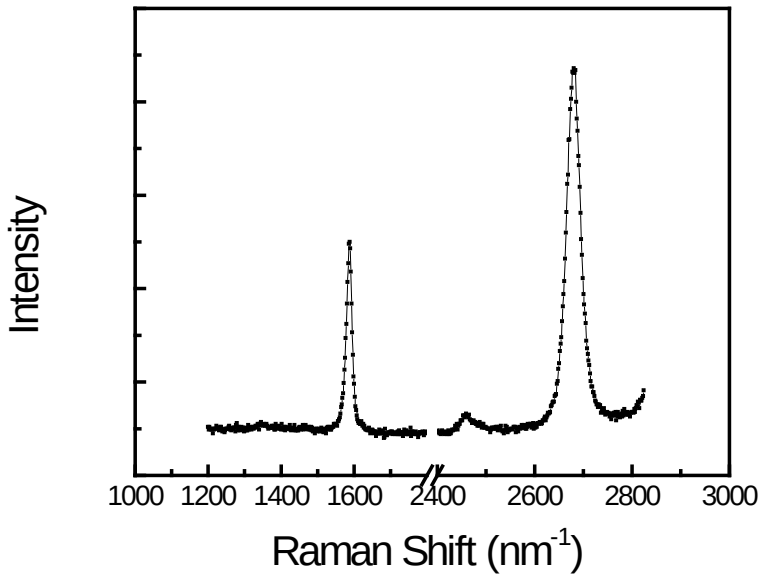

Figure 40. Micro-Raman spectra of the sample shown on Figure 1B.

4.3.3 Stability of DNA origami underneath CVD graphene

We investigated the thermal stability of DNA triangles underneath graphene over an extended period of time. Our group reported that CVD graphene oxidizes and is partially destroyed on the edges and defects when annealed air at 550 ˚C after 20 minutes.[250] A sample was annealed for 30

minutes in air and the temperature was increased by 50 °C until we observed the complete destruction of graphene. After the deposition of DNA triangles and CVD graphene on the Si/SiO_2 wafer, same-location AFM images were taken.

AFM images show that the DNA triangles under graphene at room and mild annealing temperatures ranging from 23 ˚C to 200 ˚C are visible and well-defined (Figures 41A-D). Cross-section analysis demonstrated that the height difference between the triangles up to 200 ˚C are within one standard deviation. We also found that after 250 °C (Figure 41D), there is a sudden decrease on the density and height of the DNA triangles on the image. When the sample was annealed at 400 ˚C, the DNA origami seems to disappear from the surface (Figure 41F). As the annealing temperature keeps increasing to 450 and 500 ˚C the DNA origami is still not visible (Figure 41G-H). At 550 °C (Figure 41I) the graphene is destroyed and triangular-shaped inorganic DNA residue (*i.e.* magnesium phosphate) are observed outside of the graphene (marked with a white arrow).[151] The DNA residue conserved the triangular shaped and the lateral sides had a height of (1.54 ± 0.21) nm. We attribute the height difference to DNA salt residue accumulation. Cross-section analysis showed that the height of the graphene was (1.65 ± 0.07) nm, in accordance to literature reports. The value of the measurement is higher than the theoretical value of 0.33 nm due to the change in the tip–sample interaction as the tapping tip scans over the surface.[253] Further cross-section analysis of the structural evolution of three triangles confirmed that the height of the triangles decreases as the temperature increases. The average height of the triangles on Figure 41A was (1.39 ± 0.13) nm while the height of the triangles on Figure 41H was (0.47 ± 0.03) nm, representing a 66.2% height loss. Figure 42 depicts the average height loss of three DNA triangles as the annealing temperature increased. Based on these findings, we determined that the ideal temperatures to monitor the behavior of the

DNA origami under graphene are 300 ˚C and 400 ˚C because at 300 ˚C the triangles are still visible while at 400 ˚C the triangles first started to disappear from the image, an observation worth studying.

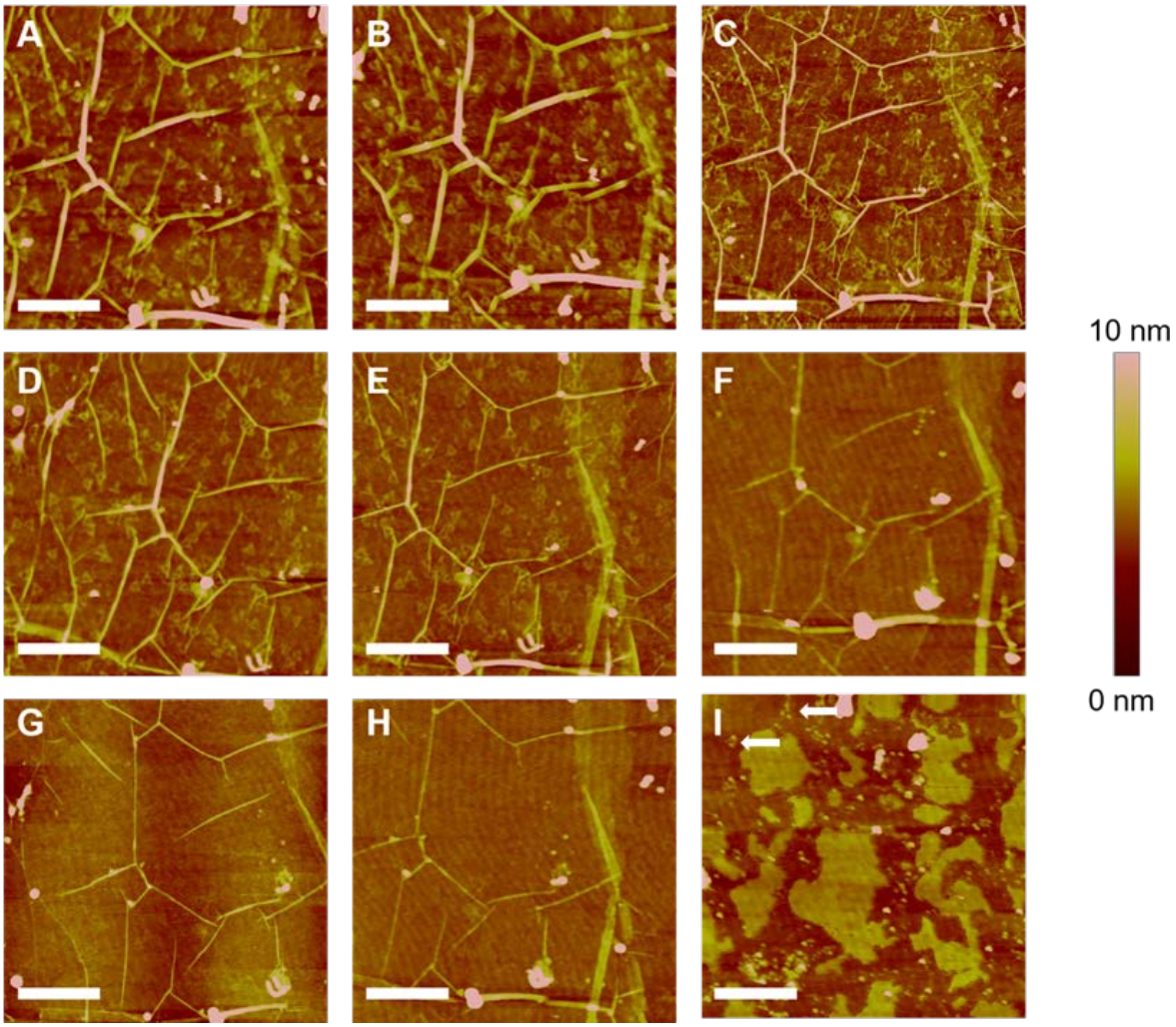

Figure 41. Same-location AFM images of DNA origami underneath CVD graphene at different temperatures: (A) 23 °C. (B) 100 °C. (C) 200 °C. (D) 250 °C. (E) 300 °C. (F) 400 °C. (G) 450 °C. (H) 500 °C. (I) 550 °C. The scale bar denotes 750 nm. White arrows points to inorganic residue from the DNA origami triangles.

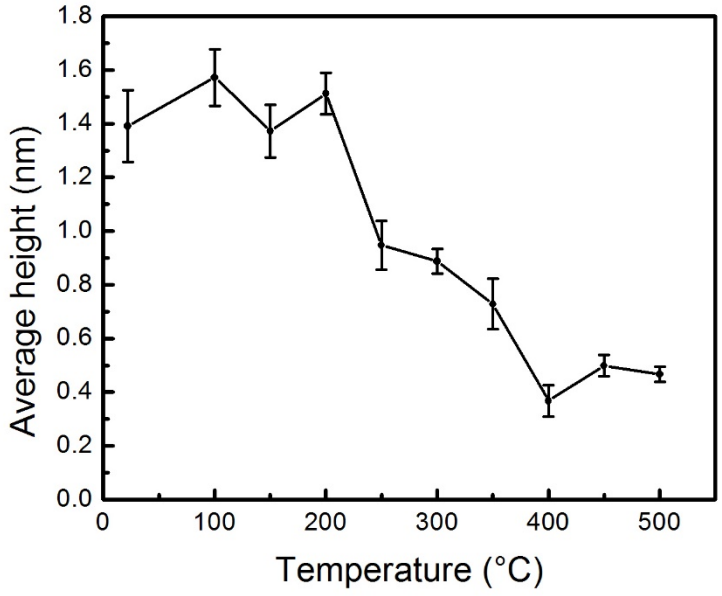

Figure 42. Structural evolution of three DNA origami triangles measured as the average height (nm) of the DNA origami as a function of the annealing temperature (˚C).

4.3.4 Analysis of the thermal stability of DNA origami at 300 ˚C

Since the previous experiment demonstrated that 300 °C was the last temperature where the DNA triangles were observed, a study was carried out to analyze the effect of the heating time in the stability of the DNA tringles under graphene. The temperature remained constant at 300 ˚C, but the annealing time was slowly increased from 5 minutes to 29 hours, using 30-minute intervals. Figure 43 shows representative AFM images of the same 3 μm by 3 μm location after annealing the sample. Cross-section analysis of three DNA triangles showed that the initial height of the DNA origami was (0.97 ± 0.22) nm which was lower than the previous experiment. We attribute this height difference to the tip-sample interaction. The DNA origami triangles were visible and stable with no clear deformation for at least 60 minutes (Figure 43A-C). Cross-

section analysis of the origami height does show a small decrease in height after 1 hour with a 29.6 % height loss when compared to the sample at room temperature (See Table 4).

After 5 hours of thermal annealing, the DNA triangles seem to disappear from the surface (Figure 43D) and the height of the triangles was not measurable. Regarding the graphene coating, typical effects of the annealing process are shown such as the wrinkles getting smoother and the disappearance of PPMA residue (Figure 43E). No visible change was observed until the sample was annealed for a total of 23 hours where the DNA origami triangles were again observed (Figure 43F). The cross-section analysis showed that the height decreased to (0.671 ± 0.058) nm, representing a 30.8% height loss. After 27 h of thermal annealing the DNA origami triangles appeared to be completely destroyed since their features are difficult to identify and the DNA height was difficult to measure (Figure 43H).

After 29 hours of thermal annealing, the graphene was completely oxidized. While most of the graphene was destroyed, the top part of the sample was preserved and holes were observed (some triangular) in the same location where the DNA triangles were observed before the annealing process (Figures 43A and 43I). An inset of the AFM images before (Figure 43A) and at the end of the thermal annealing (Figure 43I) with the cross-section analysis of the same DNA origami triangle (blue square) is shown in Figure 44. The depth of the holes of the three DNA triangles measured was (1.16 ± 0.30) nm, corresponding to the height of single layer graphene. The length of the holes was (158.3 ± 3.7) nm which is *ca.* 1.1 times larger than the length of DNA origami. The small incongruence between the trench and DNA origami length could be due to the selective etching of the graphene edge by O_2 after the holes were formed. Cross-section analysis of a DNA triangle and its respective hole (blue square on the images) also shows that to our surprise, some triangular DNA origami residue still remained after the annealing, with

a length and height of *ca.* 60 nm and 0.3 nm, respectively. The shape of the inorganic residue has a well-defined triangular shape, similar to the behavior observed when DNA origami is annealed in air without the presence of graphene.[151] This points out to our hypothesis that graphene encapsulates the DNA and protects it from thermal decomposition.

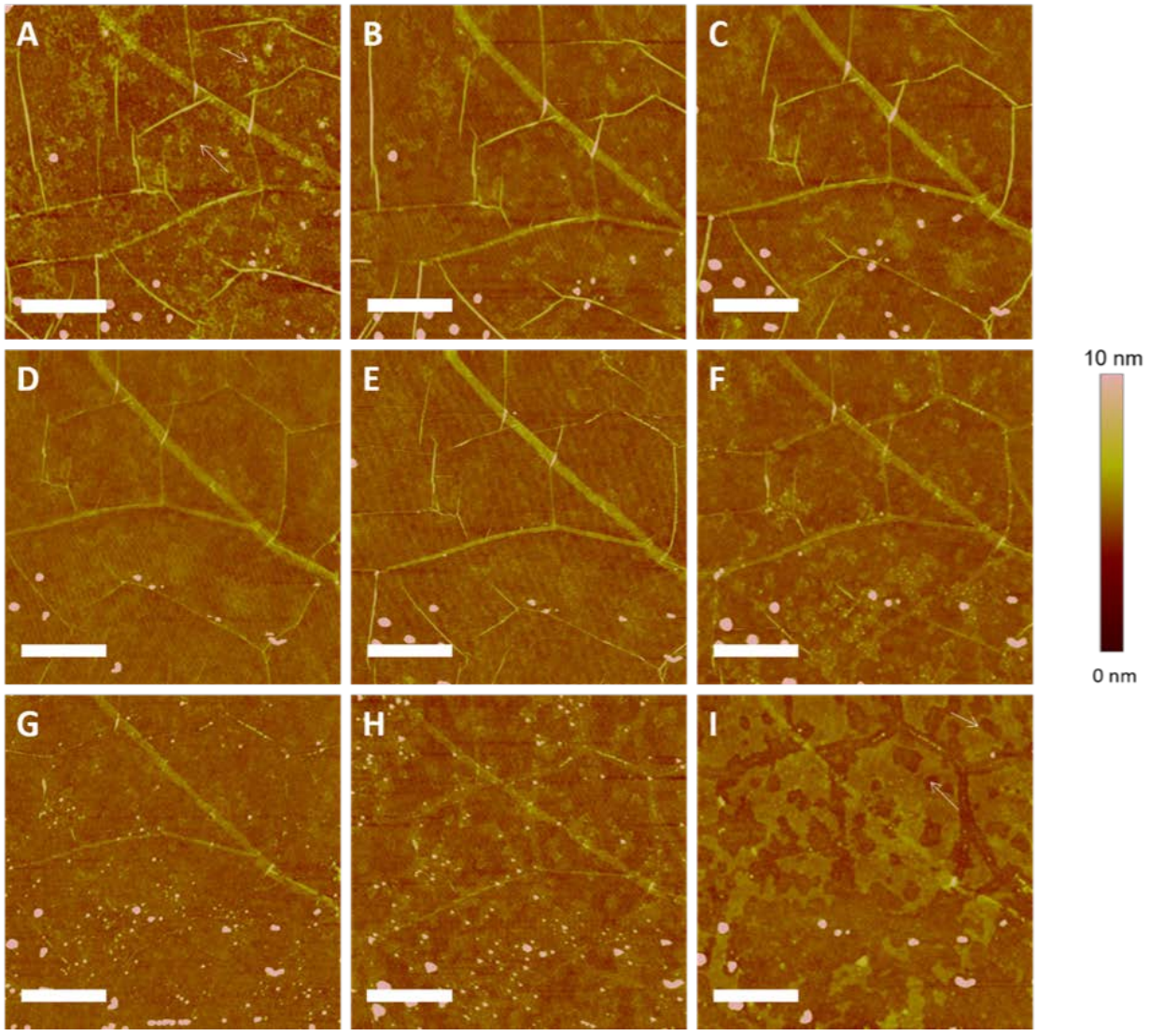

Figure 43. Same-location AFM images of DNA origami underneath CVD graphene as the annealing time increased at 300 °C: (A) Room temperature. (B) 5 min. (C) 1 h. (D) 5 h. (E) 7 h. (F) 23 h. (G) 24 h. (H) 27 h. (I) 29 h. The scale bar denotes 750 nm.

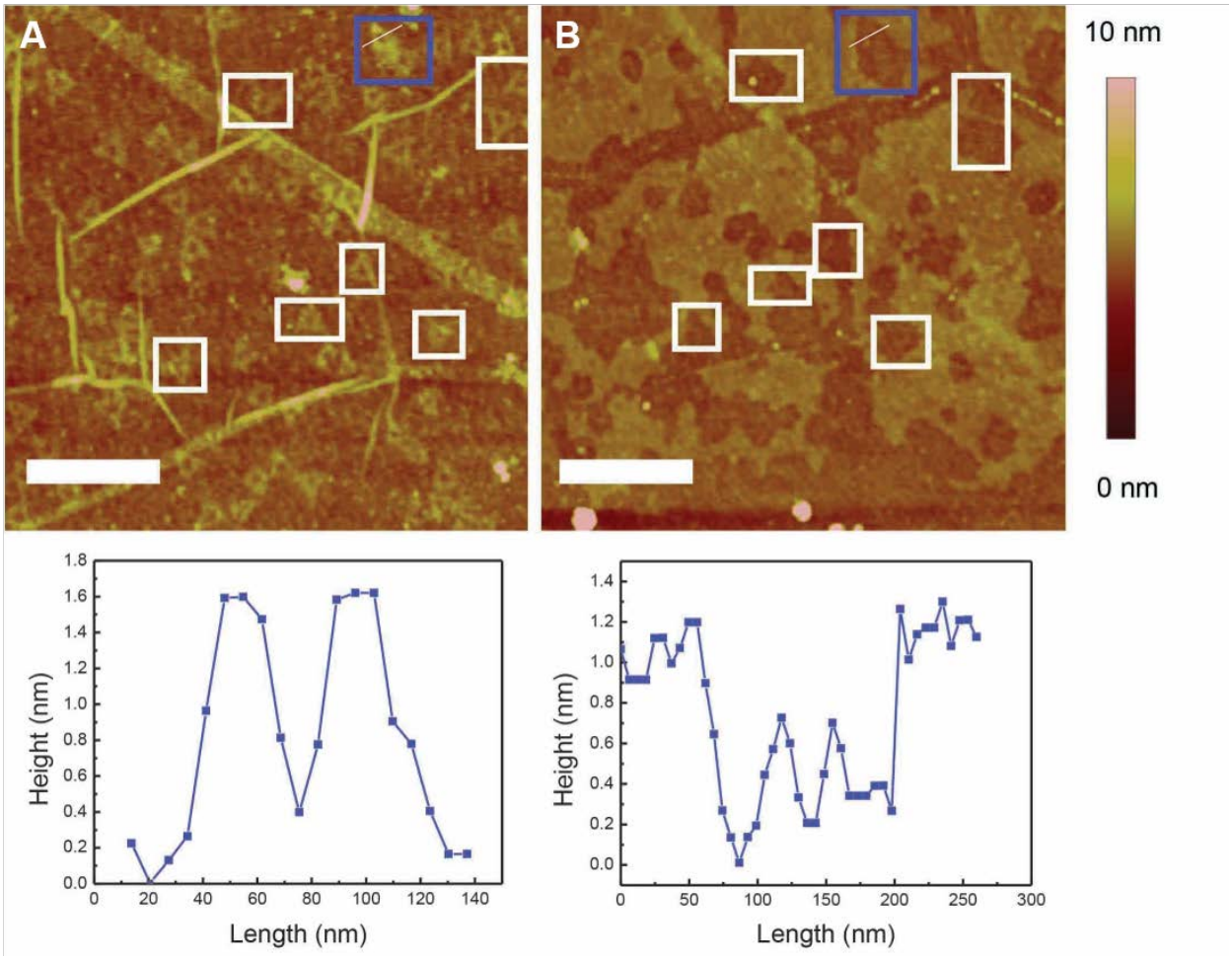

Figure 44. Zoomed AFM images and cross section analysis of a triangle in the blue square from Figure 42A (A) and 42I (B). Scale bars denote 750 nm.

Table 4. Average height of three DNA origami triangles under CVD graphene at 300 ˚C as the annealing time increased.

Time	Average height (nm)	St. Deviation (nm)
0 min	0.97	0.22
5 min	0.75	0.23
1 h	0.683	0.010
23 h	0.671	0.058
29 h	0.360	0.046

4.3.5 Analysis of the thermal stability of DNA origami at 400 ˚C

While at 300 °C we were able to observe the degradation process of the DNA triangles under graphene, the time it took to obtain the selective holes was extensive. We repeated the study and increased the temperature to 400 ˚C while the 30 minute intervals remained constant. This experiment design was based on the results from section 4.3.3 because at this temperature the triangles were not observed. Figure 45 shows representative AFM images of the same 3 µm by 3 µm location after annealing the sample. Cross-section analysis of three DNA samples determined that the initial height of the triangles was (1.07 ± 0.30) nm. The DNA origami triangle were again visible and stable at room temperature (Figure 44A).

After 2 hours of thermal annealing the DNA triangles seem to disappear from the image (Figure 45B). Cross-section analysis of the origami height show a decrease in height with a 42.6 % height loss when compared to the sample at room temperature (See Table 5). As observed in

the previous experiment, the signs of thermal oxidation are present (Figure 45C and 45D). After 6 and 8 hours of thermal annealing, the DNA triangles reappear on the image (Figure 45C and 44D). Nonetheless, cross-section measurements were not possible due to the roughness of the sample. After 11 hours of thermal annealing, the DNA triangles were visible and measurable (Figure 44E). The cross- section analysis of the height of the lateral sides of the triangles showed that the height decreased to (0.75 ± 0.26) nm, representing a 29.7 % height loss. We attribute the increase of the height to the formation of salt aggregate clusters that maintained triangular features.

Due to severe surface contamination, the same location study was moved 5 μm below the original area after Figure 45E was taken (Figure 45F and 45G). Localized holes were observed after 14 hours of thermal annealing (Figure 45H and 45I), consistent with the experiment described on the previous section. An inset of the AFM images of the DNA inorganic residue after it resurfaced (Figure 45F) and at the end of the thermal annealing (Figure 45I) with the cross-section analysis of the same DNA origami triangle (blue square) is shown in Figure 46. The depth of the holes of the three DNA triangles measured was (1.76 ± 0.41) nm, in accordance to single layer graphene within the standard deviation. The length of the holes was (132 ± 20) nm, *ca.* 1.03 times larger than DNA origami in Si/SiO_2. Overall, similar results were observed at 300 ˚C and 400 ˚C. The only notable difference is that the rate of oxidation is almost twice as fast at 400 ˚C when compared to the results of the thermal annealing at 300 ˚C.

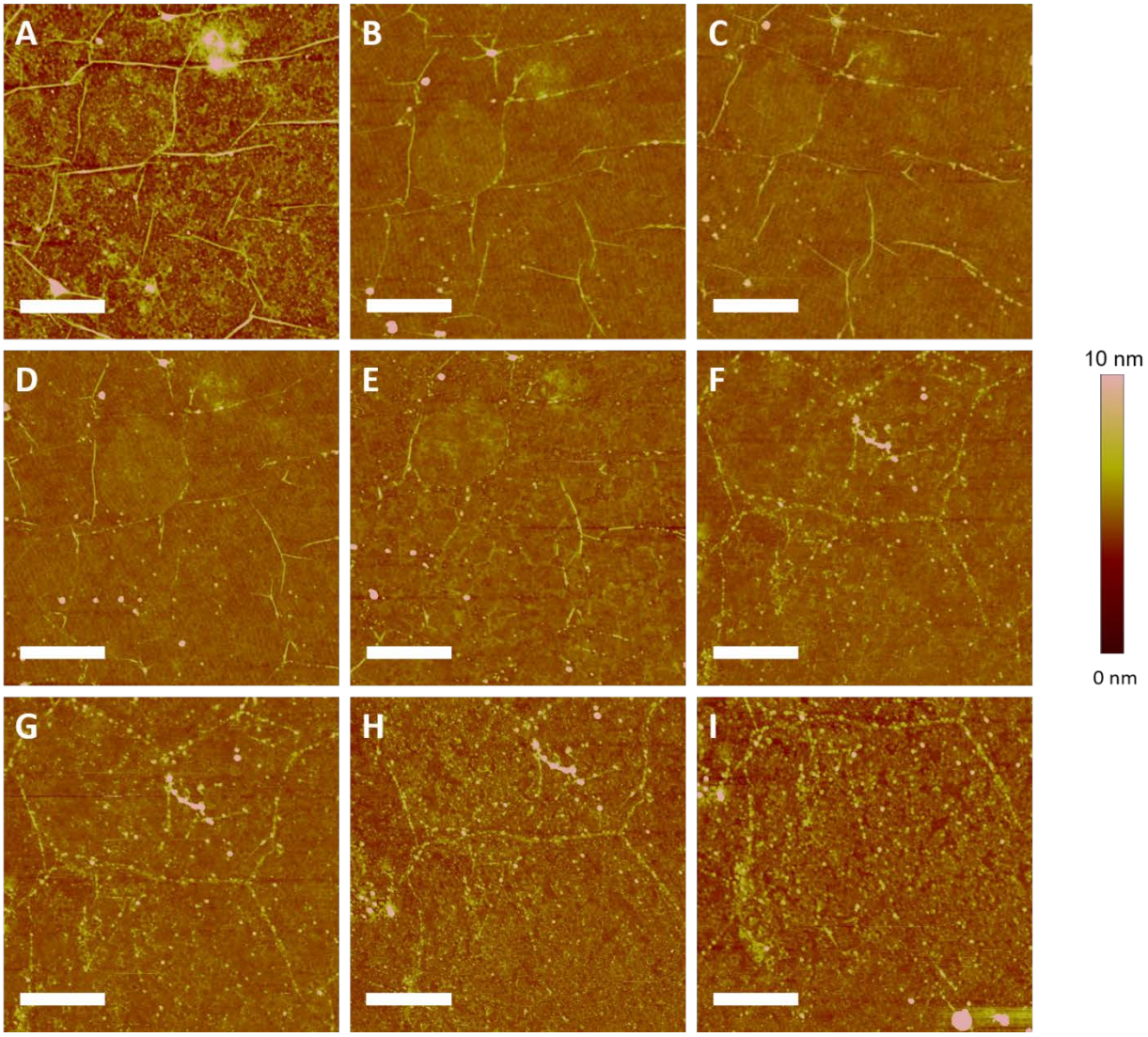

Figure 45. Figure 44. Same-location AFM images of DNA origami underneath CVD graphene as the annealing time increased at 400 °C. (A) Room temperature. (B) 2h. (C) 4h. (D) 6h. (E) 8h 30min. (F) 11h. (G) 12h. (H) 14h. (I) 14h 30 min. The scale bars denote 750 nm.

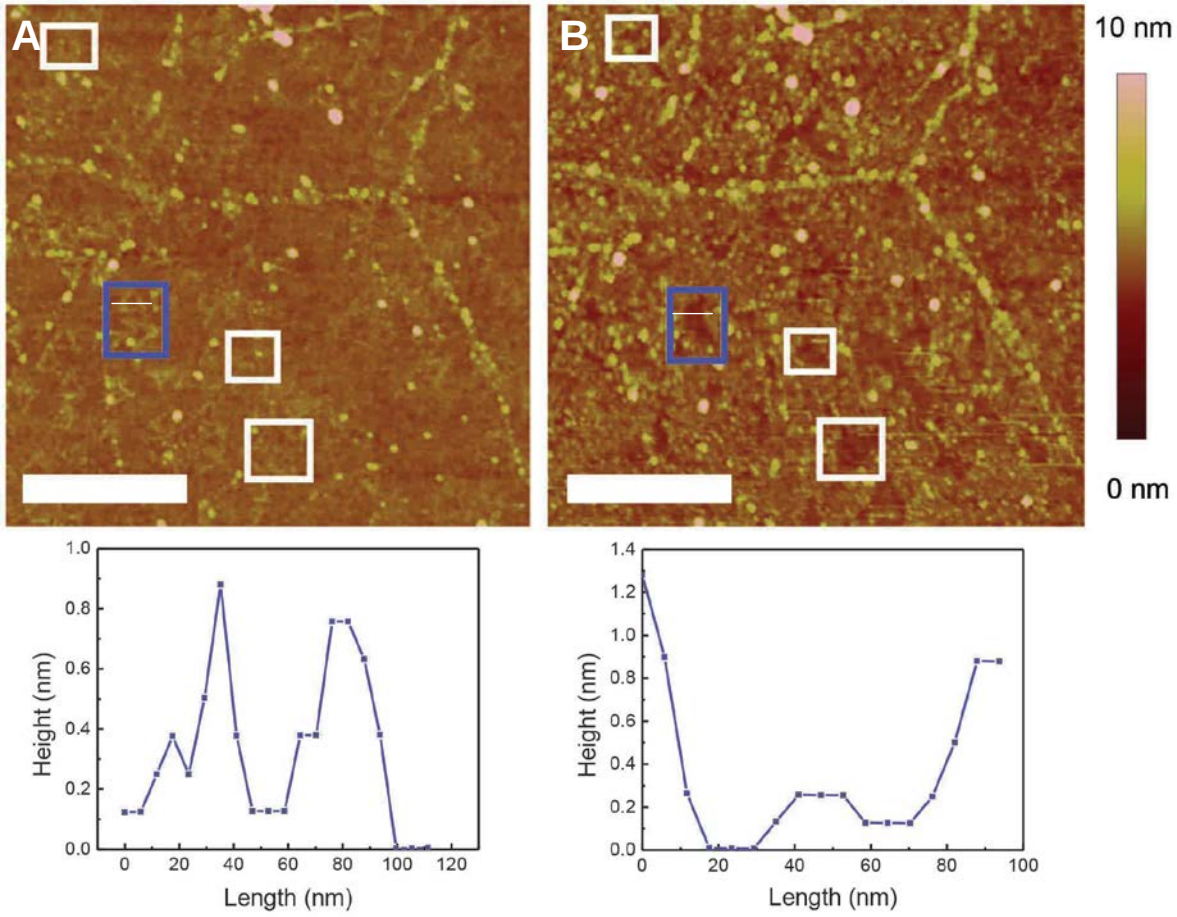

Figure 46. Zoomed AFM images and cross section analysis of a triangle in the blue square from Figure 44F (A) and 44I (B). The scale bars denote 500 nm.

Table 5. Average height of three DNA origami triangles under CVD graphene at 400 ˚C as the annealing time increased.

Time (h)	Average height (nm)	St. Deviation (nm)
0	1.07	0.30
4	0.62	0.16
11	0.75	0.26
12	1.43	0.53
14.5	1.56	0.42

4.3.6 Thermal stability of DNA origami in air

Previous reports suggested that graphene can protect and preserve the DNA origami shape and height.[185] We were interested in comparing the stability of DNA origami in air and underneath graphene. A control study was performed to analyze its thermal stability of the DNA origami in air. Separate samples were prepared and were annealed at 300 °C in air for 15 minute intervals until the DNA origami was completely destroyed. At room temperature (Figure 47A), the height of the DNA triangle sides is (1.05 ± 0.24) nm. After 15 minutes of thermal annealing (Figure 47B), the height of the origami decreased by 27 %. Shown in Figure 47C, the height of the DNA triangle decreases by 30 % when compared to the sample at room temperature (See Table 6). Nonetheless, the triangular shape of the DNA was preserved. Upon annealing for 45 minutes (Figure 47D), the density of the DNA triangles is low and most of the DNA origami is completely destroyed. Results presented on sections 4.3.4 and 4.3.5 demonstrated that the height and triangular shape of the DNA origami was conserved for at least 2 hours, confirming our

hypothesis that when DNA is encapsulated with graphene, the origami is significantly more stable when compared to DNA directly exposed to air. Nonetheless, it is important to point out that the fact that the triangular shape of the DNA nanostructure is conserved does not imply that its organic structure is still intact under the graphene.

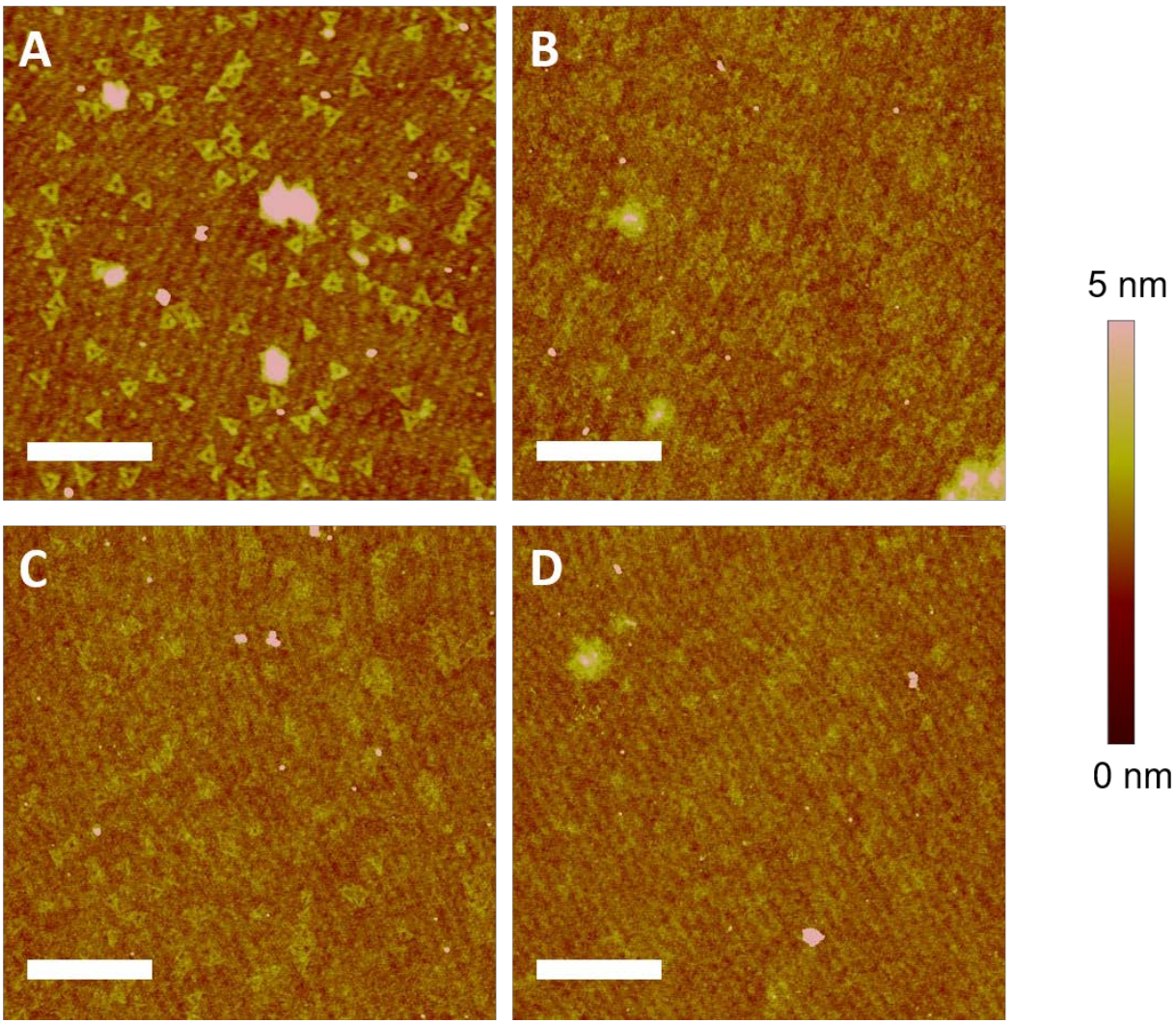

Figure 47. Same-area AFM images of DNA origami after thermal annealing at 300 °C at different times: (A) 0 min. (B) 15 min. (C) 30 min. (D) 45min. The scale bars denote 750 nm. Wavy patterns on the images are due to noise and vibrations present in the room where the AFM is located.

Table 6. Average height of five DNA origami triangles on a Si/SiO_2 substrate annealed at 300 ˚C as a the annealing time increased.

Time (min)	Average height (nm)	St. Deviation (nm)
0	1.05	0.22
15	0.76	0.18
30	0.72	0.17
45	N/A	N/A

4.3.7 Proposed mechanism

We attribute the hole formation on the CVD graphene to the interaction of water trapped between the DNA triangles and CVD graphene combined with the atmospheric oxidation of graphene. In order to understand the results described, we consider the following key steps that occur during the thermal annealing process, depicted in Figure 48:

(1) Entrapment of water on the graphene/DNA origami interface. Water from the wet graphene transfer protocol is trapped underneath the graphene and interacts with the DNA origami triangles.

(2) Evaporation of water. During the annealing process, water evaporates and creates a separation between the decomposed DNA triangles and graphene, producing small nanobubbles on the graphene lattice where the DNA triangles are located.

(3) Diffusion of water and formation of a salt-templated hole. As the annealing continues, gaseous water is expulsed to the atmosphere. Holes are formed due to the atmospheric

oxidation of graphene stemming from the presence of O_2, water and DNA triangles residue.

Our mechanism proposes that water is trapped under the CVD graphene during the transfer process (Step 1). While our mechanism has not yet been proven, the entrapment of water between graphene and a substrate has been studied.[181, 254] When the sample is annealed, the water in the gaseous phase creates separation between the DNA triangles and graphene (Step 2). Multiple reports have demonstrated the formation of graphene nanobubbles on the nanometer scale with high VDW forces and internal pressure.[255-258] It is possible that the water vapor along with the DNA residue promote the formation of the nanobubbles. Upon further annealing, the nanobubbles collapse, explaining why the DNA triangles are once again visible (Step 2). The height decrease observed is attributed to the decomposition of the DNA origami. As the annealing time increases, the DNA salt residue combined with the exposure of oxygen from air promotes the localized oxidation and formation of holes, in accordance to literature reports (Step 3).[250, 252]

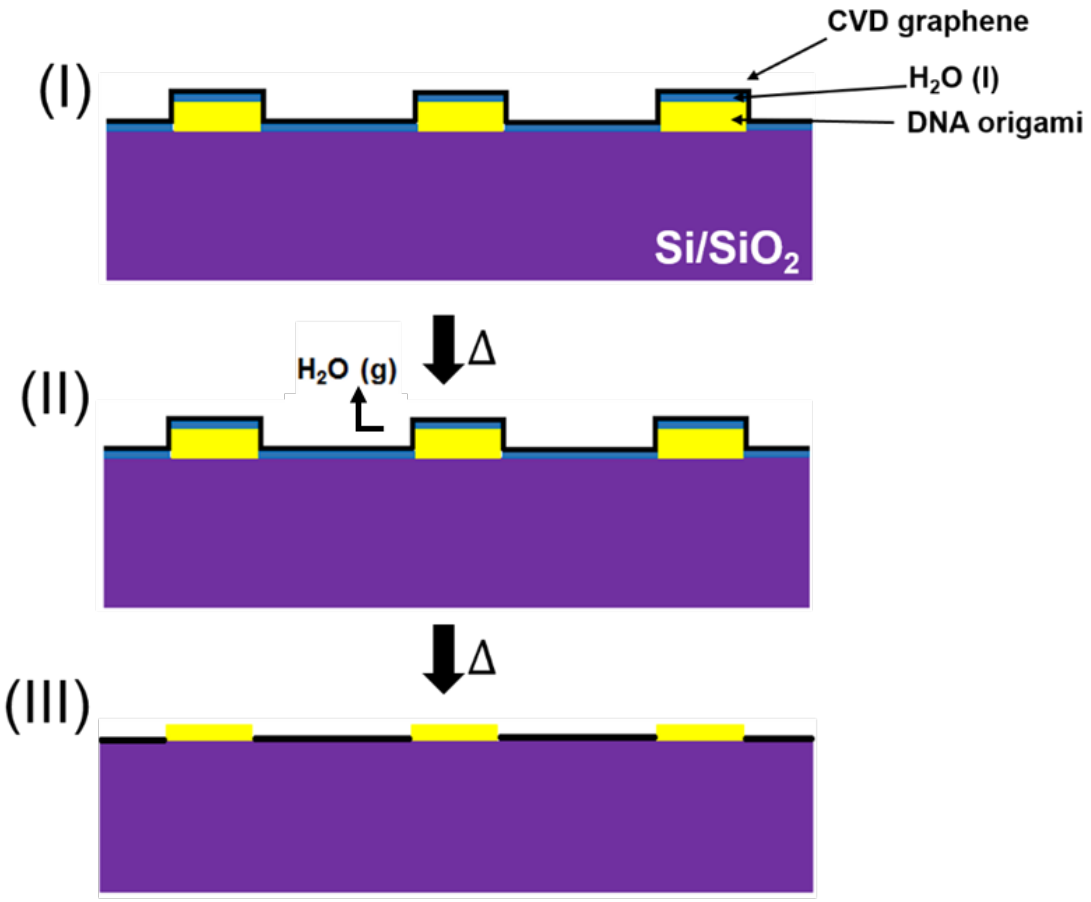

Figure 48. Schematic representation of the mechanism of the oxidation and patterning of graphene after thermal annealing (side view). (I) Before annealing. (II) Decomposition of DNA origami and oxidation of graphene. (III) Decomposition of DNA origami and formation of salt-templated holes.

4.4 CONCLUSION

In conclusion, we studied the encapsulation of DNA origami nanostructures by using CVD graphene as the encapsulating agent. The DNA origami was stable for at least two hours under graphene, a longer time when compared to the nanostructures directly exposed to air. We also determined several physical characteristics such as the optimal oxidation temperature and time for the process to occur. A site-specific oxidation of graphene with DNA origami as a template was observed. Furthermore, using a control experiment we were able to conclude that CVD graphene acts as a protective layer to the DNA triangles; the DNA triangle shape is preserved after several hours of thermal annealing. This discovery could be very helpful for future nanomaterial protection, for example, making the desired material more stable in ambient conditions.

5.0 CONCLUSION

My research aimed at studying the interaction of graphitic materials with hydrophilic components. I have shown a straightforward method to synthesize graphene without the aid of surfactants and organic solvents. In addition, my thesis also included detailed studies of the interfacial interaction of HOPG and CVD graphene with DNA origami nanostructures. Below, I've summarized the key observations, main conclusions and outlook of this dissertation.

5.1 SURFACTANT-FREE EXFOLIATION OF GRAPHITE

In chapter two, I reported the surfactant-free synthesis of few-layer graphene in an aqueous solution in a basic aqueous solution. The graphene flakes varied from 50 nm up to 2 μm in length and a height ranging from 5 to 10 nm. The graphene flakes are stabilized by electrostatic repulsion and are stable at room temperature for up to several months. Zeta potential of the graphene dispersion reflects that at pH = 11, the colloidal suspension is at its most stable state. Raman spectroscopy showed the characteristic bands of graphene, including a small defect peak that is due to the aggregation of smaller flakes to form a film. Control experiments suggest that interfacial accumulation of OH^- ions and naturally-occurring functional groups in graphite may contribute to the observed colloidal stability of graphene.

Regarding future work, it is important to quantify the amount of groups that decorate the exfoliated graphene. In order to do this, TGA measurements should be carried out. The decomposition of the labile oxygen-containing functional groups, should be observed. In order to use the exfoliated graphene for electronic applications, conductivities measurements must be carried out. A graphene film can be created and using a three-point probe the conductivity can be measured. While the conductivity value of the film will be lower when compared to CVD graphene, it should yield better values to the ones from exfoliated graphene using surfactants or organic solvents. Another application is the fabrication of graphene/polymer composites. Since the cost to produce surfactant-free graphene is low, the composite fabrication will be suitable for industrial applications.

5.2 DEPOSITION OF DNA ON HOPG

In chapter 3, I developed a method to successfully deposit DNA origami nanostructures on HOPG. No surface modification was needed to achieve the deposition. The triangles were stable for at least a week. The interaction between the DNA origami and the HOPG is possible due to structural rearrangement, exposing the DNA backbone to the HOPG surface. The density of the deposited DNA nanostructure on HOPG is roughly half of that on a Si/SiO_2 substrate. A useful application was found when the deposited DNA triangles promoted site-selective chemical vapor deposition growth of SiO_2.

It would be interesting to analyze the CVD deposition of other semiconductors such as TiO_2 with a suitable precursor to avoid the reactivity of TiO_2 with the step edges of HOPG. Additionally, the deposition of DNA origami without the aid of 1-pyrenemethylamine or doping

on graphene and other 2D materials should be studied. While a structural deformation may be observed, a new inexpensive method for patterning materials seems possible.

5.3 ENCAPSULATION OF DNA ORIGAMI USING CVD GRAPHENE

In chapter four, I reported that by using graphene as a protective layer, the stability of DNA origami triangles was enhanced. We were also able to observe and study the interaction between the nanostructures and CVD graphene that caused a site-specific oxidation, forming triangular-shaped holes where DNA triangles were present. Physical characteristics such as the optimal oxidation temperature, ideal time for the thermal annealing among other features were also studied.

The mechanism of the site-specific oxidation of graphene using DNA origami must be proven. In order to do this, a control experiment of the thermal annealing at 300 ˚C and 400 ˚C must be carried out with the encapsulation of magnesium phosphate. The oxidation of graphene without the encapsulation of the DNA triangles should be also performed to support of hypothesis that the DNA residue is responsible for the observed triangular holes. Our group reported a study of the structural stability of DNA origami under several chemical environments. It would be useful to perform similar experiments and compare the structural integrity of the DNA origami under graphene and outside on the same sample. The encapsulation of DNA origami with other 2D materials such as BN and MoS_2 can also be explored and analyze if a similar behavior is observed. Finally, the electrical properties of graphene can be controlled by the replication of DNA. Since the DNA may create localized defects, the band gap of graphene

could be opened for the application of temperature dependent electrical fuses or sensors for channel breaking.

5.4 FINAL REMARKS

In summary, my research provided new insight into the interaction between graphitic surfaces and its environment. These results could have significant implications to the understanding of the hydrophilic properties of graphene and its possible applications.

APPENDIX A

MECHANISM OF THE EXFOLIATION OF GRAPHITE

Sonochemistry is the application of ultrasound to chemical reactions and processes and arises from acoustic cavitation: the formation, growth, and implosive collapse of bubbles in a liquid.[259] Cavitation is a process in which mechanical activation destroys the attractive forces of molecules in the solid or liquid phase. The sonication of a liquid results in sonic cavitation that creates localized “hotspots” with effective temperatures of 5000 K and lifetimes on the order of a few nanoseconds or less.[260]

Liquid-phase exfoliation of graphite is commonly accompanied by external forces such as ultrasonication or shear mixing. Ultrasonic exfoliation is a suitable method to produce graphene in solution because mechanical forces, shear forces and cavitation are applied to drive graphite layer separation by destroying the van der Waals attraction forces between the adjacent layers. Furthermore, it is cheap and readily available. The intercalation and adsorption of hydroxide ions are important processes for the successful exfoliation of graphite to obtain single and few-layer graphene in solution without the aid of surfactants and organic solvents. It is relevant to understand the mechanism of ultrasound-assisted exfoliation because the optimization

of the exfoliation itself, a possible change in the chemical properties of graphene and the yield of graphene in solution can be studied.

For the promoting mechanism of ultrasonication to exfoliate graphite, the cavitation of bubbles generated by ultrasonication can accelerate the hydroxide groups in the aqueous solution introduce into natural graphite, shown in Figure 49. It can also reduce the van der Waals forces and expand the space between neighboring carbon sheets, which make the molecules to penetrate the interlayer space of graphite easily. Then, the shear forces supplied by sonication can separate the graphite flakes due to the breaking of interlayer van der Waals forces. Subsequently, graphene flakes stabilized by electrostatic repulsion are obtained.

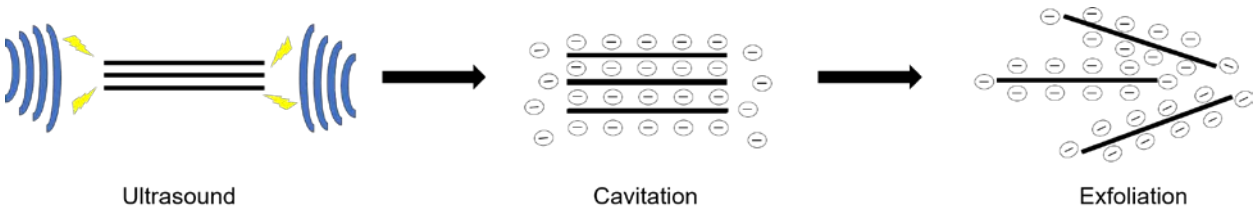

Figure 49. Schematic drawing of the exfoliation of graphite to obtain single and few layer graphene.

Because of the forces applied to graphite during the sonication step, we cannot rule out the possibility to damage of the basal plane or edges of graphene. Srivastava *et al.* reported the exfoliation of HOPG in deionized water without the aid of surfactants or organic solvents due to n-type doping and the adsorption of H^+ ions on the surface.[77] They proposed that the adsorption of hydronium ions will be attracted to defect centers from the sonication. However, Khan *et al.* demonstrated that the defects created during the sonication step are situated mostly on the edges, rather than on the graphene surface, leaving mostly intact the electronic properties of the material.[59] Generally, mild sonication of graphite for shorter time periods is regarded non-

destructive, as the process leaves the graphene basal plane relatively undamaged and the defects, if at all created would be principally located around the edges.[261]

To characterize the presence of disorders and defects in exfoliated graphene, several analytical characterization methods can be employed. Raman spectroscopy can be employed to assess the quality of graphene. If such defect exists, a D peak at around 1350 cm^{-1} should be present.[200] The vibrational modes of graphene and other functional groups can be also characterized using FT-IR. One can expect C=C peak in the frequency range of 1500 – 1600 cm^{-1}, corresponding to aromatic rings and C-H peaks of alkenes at 675 – 995 and 3010 – 3095 cm^{-1}. If the graphene is functionalized with oxide groups several peaks should be present such as the C-O from alcohols, ether and ester groups (1050 – 1300 cm^{-1}), C=O from carboxylic acids (1690 – 1760 cm^{-1}) and -OH from phenols (3200 – 3600 cm^{-1}).[195] Finally, an XPS spectrum could be beneficial to further confirm the presence of oxide groups. It is important to point out that contrary to FT-IR, XPS will not identify different functional groups. The C 1s peak should be present at approximately 184 eV and if oxides are present a 1s peak will be present at a range between 285 – 286 eV.[195]

BIBLIOGRAPHY

1. Chung, D. D. L. *Journal of Materials Science* **2002,** 37, (8), 1475-1489.
2. McCreery, R. L. *Chemical Reviews* **2008,** 108, (7), 2646-2687.
3. Borisov, A. M.; Mashkova, E. S.; Nemov, A. S.; Virgiliev, Y. S. *Nuclear Instruments & Methods in Physics Research Section B-Beam Interactions with Materials and Atoms* **2007,** 256, (1), 363-367.
4. Moore, A. W.; Ubbelohde, A. R.; Young, D. A. *Proceedings of the Royal Society of London Series a-Mathematical and Physical Sciences* **1964,** 280, (1380), 153-169.
5. Blackman, L. C.; Ubbelohde, A. R. *Proceedings of the Royal Society of London Series a-Mathematical and Physical Sciences* **1962,** 266, (1324), 20-32.
6. (Accessed January 2017).
7. (Accessed January 2017).
8. Chang, H. P.; Bard, A. J. *Langmuir* **1991,** 7, (6), 1143-1153.
9. Xiao, W. D.; Kushvaha, S. S.; Wang, X. S. *Journal of Physics-Condensed Matter* **2008,** 20, (22), 1-6.
10. Zhang, G. H.; Cuharuc, A. S.; Guell, A. G.; Unwin, P. R. *Physical Chemistry Chemical Physics* **2015,** 17, (17), 11827-11838.
11. Lai, S. C. S.; Patel, A. N.; McKelvey, K.; Unwin, P. R. *Angewandte Chemie-International Edition* **2012,** 51, (22), 5405-5408.
12. Patel, A. N.; Collignon, M. G.; O'Connell, M. A.; Hung, W. O. Y.; McKelvey, K.; Macpherson, J. V.; Unwin, P. R. *Journal of the American Chemical Society* **2012,** 134, (49), 20117-20130.
13. Patel, A. N.; McKelvey, K.; Unwin, P. R. *Journal of the American Chemical Society* **2012,** 134, (50), 20246-20249.
14. Doppner, T.; Neumayer, P.; Girard, F.; Kugland, N. L.; Landen, O. L.; Niemann, C.; Glenzer, S. H. *Review of Scientific Instruments* **2008,** 79, (10), 1-3.
15. Legall, H.; Stiel, H.; Arkadiev, V.; Bjeoumikhov, A. A. *Optics Express* **2006,** 14, (10), 4570-4576.
16. Falvo, M. R.; Superfine, R. *Journal of Nanoparticle Research* **2000,** 2, (3), 237-248.
17. Hugentobler, M.; Bonanni, S.; Sautier, A.; Harbich, W. *European Physical Journal D* **2011,** 63, (2), 215-220.
18. Shen, P. K.; Chi, N.; Chan, K. Y.; Phillips, D. L. *Applied Surface Science* **2001,** 172, (1-2), 159-166.
19. Song, Z.; Cai, T. H.; Hanson, J. C.; Rodriguez, J. A.; Hrbek, J. *Journal of the American Chemical Society* **2004,** 126, (27), 8576-8584.
20. Lopez-Salido, I.; Lim, D. C.; Kim, Y. D. *Surface Science* **2005,** 588, (1-3), 6-18.

21. Chen, L.; Yelon, A.; Sacher, E. *Journal of Physical Chemistry C* **2012,** 116, (12), 6902-6912.
22. Yang, S. J.; Tsai, P. C.; Kooij, E. S.; Prosperetti, A.; Zandvliet, H. J. W.; Lohse, D. *Langmuir* **2009,** 25, (3), 1466-1474.
23. Wang, X. Y.; Zhao, B. Y.; Ma, W. G.; Wang, Y.; Gao, X. Y.; Tai, R. Z.; Zhou, X. F.; Zhang, L. J. *Chemphyschem* **2015,** 16, (5), 1003-1007.
24. Schwabegger, G.; Oehzelt, M.; Salzmann, I.; Quochi, F.; Saba, M.; Mura, A.; Bongiovanni, G.; Vollmer, A.; Koch, N.; Sitter, H.; Simbrunner, C. *Langmuir* **2013,** 29, (47), 14444-14450.
25. Liu, Z. G.; Zhao, L.; Zhou, Z.; Sun, T. Z.; Zu, Y. G. *Scanning* **2012,** 34, (5), 302-308.
26. Brett, A. M. O.; Paquim, A. M. C. *Bioelectrochemistry* **2005,** 66, (1-2), 117-124.
27. Zhao, X. Q.; Huang, Y. S.; Yang, C. J.; Mao, B. W. *Science China-Chemistry* **2015,** 58, (12), 1858-1865.
28. Contera, S. A.; Iwasaki, H.; Suzuki, S. *Ultramicroscopy* **2003,** 97, (1-4), 65-72.
29. Frederix, P.; Bosshart, P. D.; Akiyama, T.; Chami, M.; Gullo, M. R.; Blackstock, J. J.; Dooleweerdt, K.; de Rooij, N. F.; Staufer, U.; Engel, A. *Nanotechnology* **2008,** 19, (38), 1-10.
30. Morcos, I. *Journal of Colloid and Interface Science* **1970,** 34, (3), 469-471.
31. Morcos, I. *Journal of Chemical Physics* **1972,** 57, (4), 1801-1802.
32. Wang, S. R.; Zhang, Y.; Abidi, N.; Cabrales, L. *Langmuir* **2009,** 25, (18), 11078-11081.
33. Yan, A. H.; Xiao, X. C.; Kulaots, I.; Sheldon, B. W.; Hurt, R. H. *Carbon* **2006,** 44, (14), 3116-3120.
34. Parobek, D.; Liu, H. T. *2d Materials* **2015,** 2, (3), 1-10.
35. Kozbial, A.; Li, Z. T.; Sun, J. N.; Gong, X.; Zhou, F.; Wang, Y. J.; Xu, H. C.; Liu, H. T.; Li, L. *Carbon* **2014,** 74, 218-225.
36. Li, Z. T.; Wang, Y. J.; Kozbial, A.; Shenoy, G.; Zhou, F.; McGinley, R.; Ireland, P.; Morganstein, B.; Kunkel, A.; Surwade, S. P.; Li, L.; Liu, H. T. *Nature Materials* **2013,** 12, (10), 925-931.
37. Westreich, P.; Fortier, H.; Flynn, S.; Foster, S.; Dahn, J. R. *Journal of Physical Chemistry C* **2007,** 111, (9), 3680-3684.
38. Kozbial, A.; Zhou, F.; Li, Z. T.; Liu, H. T.; Li, L. *Accounts of Chemical Research* **2016,** 49, (12), 2765-2773.
39. Warner, J. H.; Lee, G. D.; He, K.; Robertson, A. W.; Yoon, E.; Kirkland, A. I. *Acs Nano* **2013,** 7, (11), 9860-9866.
40. Geim, A. K.; Novoselov, K. S. *Nature Materials* **2007,** 6, (3), 183-191.
41. Boehm, H. P.; Setton, R.; Stumpp, E. *Carbon* **1986,** 24, (2), 241-245.
42. Boehm, H. P.; Setton, R.; Stumpp, E. *Pure and Applied Chemistry* **1994,** 66, (9), 1893-1901.
43. Novoselov, K. S.; Geim, A. K.; Morozov, S. V.; Jiang, D.; Zhang, Y.; Dubonos, S. V.; Grigorieva, I. V.; Firsov, A. A. *Science* **2004,** 306, (5696), 666-669.
44. Randviir, E. P.; Brownson, D. A. C.; Banks, C. E. *Materials Today* **2014,** 17, (9), 426-432.
45. Novoselov, K. S.; Jiang, Z.; Zhang, Y.; Morozov, S. V.; Stormer, H. L.; Zeitler, U.; Maan, J. C.; Boebinger, G. S.; Kim, P.; Geim, A. K. *Science* **2007,** 315, (5817), 1379-1379.
46. Bolotin, K. I.; Sikes, K. J.; Jiang, Z.; Klima, M.; Fudenberg, G.; Hone, J.; Kim, P.; Stormer, H. L. *Solid State Communications* **2008,** 146, (9-10), 351-355.

47. Balandin, A. A.; Ghosh, S.; Bao, W. Z.; Calizo, I.; Teweldebrhan, D.; Miao, F.; Lau, C. N. *Nano Letters* **2008,** 8, (3), 902-907.
48. Nair, R. R.; Blake, P.; Grigorenko, A. N.; Novoselov, K. S.; Booth, T. J.; Stauber, T.; Peres, N. M. R.; Geim, A. K. *Science* **2008,** 320, (5881), 1308-1308.
49. Lee, C.; Wei, X. D.; Kysar, J. W.; Hone, J. *Science* **2008,** 321, (5887), 385-388.
50. Lee, J. U.; Yoon, D.; Cheong, H. *Nano Letters* **2012,** 12, (9), 4444-4448.
51. Mishra, N.; Boeckl, J.; Motta, N.; Iacopi, F. *Physica Status Solidi a-Applications and Materials Science* **2016,** 213, (9), 2277-2289.
52. Jiao, L. Y.; Zhang, L.; Wang, X. R.; Diankov, G.; Dai, H. J. *Nature* **2009,** 458, (7240), 877-880.
53. Park, S.; Ruoff, R. S. *Nat Nano* **2009,** 4, (4), 217-224.
54. Hummers, W. S.; Offeman, R. E. *J. Am. Chem. Soc.* **1958,** 80, (6), 1339-1339.
55. Stankovich, S.; Piner, R. D.; Chen, X. Q.; Wu, N. Q.; Nguyen, S. T.; Ruoff, R. S. *J. Mater. Chem.* **2006,** 16, (2), 155-158.
56. Stankovich, S.; Dikin, D. A.; Piner, R. D.; Kohlhaas, K. A.; Kleinhammes, A.; Jia, Y.; Wu, Y.; Nguyen, S. T.; Ruoff, R. S. *Carbon* **2007,** 45, (7), 1558-1565.
57. Li, D.; Muller, M. B.; Gilje, S.; Kaner, R. B.; Wallace, G. G. *Nat. Nanotechnol.* **2008,** 3, (2), 101-105.
58. Hernandez, Y.; Nicolosi, V.; Lotya, M.; Blighe, F. M.; Sun, Z. Y.; De, S.; McGovern, I. T.; Holland, B.; Byrne, M.; Gun'ko, Y. K.; Boland, J. J.; Niraj, P.; Duesberg, G.; Krishnamurthy, S.; Goodhue, R.; Hutchison, J.; Scardaci, V.; Ferrari, A. C.; Coleman, J. N. *Nature Nanotechnology* **2008,** 3, (9), 563-568.
59. Khan, U.; O'Neill, A.; Lotya, M.; De, S.; Coleman, J. N. *Small* **2010,** 6, (7), 864-871.
60. Khan, U.; Porwal, H.; O'Neill, A.; Nawaz, K.; May, P.; Coleman, J. N. *Langmuir* **2011,** 27, (15), 9077-9082.
61. Bourlinos, A. B.; Georgakilas, V.; Zboril, R.; Steriotis, T. A.; Stubos, A. K. *Small* **2009,** 5, (16), 1841-1845.
62. Hamilton, C. E.; Lomeda, J. R.; Sun, Z. Z.; Tour, J. M.; Barron, A. R. *Nano Letters* **2009,** 9, (10), 3460-3462.
63. Niu, L. Y.; Coleman, J. N.; Zhang, H.; Shin, H.; Chhowalla, M.; Zheng, Z. J. *Small* **2016,** 12, (3), 272-293.
64. Choi, E. Y.; Choi, W. S.; Lee, Y. B.; Noh, Y. Y. *Nanotechnology* **2011,** 22, (36), 1-6.
65. Qian, W.; Hao, R.; Hou, Y. L.; Tian, Y.; Shen, C. M.; Gao, H. J.; Liang, X. L. *Nano Research* **2009,** 2, (9), 706-712.
66. Zhang, X. Y.; Coleman, A. C.; Katsonis, N.; Browne, W. R.; van Wees, B. J.; Feringa, B. L. *Chemical Communications* **2010,** 46, (40), 7539-7541.
67. Lotya, M.; Hernandez, Y.; King, P. J.; Smith, R. J.; Nicolosi, V.; Karlsson, L. S.; Blighe, F. M.; De, S.; Wang, Z. M.; McGovern, I. T.; Duesberg, G. S.; Coleman, J. N. *Journal of the American Chemical Society* **2009,** 131, (10), 3611-3620.
68. Hao, R.; Qian, W.; Zhang, L. H.; Hou, Y. L. *Chemical Communications* **2008**, (48), 6576-6578.
69. Lotya, M.; King, P. J.; Khan, U.; De, S.; Coleman, J. N. *Acs Nano* **2010,** 4, (6), 3155-3162.
70. Green, A. A.; Hersam, M. C. *Nano Letters* **2009,** 9, (12), 4031-4036.
71. Vadukumpully, S.; Paul, J.; Valiyaveettil, S. *Carbon* **2009,** 47, (14), 3288-3294.

72. Guardia, L.; Fernandez-Merino, M. J.; Paredes, J. I.; Solis-Fernandez, P.; Villar-Rodil, S.; Martinez-Alonso, A.; Tascon, J. M. D. *Carbon* **2011,** 49, (5), 1653-1662.
73. Ricardo, K. B.; Sendecki, A.; Liu, H. T. *Chemical Communications* **2014,** 50, (21), 2751-2754.
74. Englert, J. M.; Rohrl, J.; Schmidt, C. D.; Graupner, R.; Hundhausen, M.; Hauke, F.; Hirsch, A. *Advanced Materials* **2009,** 21, (42), 4265-4269.
75. Paton, K. R.; Varrla, E.; Backes, C.; Smith, R. J.; Khan, U.; O'Neill, A.; Boland, C.; Lotya, M.; Istrate, O. M.; King, P.; Higgins, T.; Barwich, S.; May, P.; Puczkarski, P.; Ahmed, I.; Moebius, M.; Pettersson, H.; Long, E.; Coelho, J.; O'Brien, S. E.; McGuire, E. K.; Sanchez, B. M.; Duesberg, G. S.; McEvoy, N.; Pennycook, T. J.; Downing, C.; Crossley, A.; Nicolosi, V.; Coleman, J. N. *Nature Materials* **2014,** 13, (6), 624-630.
76. He, P.; Zhou, C.; Tian, S. Y.; Sun, J.; Yang, S. W.; Ding, G. Q.; Xie, X. M.; Jiang, M. H. *Chemical Communications* **2015,** 51, (22), 4651-4654.
77. Srivastava, P. K.; Yadav, P.; Ghosh, S. *Nanoscale* **2016,** 8, (34), 15702-15711.
78. Bourlinos, A. B.; Georgakilas, V.; Zboril, R.; Steriotis, T. A.; Stubos, A. K.; Trapalis, C. *Solid State Communications* **2009,** 149, (47-48), 2172-2176.
79. Dong, X. C.; Shi, Y. M.; Zhao, Y.; Chen, D. M.; Ye, J.; Yao, Y. G.; Gao, F.; Ni, Z. H.; Yu, T.; Shen, Z. X.; Huang, Y. X.; Chen, P.; Li, L. J. *Physical Review Letters* **2009,** 102, (13), 1335501-1-1335501-4.
80. Wang, X. Q.; Fulvio, P. F.; Baker, G. A.; Veith, G. M.; Unocic, R. R.; Mahurin, S. M.; Chi, M. F.; Dai, S. *Chemical Communications* **2010,** 46, (25), 4487-4489.
81. Nuvoli, D.; Valentini, L.; Alzari, V.; Scognamillo, S.; Bon, S. B.; Piccinini, M.; Illescas, J.; Mariani, A. *Journal of Materials Chemistry* **2011,** 21, (10), 3428-3431.
82. Parvez, K.; Li, R. J.; Puniredd, S. R.; Hernandez, Y.; Hinkel, F.; Wang, S. H.; Feng, X. L.; Mullen, K. *Acs Nano* **2013,** 7, (4), 3598-3606.
83. Su, C. Y.; Lu, A. Y.; Xu, Y. P.; Chen, F. R.; Khlobystov, A. N.; Li, L. J. *Acs Nano* **2011,** 5, (3), 2332-2339.
84. Chia, J. S. Y.; Tan, M. T. T.; Khiew, P. S.; Chin, J. K.; Siong, C. W. *Science of Advanced Materials* **2016,** 8, (6), 1177-1186.
85. Banerjee, B. C.; Walker, P. L.; Hirt, T. J. *Nature* **1961,** 192, (480), 450-451.
86. Li, X. S.; Cai, W. W.; An, J. H.; Kim, S.; Nah, J.; Yang, D. X.; Piner, R.; Velamakanni, A.; Jung, I.; Tutuc, E.; Banerjee, S. K.; Colombo, L.; Ruoff, R. S. *Science* **2009,** 324, (5932), 1312-1314.
87. Bae, S.; Kim, H.; Lee, Y.; Xu, X. F.; Park, J. S.; Zheng, Y.; Balakrishnan, J.; Lei, T.; Kim, H. R.; Song, Y. I.; Kim, Y. J.; Kim, K. S.; Ozyilmaz, B.; Ahn, J. H.; Hong, B. H.; Iijima, S. *Nature Nanotechnology* **2010,** 5, (8), 574-578.
88. Liu, J. B.; Li, P. J.; Chen, Y. F.; Wang, Z. G.; He, J. R.; Tian, H. J.; Qi, F.; Zheng, B. J.; Zhou, J. H.; Lin, W.; Zhang, W. L. *Journal of Alloys and Compounds* **2014,** 615, 415-418.
89. Li, X. S.; Colombo, L.; Ruoff, R. S. *Advanced Materials* **2016,** 28, (29), 6247-6252.
90. Li, X. S.; Zhu, Y. W.; Cai, W. W.; Borysiak, M.; Han, B. Y.; Chen, D.; Piner, R. D.; Colombo, L.; Ruoff, R. S. *Nano Letters* **2009,** 9, (12), 4359-4363.
91. Li, X. S.; Magnuson, C. W.; Venugopal, A.; An, J. H.; Suk, J. W.; Han, B. Y.; Borysiak, M.; Cai, W. W.; Velamakanni, A.; Zhu, Y. W.; Fu, L. F.; Vogel, E. M.; Voelkl, E.; Colombo, L.; Ruoff, R. S. *Nano Letters* **2010,** 10, (11), 4328-4334.
92. Wofford, J. M.; Nie, S.; McCarty, K. F.; Bartelt, N. C.; Dubon, O. D. *Nano Letters* **2010,** 10, (12), 4890-4896.

93. Kim, M. S.; Woo, J. M.; Geum, D. M.; Rani, J. R.; Jang, J. H. *Aip Advances* **2014,** 4, (12).
94. Mattevi, C.; Kim, H.; Chhowalla, M. *Journal of Materials Chemistry* **2011,** 21, (10), 3324-3334.
95. Watson, J. D.; Crick, F. H. C. *Nature* **1953,** 171, (4356), 737-738.
96. Berg, J. M.; Tymoczko, J. L.; Gatto, G. J.; Stryer, L., *Biochemistry*. W. H. Freeman: 2015.
97. Seeman, N. C.; Lukeman, P. S. *Reports on Progress in Physics* **2005,** 68, (1), 237-270.
98. Seeman, N. C. *J. Theor. Biol.* **1982,** 99, (2), 237-247.
99. Aldaye, F. A.; Palmer, A. L.; Sleiman, H. F. *Science* **2008,** 321, (5897), 1795-1799.
100. Li, H. Y.; Carter, J. D.; LaBean, T. H. *Materials Today* **2009,** 12, (5), 24-32.
101. Kuzuya, A.; Komiyama, M. *Nanoscale* **2010,** 2, (3), 310-322.
102. Seeman, N. C., Nanomaterials Based on DNA. In *Annual Review of Biochemistry, Vol 79*, Kornberg, R. D.; Raetz, C. R. H.; Rothman, J. E.; Thorner, J. W., Eds. 2010; Vol. 79, pp 65-87.
103. Pinheiro, A. V.; Han, D. R.; Shih, W. M.; Yan, H. *Nature Nanotechnology* **2011,** 6, (12), 763-772.
104. Zadegan, R. M.; Norton, M. L. *International Journal of Molecular Sciences* **2012,** 13, (6), 7149-7162.
105. Zhang, F.; Nangreave, J.; Liu, Y.; Yan, H. *Journal of the American Chemical Society* **2014,** 136, (32), 11198-11211.
106. Mathur, D.; Medintz, I. L. *Analytical Chemistry* **2017,** 89, (5), 2646-2663.
107. Fu, T. J.; Tsedinh, Y. C.; Seeman, N. C. *Journal of Molecular Biology* **1994,** 236, (1), 91-105.
108. Li, H. Y.; LaBean, T. H.; Leong, K. W. *Interface Focus* **2011,** 1, (5), 702-724.
109. Fu, T. J.; Seeman, N. C. *Biochemistry* **1993,** 32, (13), 3211-3220.
110. Yin, P.; Hariadi, R. F.; Sahu, S.; Choi, H. M. T.; Park, S. H.; LaBean, T. H.; Reif, J. H. *Science* **2008,** 321, (5890), 824-826.
111. Rothemund, P. W. K.; Ekani-Nkodo, A.; Papadakis, N.; Kumar, A.; Fygenson, D. K.; Winfree, E. *Journal of the American Chemical Society* **2004,** 126, (50), 16344-16352.
112. Liu, W. Y.; Zhong, H.; Wang, R. S.; Seeman, N. C. *Angewandte Chemie-International Edition* **2011,** 50, (1), 264-267.
113. Winfree, E.; Liu, F. R.; Wenzler, L. A.; Seeman, N. C. *Nature* **1998,** 394, (6693), 539-544.
114. He, Y.; Chen, Y.; Liu, H. P.; Ribbe, A. E.; Mao, C. D. *Journal of the American Chemical Society* **2005,** 127, (35), 12202-12203.
115. Wei, B.; Dai, M. J.; Yin, P. *Nature* **2012,** 485, (7400), 623-626.
116. Chen, J. H.; Seeman, N. C. *Nature* **1991,** 350, (6319), 631-633.
117. Li, Z.; Wei, B.; Nangreave, J.; Lin, C. X.; Liu, Y.; Mi, Y. L.; Yan, H. *Journal of the American Chemical Society* **2009,** 131, (36), 13093-13098.
118. Zhang, Y. W.; Seeman, N. C. *Journal of the American Chemical Society* **1994,** 116, (5), 1661-1669.
119. Shih, W. M.; Quispe, J. D.; Joyce, G. F. *Nature* **2004,** 427, (6975), 618-621.
120. He, Y.; Ye, T.; Su, M.; Zhang, C.; Ribbe, A. E.; Jiang, W.; Mao, C. D. *Nature* **2008,** 452, (7184), 198-U41.

121. Zheng, J. P.; Birktoft, J. J.; Chen, Y.; Wang, T.; Sha, R. J.; Constantinou, P. E.; Ginell, S. L.; Mao, C. D.; Seeman, N. C. *Nature* **2009,** 461, (7260), 74-77.
122. Rothemund, P. W. K. *Nature* **2006,** 440, (7082), 297-302.
123. Douglas, S. M.; Marblestone, A. H.; Teerapittayanon, S.; Vazquez, A.; Church, G. M.; Shih, W. M. *Nucleic Acids Research* **2009,** 37, (15), 5001-5006.
124. Andersen, E. S.; Dong, M. D.; Nielsen, M. M.; Jahn, K.; Lind-Thomsen, A.; Mamdouh, W.; Gothelf, K. V.; Besenbacher, F.; Kjems, J. *Acs Nano* **2008,** 2, (6), 1213-1218.
125. Zhang, H. L.; Chao, J.; Pan, D.; Liu, H. J.; Huang, Q.; Fan, C. H. *Chemical Communications* **2012,** 48, (51), 6405-6407.
126. Zhao, Z.; Liu, Y.; Yan, H. *Nano Letters* **2011,** 11, (7), 2997-3002.
127. Ke, Y. G.; Sharma, J.; Liu, M. H.; Jahn, K.; Liu, Y.; Yan, H. *Nano Letters* **2009,** 9, (6), 2445-2447.
128. Han, D. R.; Pal, S.; Nangreave, J.; Deng, Z. T.; Liu, Y.; Yan, H. *Science* **2011,** 332, (6027), 342-346.
129. Douglas, S. M.; Dietz, H.; Liedl, T.; Hogberg, B.; Graf, F.; Shih, W. M. *Nature* **2009,** 459, (7245), 414-418.
130. Dietz, H.; Douglas, S. M.; Shih, W. M. *Science* **2009,** 325, (5941), 725-730.
131. Andersen, E. S.; Dong, M.; Nielsen, M. M.; Jahn, K.; Subramani, R.; Mamdouh, W.; Golas, M. M.; Sander, B.; Stark, H.; Oliveira, C. L. P.; Pedersen, J. S.; Birkedal, V.; Besenbacher, F.; Gothelf, K. V.; Kjems, J. *Nature* **2009,** 459, (7243), 73-76.
132. Han, D. R.; Pal, S.; Liu, Y.; Yan, H. *Nature Nanotechnology* **2010,** 5, (10), 712-717.
133. Pal, S.; Deng, Z. T.; Ding, B. Q.; Yan, H.; Liu, Y. *Angewandte Chemie-International Edition* **2010,** 49, (15), 2700-2704.
134. Ding, B. Q.; Deng, Z. T.; Yan, H.; Cabrini, S.; Zuckermann, R. N.; Bokor, J. *Journal of the American Chemical Society* **2010,** 132, (10), 3248–3249.
135. Maune, H. T.; Han, S. P.; Barish, R. D.; Bockrath, M.; Goddard, W. A.; Rothemund, P. W. K.; Winfree, E. *Nature Nanotechnology* **2010,** 5, (1), 61-66.
136. Sacca, B.; Meyer, R.; Erkelenz, M.; Kiko, K.; Arndt, A.; Schroeder, H.; Rabe, K. S.; Niemeyer, C. M. *Angewandte Chemie-International Edition* **2010,** 49, (49), 9378-9383.
137. Kuzyk, A.; Laitinen, K. T.; Torma, P. *Nanotechnology* **2009,** 20, (23), 1-5.
138. Zhang, G. M.; Surwade, S. P.; Zhou, F.; Liu, H. T. *Chemical Society Reviews* **2013,** 42, (7), 2488-2496.
139. Peng, Z. B.; Liu, H. T. *Chemistry of Materials* **2016,** 28, (4), 1012-1021.
140. Hong, F.; Zhang, F.; Liu, Y.; Yan, H. *Chemical Reviews* **2017**.
141. Surwade, S. P.; Zhou, F.; Wei, B.; Sun, W.; Powell, A.; O'Donnell, C.; Yin, P.; Liu, H. T. *Journal of the American Chemical Society* **2013,** 135, (18), 6778-6781.
142. Gopinath, A.; Rothemund, P. W. K. *Acs Nano* **2014,** 8, (12), 12030-12040.
143. Tian, C.; Kim, H.; Sun, W.; Kim, Y.; Yin, P.; Liu, H. T. *Acs Nano* **2017,** 11, (1), 227-238.
144. Diagne, C. T.; Brun, C.; Gasparutto, D.; Baillin, X.; Tiron, R. *Acs Nano* **2016,** 10, (7), 6458-6463.
145. Kuzuya, A.; Sakai, Y.; Yamazaki, T.; Xu, Y.; Komiyama, M. *Nature Communications* **2011,** 2, 1-8.
146. Ke, Y. G.; Lindsay, S.; Chang, Y.; Liu, Y.; Yan, H. *Science* **2008,** 319, (5860), 180-183.
147. Bell, N. A. W.; Keyser, U. F. *Febs Letters* **2014,** 588, (19), 3564-3570.

148. Zhao, Y. X.; Shaw, A.; Zeng, X. H.; Benson, E.; Nystrom, A. M.; Hogberg, B. *Acs Nano* **2012,** 6, (10), 8684-8691.
149. Jiang, Q.; Song, C.; Nangreave, J.; Liu, X. W.; Lin, L.; Qiu, D. L.; Wang, Z. G.; Zou, G. Z.; Liang, X. J.; Yan, H.; Ding, B. Q. *Journal of the American Chemical Society* **2012,** 134, (32), 13396-13403.
150. Douglas, S. M.; Bachelet, I.; Church, G. M. *Science* **2012,** 335, (6070), 831-834.
151. Kim, H.; Surwade, S. P.; Powell, A.; O'Donnell, C.; Liu, H. T. *Chemistry of Materials* **2014,** 26, (18), 5265-5273.
152. Ramakrishnan, S.; Krainer, G.; Grundmeier, G.; Schlierf, M.; Keller, A. *Nanoscale* **2016,** 8, (19), 10398-10405.
153. Rajendran, A.; Endo, M.; Katsuda, Y.; Hidaka, K.; Sugiyama, H. *Journal of the American Chemical Society* **2011,** 133, (37), 14488-14491.
154. Wang, P. F.; Meyer, T. A.; Pan, V.; Dutta, P. K.; Ke, Y. G. *Chem* **2017,** 2, (3), 359-382.
155. Martin, T. G.; Dietz, H. *Nature Communications* **2012,** 3, 1-6.
156. Castro, C. E.; Kilchherr, F.; Kim, D. N.; Shiao, E. L.; Wauer, T.; Wortmann, P.; Bathe, M.; Dietz, H. *Nature Methods* **2011,** 8, (3), 221-229.
157. Kershner, R. J.; Bozano, L. D.; Micheel, C. M.; Hung, A. M.; Fornof, A. R.; Cha, J. N.; Rettner, C. T.; Bersani, M.; Frommer, J.; Rothemund, P. W. K.; Wallraff, G. M. *Nature Nanotechnology* **2009,** 4, (9), 557-561.
158. Brett, A. M. O.; Chiorcea, A. M. *Langmuir* **2003,** 19, (9), 3830-3839.
159. Brett, A. M. O.; Chiorcea, A. M. *Electrochemistry Communications* **2003,** 5, (2), 178-183.
160. Doi, K.; Takeuchi, H.; Nii, R.; Akamatsu, S.; Kakizaki, T.; Kawano, S. *Journal of Chemical Physics* **2013,** 139, (8), 085102-1-085102-9.
161. Liu, Z. G.; Zhao, L.; Zu, Y. G.; Tan, S. N.; Wang, Y. L.; Zhang, Y. M. *Microscopy and Microanalysis* **2013,** 19, (3), 544-552.
162. Jiang, X. H.; Lin, X. Q. *Electrochemistry Communications* **2004,** 6, (9), 873-879.
163. Yamamoto, I.; Kanno, T.; Tanaka, H.; Kawai, T. *Japanese Journal of Applied Physics Part 2-Letters* **2003,** 42, (5B), L559-L560.
164. Zhao, L.; Liu, Z. G.; Zu, Y. G.; Zhou, Z.; Sun, T. Z. *Scanning* **2012,** 34, (1), 68-75.
165. Wang, H. B.; An, H. J.; Zhang, F.; Zhang, Z. X.; Ye, M.; Xiu, P.; Zhang, Y.; Hu, J. *Journal of Vacuum Science & Technology B* **2008,** 26, (5), L41-L44.
166. Wang, H. B.; Wang, X. Y.; Li, H. B.; Zhang, X. H.; Zhang, Y.; Hu, J. *Langmuir* **2011,** 27, (6), 2405-2410.
167. Adamcik, J.; Tobenas, S.; Di Santo, G.; Klinov, D.; Dietler, G. *Langmuir* **2009,** 25, (5), 3159-3162.
168. Dubrovin, E. V.; Schachtele, M.; Schaffer, T. E. *Rsc Advances* **2016,** 6, (83), 79584-79592.
169. Dubrovin, E. V.; Speller, S.; Yaminsky, I. V. *Langmuir* **2014,** 30, (51), 15423-15432.
170. Dubrovin, E. V.; Gerritsen, J. W.; Zivkovic, J.; Yaminsky, I. V.; Speller, S. *Colloids and Surfaces B-Biointerfaces* **2010,** 76, (1), 63-69.
171. Husale, S.; Sahoo, S.; Radenovic, A.; Traversi, F.; Annibale, P.; Kis, A. *Langmuir* **2010,** 26, (23), 18078-18082.
172. Tang, L. H.; Wang, Y.; Li, J. H. *Chemical Society Reviews* **2015,** 44, (19), 6954-6980.
173. Campos, R.; Zhang, S.; Majikes, J. M.; Ferraz, L. C. C.; LaBean, T. H.; Dong, M. D.; Ferapontova, E. E. *Chemical Communications* **2015,** 51, (74), 14111-14114.

174. Ricardo, K. B. X., A.; Salim, M.; Zhou, F.; Liu, H. *Langmuir* **2017,** 33, (16), 3991-3997.
175. Rahman, M.; Neff, D.; Green, N.; Norton, M. L. *Nanomaterials* **2016,** 6, (11), 1-13.
176. Green, N. S.; Norton, M. L. *Analytica Chimica Acta* **2015,** 853, 127-142.
177. Mudedla, S. K.; Balamurugan, K.; Kamaraj, M.; Subramanian, V. *Physical Chemistry Chemical Physics* **2016,** 18, (1), 295-309.
178. Yun, J. M.; Kim, K. N.; Kim, J. Y.; Shin, D. O.; Lee, W. J.; Lee, S. H.; Lieberman, M.; Kim, S. O. *Angewandte Chemie-International Edition* **2012,** 51, (4), 912-915.
179. Jin, Z.; Sun, W.; Ke, Y.; Shih, C.-J.; Paulus, G. L. C.; Wang, Q. H.; Mu, B.; Yin, P.; Strano, M. S. *Nature Communications* **2013,** 4.
180. Cao, P. G.; Xu, K.; Varghese, J. O.; Heath, J. R. *Nano Letters* **2011,** 11, (12), 5581-5586.
181. Xu, K.; Cao, P. G.; Heath, J. R. *Science* **2010,** 329, (5996), 1188-1191.
182. Severin, N.; Lange, P.; Sokolov, I. M.; Rabe, J. P. *Nano Letters* **2012,** 12, (2), 774-779.
183. Moon, Y.; Shin, J.; Seo, S.; Park, J.; Dugasani, S. R.; Woo, S. H.; Park, T.; Park, S. H.; Ahn, J. R. *Applied Physics Letters* **2014,** 104, (23).
184. Severin, N.; Dorn, M.; Kalachev, A.; Rabe, J. P. *Nano Letters* **2011,** 11, (6), 2436-2439.
185. Matkovic, A.; Vasic, B.; Pesic, J.; Prinz, J.; Bald, I.; Milosavljevic, A. R.; Gajic, R. *New Journal of Physics* **2016,** 18.
186. Myung, S.; Solanki, A.; Kim, C.; Park, J.; Kim, K. S.; Lee, K. B. *Advanced Materials* **2011,** 23, (19), 2221-2225.
187. Mohanty, N.; Fahrenholtz, M.; Nagaraja, A.; Boyle, D.; Berry, V. *Nano Letters* **2011,** 11, (3), 1270-1275.
188. Kempaiah, R.; Salgado, S.; Chung, W. L.; Maheshwari, V. *Chemical Communications* **2011,** 47, (41), 11480-11482.
189. Liu, Q.; Shi, J. B.; Cheng, M. T.; Li, G. L.; Cao, D.; Jiang, G. B. *Chemical Communications* **2012,** 48, (13), 1874-1876.
190. Dill, K.; Bromberg, S., *Molecular Driving Forces: Statistical Thermodynamics in Biology, Chemistry, Physics, and Nanoscience*. Taylor & Francis Group: 2010.
191. Instruments, M.
192. Binnig, G. K. *Physica Scripta* **1987,** T19A, 53-54.
193. Klinov, D.; Magonov, S. *Applied Physics Letters* **2004,** 84, (14), 2697-2699.
194. Lauritsen, J. V.; Reichling, M. *Journal of Physics-Condensed Matter* **2010,** 22, (26).
195. Skoog, D. A.; Crouch, S. R.; Holler, F. J., *Principles of instrumental analysis*. Thomson Brooks/Cole: Belmont, CA, 2007.
196. Ferrari, A. C. *Solid State Communications* **2007,** 143, (1-2), 47-57.
197. Ferrari, A. C.; Meyer, J. C.; Scardaci, V.; Casiraghi, C.; Lazzeri, M.; Mauri, F.; Piscanec, S.; Jiang, D.; Novoselov, K. S.; Roth, S.; Geim, A. K. *Physical Review Letters* **2006,** 97, (18), 187401-1-187401-4.
198. Wang, Y. Y.; Ni, Z. H.; Shen, Z. X.; Wang, H. M.; Wu, Y. H. *Applied Physics Letters* **2008,** 92, (4).
199. Casiraghi, C.; Hartschuh, A.; Qian, H.; Piscanec, S.; Georgi, C.; Fasoli, A.; Novoselov, K. S.; Basko, D. M.; Ferrari, A. C. *Nano Lett.* **2009,** 9, (4), 1433-1441.
200. Malard, L. M.; Pimenta, M. A.; Dresselhaus, G.; Dresselhaus, M. S. *Physics Reports-Review Section of Physics Letters* **2009,** 473, (5-6), 51-87.
201. Bhattacharjee, S. *Journal of Controlled Release* **2016,** 235, 337-351.

202. Blake, P.; Brimicombe, P. D.; Nair, R. R.; Booth, T. J.; Jiang, D.; Schedin, F.; Ponomarenko, L. A.; Morozov, S. V.; Gleeson, H. F.; Hill, E. W.; Geim, A. K.; Novoselov, K. S. *Nano Lett.* **2008,** 8, (6), 1704-1708.
203. De, S.; Coleman, J. N. *Acs Nano* **2010,** 4, (5), 2713-2720.
204. Zhang, B.; Yu, B.; Zhou, F.; Liu, W. *Journal of Materials Chemistry A* **2013,** 1, (30), 8587-8592.
205. Nicolosi, V.; Chhowalla, M.; Kanatzidis, M. G.; Strano, M. S.; Coleman, J. N. *Science* **2013,** 340, (6139), 1420-1441.
206. Ciesielski, A.; Samori, P. *Chemical Society Reviews* **2014,** 43, (1), 381-398.
207. O'Neill, A.; Khan, U.; Nirmalraj, P. N.; Boland, J.; Coleman, J. N. *Journal of Physical Chemistry C* **2011,** 115, (13), 5422-5428.
208. Choi, E. Y.; Choi, W. S.; Lee, Y. B.; Noh, Y. Y. *Nanotechnology* **2011,** 22, (36), 365601
209. Marcano, D. C.; Kosynkin, D. V.; Berlin, J. M.; Sinitskii, A.; Sun, Z. Z.; Slesarev, A.; Alemany, L. B.; Lu, W.; Tour, J. M. *Acs Nano* **2010,** 4, (8), 4806-4814.
210. Choi, E. K.; Jeon, I. Y.; Bae, S. Y.; Lee, H. J.; Shin, H. S.; Dai, L. M.; Baek, J. B. *Chem. Commun.* **2010,** 46, (34), 6320-6322.
211. Liu, W. W.; Wang, J. N. *Chem. Commun.* **2011,** 47, (24), 6888-6890.
212. Beattie, J. K.; Djerdjev, A. M. *Angewandte Chemie-International Edition* **2004,** 43, (27), 3568-3571.
213. Zimmermann, R.; Freudenberg, U.; Schweiss, R.; Kuettner, D.; Werner, C. *Current Opinion in Colloid & Interface Science* **2010,** 15, (3), 196-202.
214. Liu, H. T.; Steigerwald, M. L.; Nuckolls, C. *J. Am. Chem. Soc.* **2009,** 131, (47), 17034-+.
215. Xiang, G.; Long, Y.; He, J.; Xu, B.; Liu, H.; Wang, X. *Langmuir* **2014**.
216. Roger, K.; Cabane, B. *Angewandte Chemie-International Edition* **2012,** 51, (23), 5625-5628.
217. Beattie, J. K.; Gray-Weale, A. *Angewandte Chemie-International Edition* **2012,** 51, (52), 12941-12942.
218. Roger, K.; Cabane, B. *Angewandte Chemie-International Edition* **2012,** 51, (52), 12943-12945.
219. Jena, K. C.; Scheu, R.; Roke, S. *Angew. Chem.* **2012,** 124, (52), 13112-13114.
220. Barton, S. S.; Harrison, B. H. *Carbon* **1975,** 13, (4), 283-288.
221. Gu, H.; Chao, J.; Xiao, S.-J.; Seeman, N. C. *Nature Nanotechnology* **2009,** 4, (4), 245-248.
222. Zhang, X.; Hu, H. *Central European Journal of Chemistry* **2014,** 12, (10), 977-993.
223. McCreery, R. L.; McDermott, M. T. *Analytical Chemistry* **2012,** 84, (5), 2602-2605.
224. Ashraf, A.; Wu, Y. B.; Wang, M. C.; Aluru, N. R.; Dastgheib, S. A.; Nam, S. *Langmuir* **2014,** 30, (43), 12827-12836.
225. Kwon, S.; Vidic, R.; Borguet, E. *Carbon* **2002,** 40, (13), 2351-2358.
226. Martinez-Martinez, D.; Kolodziejczyk, L.; Sanchez-Lopez, J. C.; Fernandez, A. *Surface Science* **2009,** 603, (7), 973-979.
227. Diculescu, V. C.; Paquim, A. M. C.; Brett, A. M. O. *Sensors* **2005,** 5, (6-10), 377-393.
228. Chiorcea, A. M.; Brett, A. M. O. *Bioelectrochemistry* **2004,** 63, (1-2), 229-232.
229. Clemmer, C. R.; Beebe, T. P. *Science* **1991,** 251, (4994), 640-642.
230. Chiorcea, A. M.; Oliveira-Brett, A. M. *Bioelectrochemistry* **2002,** 55, (1-2), 63-65.
231. Yang, Y.; Endo, M.; Hidaka, K.; Sugiyama, H. *Journal of the American Chemical Society* **2012,** 134, (51), 20645-20653.

232. Zhang, X.; Rahman, M.; Neff, D.; Norton, M. L. *Beilstein Journal of Nanotechnology* **2014,** 5, 501-506.
233. Zhou, F.; Michael, B.; Surwade, S. P.; Ricardo, K. B.; Zhao, S. C.; Liu, H. T. *Chemistry of Materials* **2015,** 27, (5), 1692-1698.
234. Alloyeau, D.; Ding, B.; Ramasse, Q.; Kisielowski, C.; Lee, Z.; Jeon, K.-J. *Chemical Communications* **2011,** 47, (33), 9375-9377.
235. Giessibl, F. J. *Reviews of Modern Physics* **2003,** 75, (3), 949-983.
236. Zheng, M.; Jagota, A.; Semke, E. D.; Diner, B. A.; McLean, R. S.; Lustig, S. R.; Richardson, R. E.; Tassi, N. G. *Nature Materials* **2003,** 2, (5), 338-342.
237. Yoo, J.; Aksimentiev, A. *Proceedings of the National Academy of Sciences of the United States of America* **2013,** 110, (50), 20099-20104.
238. El Kirat, K.; Burton, I.; Dupres, V.; Dufrene, Y. F. *Journal of Microscopy-Oxford* **2005,** 218, 199-207.
239. Clemmer, C. R.; Beebe, T. P. *Scanning Microscopy* **1992,** 6, (2), 319-333.
240. Domi, Y.; Ochida, M.; Tsubouchi, S.; Nakagawa, H.; Yamanaka, T.; Doi, T.; Abe, T.; Ogumi, Z. *Journal of Physical Chemistry C* **2011,** 115, (51), 25484-25489.
241. Zhang, Y.; Zhao, H.; Wu, Z. J.; Xue, Y.; Zhang, X. F.; He, Y. J.; Li, X. J.; Yuan, Z. B. *Biosensors & Bioelectronics* **2013,** 48, 180-187.
242. Becerril, H. A.; Woolley, A. T. *Small* **2007,** 3, (9), 1534-1538.
243. Deng, Z. X.; Mao, C. D. *Angewandte Chemie-International Edition* **2004,** 43, (31), 4068-4070.
244. Berman, D.; Erdemir, A.; Sumant, A. V. *Carbon* **2013,** 54, 454-459.
245. Berman, D.; Erdemir, A.; Sumant, A. V. *Materials Today* **2014,** 17, (1), 31-42.
246. Kim, K. S.; Lee, H. J.; Lee, C.; Lee, S. K.; Jang, H.; Ahn, J. H.; Kim, J. H.; Lee, H. J. *Acs Nano* **2011,** 5, (6), 5107-5114.
247. Zhou, F.; Li, Z. T.; Shenoy, G. J.; Li, L.; Liu, H. T. *Acs Nano* **2013,** 7, (8), 6939-6947.
248. Kirkland, N. T.; Schiller, T.; Medhekar, N.; Birbilis, N. *Corrosion Science* **2012,** 56, 1-4.
249. Criado, A.; Melchionna, M.; Marchesan, S.; Prato, M. *Angewandte Chemie-International Edition* **2015,** 54, (37), 10734-10750.
250. Surwade, S. P.; Li, Z. T.; Liu, H. T. *Journal of Physical Chemistry C* **2012,** 116, (38), 20600-20606.
251. Tang, Q.; Zhou, Z.; Chen, Z. F. *Nanoscale* **2013,** 5, (11), 4541-4583.
252. Liu, L.; Ryu, S. M.; Tomasik, M. R.; Stolyarova, E.; Jung, N.; Hybertsen, M. S.; Steigerwald, M. L.; Brus, L. E.; Flynn, G. W. *Nano Letters* **2008,** 8, (7), 1965-1970.
253. Nemes-Incze, P.; Osvath, Z.; Kamaras, K.; Biro, L. P. *Carbon* **2008,** 46, (11), 1435-1442.
254. Nappini, S.; Matruglio, A.; Naumenko, D.; Dal Zilio, S.; Bondino, F.; Lazzarino, M.; Magnano, E. *Nanoscale* **2017,** 9, (13), 4456-4466.
255. Dollekamp, E.; Bampoulis, P.; Poelsema, B.; Zandvliet, H. J. W.; Kooij, E. S. *Langmuir* **2016,** 32, (26), 6582-6590.
256. Herbig, C.; Ahlgren, E. H.; Schroder, U. A.; Martinez-Galera, A. J.; Arman, M. A.; Kotakoski, J.; Knudsen, J.; Krasheninnikov, A. V.; Michely, T. *Physical Review B* **2015,** 92, (8).
257. Jain, S. K.; Juricic, V.; Barkema, G. T. *Physical Chemistry Chemical Physics* **2017,** 19, (11), 7465-7470.
258. Zamborlini, G.; Imam, M.; Patera, L. L.; Mentes, T. O.; Stojic, N.; Africh, C.; Sala, A.; Binggeli, N.; Comelli, G.; Locatelli, A. *Nano Letters* **2015,** 15, (9), 6162-6169.
259. Narayan, R.; Kim, S. O. *Nano Convergence* **2015,** 2, (1), 20.

260. Yang, H. J.; Li, H. Y.; Zhai, J. L.; Sun, L.; Yu, H. W. *Industrial & Engineering Chemistry Research* **2014,** 53, (46), 17878-17883.
261. Han, J. T.; Jang, J. I.; Kim, H.; Hwang, J. Y.; Yoo, H. K.; Woo, J. S.; Choi, S.; Kim, H. Y.; Jeong, H. J.; Jeong, S. Y.; Baeg, K. J.; Cho, K.; Lee, G. W. *Scientific Reports* **2014,** 4.